Systematic effects of the plasma and surfaces in the KATRIN tritium source

Master's thesis
of

Eugen Raspopin

at the Department of Physics
Institute for Astroparticle Physics (IAP)
Institute of Experimental Particle Physics (ETP)

Reviewer:	Prof. Dr. Guido Drexlin (KIT)
Second Reviewer:	Prof. Dr. Kathrin Valerius (KIT)
Advisor:	Dr. Manuel Klein (KIT)
Second Advisor:	Jonas Kellerer, M. Sc. (KIT)

Submitted on: 14 July 2021

I declare that I have developed and written the enclosed thesis completely by myself, and have not used sources or means without declaration in the text.

Karlsruhe, 14 July 2021

. . . .

(Eugen Raspopin)

Contents

Chapter 1.

Introduction

Neutrinos are the lightest and, after the photons, the second most abundant elementary particles in the universe. They significantly contributed to the structure formation of galaxies and galaxy clusters early in the universe [Mar+11; LP14]. As a neutral lepton, the neutrino interacts only via the weak interaction and gravity. The well-established Standard Model of particle physics assumes a mass-less neutrino. However, the discovery of neutrino oscillation and the implication that the neutrino must have a non-vanishing mass opens up the possibility for new physics [Fuk+98; Ahm+02]. Still neutrino oscillation experiments can only determine the neutrino mass splitting and previous attempts of the Mainz and Troitsk experiments to directly determine the absolute neutrino mass scale have previously provided a combined upper limit of $m_\nu < 2\,\mathrm{eV}$ (95 % C.L.) [Kra+05; Ase+11].

The Karlsruhe tritium neutrino (KATRIN) experiment aims to measure the neutrino mass with a sensitivity of 0.2 eV (90 % C.L.) using the energy spectrum of the tritium beta decay. The discovery potential ($5\,\sigma$) is for a neutrino mass of 0.35 eV [Col05]. A neutrino mass leads to a deformation of the spectrum, which is most distinct near the kinematic endpoint. To ensure high statistics in the spectral endpoint region, a high-luminosity windowless gaseous tritium source (WGTS) is used, which provides 10^{11} beta electrons per second[Ake+21b]. The beta electrons are then guided by a magnetic field towards the high-resolution, integrating main spectrometer (MS). The MS acts as a high-pass filter and lets only electrons of the high-energy tail of the tritium beta spectrum reach the focal plane detector (FPD)[Ake+19]. Using the magnetic adiabatic collimation combined with an electrostatic (MAC-E) filter principle, the magnetic field required for guidance is strongly reduced in the MS to convert the transversal energy component of the electrons into the analyzable longitudinal component, and the applied retarding potential creates an energy threshold.

As a consequence of beta decay, a self-ionizing plasma is formed in the WGTS, which is magnetized and cooled down to 80 K or even 30 K. The plasma boundaries are provided by a gold coated rear wall (RW) on the rear side and the 10 m long WGTS beam tube with a diameter of 90 mm. These boundaries define the plasma potential, which serves as the starting potential for the beta electrons in the source. Spatial and temporal inhomogeneities of the plasma potential lead to a distortion of the measured beta spectrum causing a neutrino mass shift that needs to be accounted for. The systematic effects of the plasma and surfaces in the WGTS are investigated during this work. An indicator for minimal spatial inhomogeneity is the so-called optimal RW voltage, which corresponds to the work function difference of the boundaries. One way to determine the optimal RW voltage is by measuring the electron and ion currents at the RW and at the dipole electrodes in the differential pumping section (DPS) originating from the WGTS while varying the RW voltage (IU-scans).

During the operation of the tritium source, IU-scans are typically performed on a daily basis, showing drifts of the optimal RW voltage. The drifts can be divided into several categories including burn-in phase after the restart of the tritium circulation and long-term drift during the tritium circulation. To study the cause of these drifts, this thesis investigates possible correlations with source parameters. This analysis can indicate the physical cause of the drift. Possible drifts caused by RW voltage changes are explored as well. By knowing how the drift is affected by the RW voltage, more adequate voltage settings on the RW can be chosen to avoid it. Based on the observed drifts, the statistical uncertainty on the optimal RW voltage can be determined, and in principle be used in the overall neutrino mass analysis. Features observed in the DPS dipole electrodes could also be a possible indicator of optimal RW voltage. For this purpose they need to be extracted and analyzed from the characteristic IU-curves.

Simulations of electric and magnetic fields are essential to understand the plasma in the source in more detail. For this purpose, KARL is used, which is a Monte Carlo simulation code for the motion of charged particles in the presence of electric and magnetic fields or other external influence like gas flow. Important input parameters are the density of the neutral gas and the velocity of the gas particles. During this thesis, these parameters were simulated with MolFlow+ between WGTS center and the RW. The simulation results of MolFlow+ are also be used to make estimates of transversal ion mobility to draw conclusions about the plasma potential.

The thesis is structured as follows:
In chapter 2 neutrino physics is briefly introduced, while chapter 3 presents the measurement principle and setup of the KATRIN experiment. The plasma located in the WGTS and the influence of the boundaries on the plasma potential are explained in chapter 4. Chapter 5 examines the systematic effects that occur in the interplay between the plasma and its boundaries. Afterwards, chapter 6 shows the MolFlow+ simulation results of neutral gas density and velocities of the gas particles. At last, chapter 7 summarizes the key results of the thesis and gives an outlook on future research about the plasma and surfaces.

Chapter 2.

Introduction to neutrino physics

Neutrinos offer the opportunity to gain insight into the most important open questions in particle physics and cosmology, such as the asymmetry of the abundance of matter and antimatter or what constitutes dark matter. However, the weak interaction of neutrinos makes their detection extremely difficult. An important parameter for the clarification of the open questions is the extremely small but up to now unknown mass of the neutrinos. From oscillation experiments it could be shown that neutrinos have a non-vanishing mass, but until now only upper limits on the absolute neutrino mass scale could be given.

In this chapter, first the historical progression, starting from the postulation up to the discovery of neutrinos, is described. Afterwards, neutrino oscillation, whose discovery implies a non-vanishing mass, and the mechanism behind it are briefly presented. Finally, the various approaches and experiments that aim to measure the absolute mass of neutrinos are presented.

2.1. Postulate and discovery of neutrinos

The history of the neutrino began with a puzzling discovery by James Chadwick in 1914 while studying beta decay. Chadwick found that the emitted electron had a continuous energy spectrum unlike the discrete spectra previously observed in alpha and gamma decays [Cha14]. Possible discussed explanations for the observation were either that the conservation of energy is only valid to a limited extent or that during the beta decay another particle is created which escapes the detection process.

Wolfgang Pauli postulated with his famous letter written in 1930 a new electric neutral and very light spin-1/2 particle, which should solve the problem [PKW64]. This particle could carry away the missing energy in the present three-body decay:

$$\mathrm{X} \rightarrow \mathrm{Y} + \mathrm{e}^{-} + \bar{\nu}_{\mathrm{e}} \; . \tag{2.1}$$

The particle, formerly known as neutron, got its current name, neutrino, from Enrico Fermi, who was responsible for the successful theoretical formulation of beta decay in 1933 [Fer34].

Bethe and Peierls calculated in 1934 the cross section of $\sigma < 10^{-44}\,\mathrm{cm}^2$ for an interaction between a neutrino and a nucleus. They assumed that it is practically impossible to measure the neutrino [BP34]. Nevertheless, Clyde Cowan and Frederick Reines succeeded in discovering the neutrino in 1956 [Cow+56].

Cowan and Reines used the intense flux of neutrinos produced in nuclear reactors for a detection via inverse beta decay:

$$\bar{\nu}_e + p \rightarrow n + e^+ \ . \tag{2.2}$$

For the detection, cadmium chloride ($CdCl_2$) dissolved in a water tank surrounded by liquid scintillator was used. The measurement principle is based on delayed coincidence, which is a unique signature of neutrino caption. After the emission, the positron annihilates with an electron and the resulting photon signal is measured with a liquid scintillator. The moderated neutron is captured by the cadmium nucleus also followed by a photon signal, which, however, is delayed to the first signal. The observed delayed coincidence signal was a confirmation of inverse beta decay and consequently meant the discovery of the neutrino, for which Reines was awarded the Nobel Prize in 1995.

In an accelerator experiment, Leon M. Lederman, Melvin Schwartz, and Jack Steinberger successfully demonstrated in 1962 that neutrinos exist with more than one flavor. For the detection of the ν_μ, protons were collided with a beryllium target. The pions produced in the collision subsequently decay into muons and neutrinos [Dan+62]:

$$\pi^+ \rightarrow \mu^+ + \nu_\mu \ . \tag{2.3}$$

With a steel shielding it was ensured that all particles except the weakly interacting neutrinos were stopped. A small number of neutrinos could then be detected in a spark chamber by the exclusive observation of a muon. It was expected that electrons should also be produced in the case of the single neutrino flavor hypothesis. Due to their absence in the detector, a new neutrino flavor was discovered.

The DONUT experiment in 2001 finally provided evidence for the third flavor ν_τ of the neutrino [Kod+01]. It used protons from the Fermilab Tevatron to shoot them onto a tungsten beam dump. The main source of the ν_τ were charm mesons created after the collision of the protons:

$$D_S^+ \rightarrow \tau^+ + \nu_\tau \ . \tag{2.4}$$

The interaction of the tau neutrino with the iron plates sandwiched with layers of emulsion leads to the production of a few tau leptons. With their special decay signature, consisting of a 2 mm track with additional kink, the tau neutrino could be identified.

After measuring the Z^0 boson resonance with accelerator experiments at SLC and LEP, it was finally shown that there are $N_\nu = 2.9840 \pm 0.0082$ light neutrino species which is consistent with the prediction of the Standard Model [Sch+06].

2.2. Neutrino oscillation

Neutrino oscillation occurs because the neutrino flavor eigenstates, which participate in the weak interaction, are different from the neutrino mass eigenstates, which are relevant for the propagation through space. The neutrino oscillation is an effect in which a generated neutrino of a certain flavor can transform into a neutrino of a different flavor after a propagation and during the measurement process. The oscillation implies that the neutrino has a non-vanishing mass, which requires a modification of the Standard Model.

The first evidence for neutrino oscillation was provided by the Super-Kamiokande experiment in 1998 during the study of atmospheric neutrinos [Fuk+98]. Super-Kamiokande observed that the rate of muon neutrinos, which first propagate through the earth to reach the detector, is only half of the expected rate. The missing rate is explained with a flavor transformation to the tau neutrino because the rate of up-going and down-going electron neutrinos was as expected.

2.2.1. The solar neutrino problem

The first observation in which neutrino oscillation became noticeable was the so-called solar neutrino problem. The solar neutrino problem describes a measured deficit of neutrino flux from the sun compared to the theoretical prediction of the standard solar model by John N. Bahcall [Bah64]. The deficit was first shown by the Homestake solar neutrino experiment of Raymond Davis starting in the 1960s. The neutrinos produced during fusion processes in the sun were measured via a radio-chemical process. Based on the inverse beta process $^{37}\mathrm{Cl} + \nu_\mathrm{e} \rightarrow \mathrm{e}^- + {}^{37}\mathrm{Ar}$ and subsequently determining the production rate of the $^{37}\mathrm{Ar}$, the electron neutrino flux could be calculated [Dav94].

The solar neutrino problem was finally solved in 2001 with the SNO experiment. Based on the detection of Cherenkov light with photomultiplier tubes in a detector with 1000 t of highly pure heavy water, the experiment was sensitive to all three flavors of neutrinos. Strong evidence was given that neutrinos of one flavor transform into other flavors while traveling from the sun to the detector [Ahm+02]. Using charged currents and elastic scattering on deuterons induced by electron neutrinos, and using the neutral currents where neutrinos of all flavors interact with the deuterons, it was shown that only one third of the total flux comes from electron neutrinos. Since previous experiments were only sensitive to electron neutrinos, this effect could not be observed. The missing fraction was thus identified, confirming the theoretical predictions of the standard solar model. Finally, SNO and Super-Kamiokande were recognized with the Nobel Prize in 2015.

2.2.2. Oscillation mechanism

The theoretical description of neutrino oscillation was already worked out by Pontecorvo in 1958 and further developed by Maki, Nakagawa and Sakata [Pon57; MNS62]. In the neutrino oscillation mechanism, a distinction is made between flavor eigenstates $|\nu_\mathrm{e}\rangle$, $|\nu_\mu\rangle$, $|\nu_\tau\rangle$ and three mass eigenstates $|\nu_i\rangle$. Neutrinos are produced and detected as flavor eigenstates, while their propagation through space depends on the mass eigenstates. The flavor eigenstates are described as linear superposition of defined mass eigenstates (and vice versa):

$$|\nu_\alpha\rangle = \sum_i U_{\alpha i} \, |\nu_i\rangle \quad , \tag{2.5}$$

where α denotes the three neutrino flavors e, μ or τ and U the unitary mixing matrix, also known as the Pontecorvo-Maki-Nakagawa-Sakata (PMNS) matrix [Zub12].

The PMNS matrix can conveniently be parameterized as follows [Gro+20]:

$$U = \begin{pmatrix} 1 & 0 & 0 \\ 0 & c_{23} & s_{23} \\ 0 & -s_{23} & c_{23} \end{pmatrix} \begin{pmatrix} c_{13} & 0 & s_{13}e^{-i\delta_\mathrm{CP}} \\ 0 & 1 & 0 \\ -s_{13}e^{i\delta_\mathrm{CP}} & 0 & c_{13} \end{pmatrix} \begin{pmatrix} c_{12} & s_{12} & 0 \\ -s_{12} & c_{12} & 0 \\ 0 & 0 & 1 \end{pmatrix} \begin{pmatrix} e^{i\eta_1} & 0 & 0 \\ 0 & e^{i\eta_2} & 0 \\ 0 & 0 & 1 \end{pmatrix} ,$$

with the abbreviations $c_{ij} = \cos\theta_{ij}$, $s_{ij} = \sin\theta_{ij}$. The free parameters are the three mixing angles θ_{12}, θ_{13} and θ_{23} ($\theta_{ij} \in [0, \pi/2]$), CP violating phase δ_CP and two Majorana phases $\eta_i \in [0, 2\pi]$. However, the Majorana phases are irrelevant in the oscillation and become important only in

Table 2.1.: Oscillation parameters from a global fit to the data from various experiments incorporating the Super-Kamiokande data. Shown is the normal mass ordering. These results are taken from NuFIT 5.0[2]and [Est+20].

	Best fit parameter $\pm 1\sigma$
$\sin^2\theta_{12}$	$0.304^{+0.012}_{-0.012}$
$\sin^2\theta_{23}$	$0.573^{+0.016}_{-0.020}$
$\sin^2\theta_{13}$	$2.219^{+0.062}_{-0.063} \times 10^{-2}$
δ_{CP}	197^{+27}_{-24}
Δm^2_{21}	$7.42^{+0.21}_{-0.20} \times 10^{-5}\,(\mathrm{eV})^2$
Δm^2_{23}	$2.517^{+0.026}_{-0.028} \times 10^{-3}\,(\mathrm{eV})^2$

the determination of the absolute mass [Gro+20]. If neutrinos are not Majorana[1] particles, but Dirac particles, then the Majorana phases η_i can be ignored, leaving only a CP-violating phase δ_{CP}.

Considering only the oscillation between two flavor states, the PMNS matrix can be simplified to a 2 × 2 matrix and one obtains:

$$\begin{pmatrix} |\nu_\alpha\rangle \\ |\nu_\beta\rangle \end{pmatrix} = \begin{pmatrix} \cos\theta & \sin\theta \\ -\sin\theta & \cos\theta \end{pmatrix} \begin{pmatrix} |\nu_1\rangle \\ |\nu_2\rangle \end{pmatrix} . \tag{2.6}$$

The probability of finding a neutrino in a flavor state β after production in the flavor state α is [Ams15]:

$$P(\nu_\alpha \to \nu_\beta) = \sin^2(2\theta)\sin^2\left(1.267\,\frac{\Delta m^2_{21}}{\mathrm{eV}^2}\,\frac{L}{\mathrm{km}}\,\frac{\mathrm{GeV}}{E}\right) , \tag{2.7}$$

with mass squared splitting $\Delta m^2_{21} = m^2_2 - m^2_1$, E as the energy of neutrino and L is the distance between creation and detection of the neutrino. The equation 2.7 shows that for at least two neutrinos, the mass must be non-zero.

Oscillation parameters

For the determination of the flavor oscillation parameters, different experiments were set up, which are specialized on the various ranges of the neutrino energy E and the propagation length L, so that the parameters can be measured. The experiments are distinguished according to the length of the neutrino propagation. There are long baseline, short baseline, atmospheric and solar experiments.

Since only mass-squared differences appear in equation 2.7, it is not possible to determine absolute masses with oscillation experiments. Because the sign of Δm^2_{23} is not known, a distinction is made between normal mass ordering $m_1 < m_2 < m_3$ and inverted mass ordering $m_3 < m_1 < m_2$ [Ams15]. Table 2.1 shows the global best fit results of the neutrino oscillation data for each parameter for the normal mass ordering with $\Delta m^2_{23} \approx \Delta m^2_{13}$.

---

[1] In this case, the neutrino would be its own antiparticle. It is the subject of current research whether neutrinos are Dirac or Majorana fermions.

[2] `http://www.nu-fit.org/`.

2.3. Determination of neutrino mass

Oscillation experiments have shown that neutrinos have masses, however, these experiments are only sensitive to mass squared differences. Consequently, other experimental approaches are needed to determine the absolute mass and also to resolve the question whether neutrinos are Dirac or Majorana particles.

2.3.1. Cosmological observations

Neutrinos played an important role in the formation of the the universe. They significantly contributed to the structure formation of galaxies and galaxy clusters early in the universe [Mar+11; LP14]. As the second most abundant particle after the photon, neutrinos leave measurable imprints on cosmological observables, which are used to obtain a constraint on the neutrino masses [LP14].

The strongest upper limit is given by the Plank experiment for which temperature anisotropies of the cosmic microwave background (CMB) were used combined with information from temperature and polarisation maps and lensing reconstruction [Agh+20]:

$$m_{\text{tot}} = \sum_{i=1}^{3} m_i < 0.12\,\text{eV} \quad (95\,\%\ \text{C.L.})\ . \tag{2.8}$$

Since model assumptions are made for the cosmological constraints on neutrino mass and different data sets are combined in the analysis, this leads to potential systematic effects [Boy19]. It is therefore desirable to determine the neutrino mass model-independent (or an upper limit on it) and use it as constraint for the cosmological analyses.

2.3.2. Neutrinoless double beta decay

In the case that neutrinos are Majorana particles, where the particle is identical to its antiparticle, so-called neutrinoless double beta decays can occur. In contrast to the already observed double beta decay ($2\nu\beta\beta$), the neutrinoless double beta decay ($0\nu\beta\beta$) is a forbidden process in the Standard Model, which violates the lepton number conservation by two units [Ams15].

Figure 2.1 shows the corresponding Feynman diagram for the neutrinoless double beta decay. After the decay of a neutron in a nucleus, a right-handed $\bar{\nu}_\text{e}$ is emitted, which is subsequently absorbed by a second neutron of the same nucleus as a left-handed ν_e. For this process to take place, the particle must be its own antiparticle and have a mass so that a helicity flip can occur [Zub12].

To observe the double beta decay, a beta decay emitter with an even-even nucleus is needed. It is also necessary that the single beta decay is forbidden for the selected nuclei. Compared to the $2\nu\beta\beta$ decay, where a continuous energy spectrum is observed, the signature of the $0\nu\beta\beta$ decay is a characteristic peak at the Q-value of the nuclear transition.

From the half-life of the $0\nu\beta\beta$ decay [Zub12]:

$$(T^{0\nu}_{\beta\beta})^{-1} = G^{0\nu}\,|M^{0\nu}|^2 \left(\frac{m_{\beta\beta}}{m_\text{e}}\right)^2 \ , \tag{2.9}$$

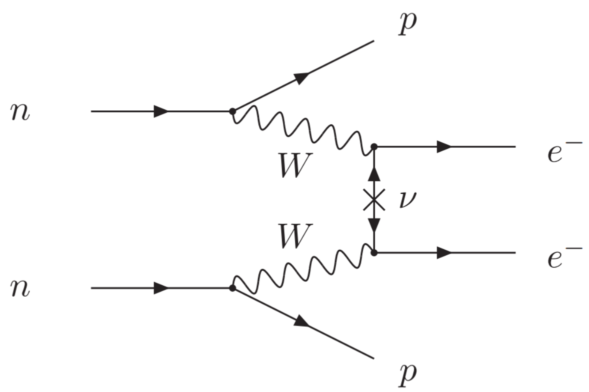

Figure 2.1.: Feynman diagram of neutrinoless double beta decay. Figure taken from [Gro+20].

with the phase space integral $G^{0\nu}$ taking into account the final atomic state and $M^{0\nu}$ as the nuclear matrix element of the transition, the so-called effective Majorana neutrino mass can be determined:

$$m_{\beta\beta} = \left| \sum_{i=1}^{3} U_{\mathrm{e}i}^2 m_i \right| \ , \tag{2.10}$$

with m_i as the mass eigenvalues and $U_{\mathrm{e}i}$ as the elements of the PMNS mixing matrix including Majorana phases. The effective Majorana mass corresponds to a coherent sum and could be affected by cancellations due to the Majorana phases [OW08]. It is important to note that the effective Majorana mass only exist if the neutrino is a Majorana particle. Due to uncertainties in the calculation of the nuclear structure $M^{0\nu}$, this results in an uncertainty of the effective Majorana values for a given half-life by a factor of 2-3 [EM17].

The KamLAND-Zen experiment, consisting of a detector filled with 13 t of liquid scintillator mixed with xenon, is one of the experiments designed to measure the $0\nu\beta\beta$ decay. The summed energy of the two electrons produced by the ^{136}Xe isotope after decay is measured via the emission of scintillation light with photomultiplier tubes [Gan+16]. With a half-life of $T_{\beta\beta}^{0\nu} > 1.07 \times 10^{26}\,\mathrm{yr}$ at 90 % C.L. KamLAND-Zen was able to obtain an upper limit of:

$$m_{\beta\beta} < 61 - 165\,\mathrm{meV} \ . \tag{2.11}$$

Until now, the $0\nu\beta\beta$ decay has not been measured and the possible Majorana nature of the neutrino remains the subject of current research.

2.3.3. Beta decay spectroscopy

When determining neutrino mass with cosmological observables or with neutrinoless beta decay, model assumptions are made. One way to determine the neutrino mass independently of a model is by exploiting the law of conservation of energy and momentum in reactions where neutrinos and antineutrinos are involved.

A suitable reaction for this purpose is the tritium $^3\mathrm{H} = \mathrm{T}$ decay:

$$\mathrm{T}_2 \rightarrow {}^3\mathrm{HeT}^+ + \mathrm{e}^- + \bar{\nu}_\mathrm{e} \ . \tag{2.12}$$

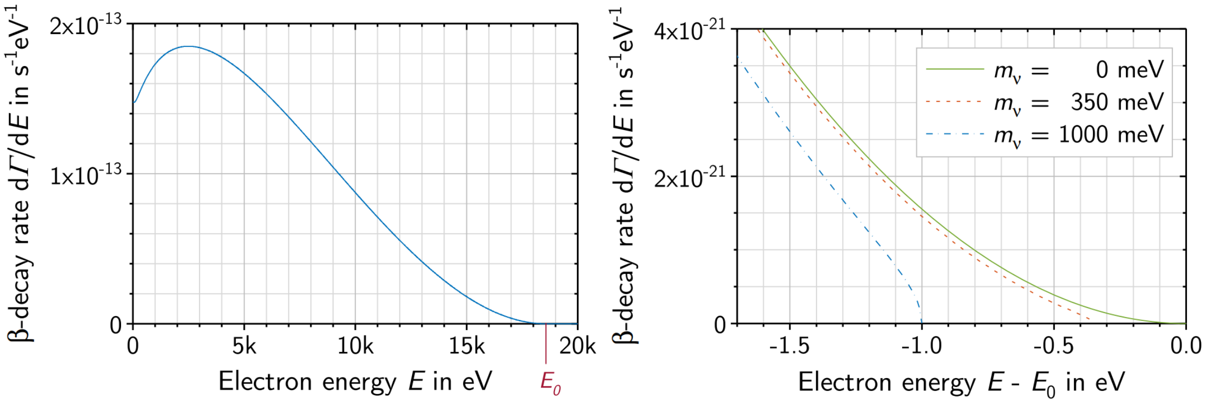

Figure 2.2.: The differential beta energy spectrum of tritium (left) and variation of the endpoint for different electron neutrino masses (right). The units shown correspond to the decay rate of a single tritium nucleus and the endpoint equals $E_0 = 18\,574\,\mathrm{keV}$. Figures taken from [Kle+19].

As shown in figure 2.2, the differential energy spectrum of the beta electron from the decay of a tritium nucleus is analyzed near the endpoint. Due to the non-vanishing mass of the neutrino, this would lead to a shift of the endpoint corresponding to its rest mass. However, the resolution of the experiments is not good enough to resolve this shift. What is measured is the deformation of the spectrum due the neutrino mass a few eV below the endpoint.

Unlike neutrinoless double beta decay (see section 2.3.2), where a coherent sum is measured, the kinematic approach measures the effective electron neutrino mass, which is composed of an incoherent sum of the mass eigenvalues [OW08]:

$$m_{\nu_e}^2 = \sum_{i=1}^{3} |U_{\mathrm{e}i}|^2 m_i^2 \ . \tag{2.13}$$

MAC-E filter

The most recent strictest upper limit for the effective neutrino mass has been established by the KATRIN experiment [Ake+21a]:

$$m_{\bar{\nu}_\mathrm{e}} < 0.8\,\mathrm{eV} \quad (90\,\%\ \mathrm{C.L.}) \ . \tag{2.14}$$

Thus, the KATRIN experiment was able to improve the upper limits established by the previous experiments from Mainz with $m_{\bar{\nu}_\mathrm{e}} < 2.3\,\mathrm{eV}$ at 95 % C.L. [Kra+05] and Troitsk $m_{\bar{\nu}_\mathrm{e}} < 2.05\,\mathrm{eV}$ at 95 % C.L. [Ase+11]. All three experiments are based on the principle of the MAC-E filter (see section 3.1) with gaseous molecular tritium used as the source in the KATRIN and Troitsk experiments and condensed molecular tritium in the Mainz experiment.

Cyclotron radiation emission spectroscopy

An alternative approach to inferring the neutrino mass from the energy measurement of the decay electron is currently being investigated by Project 8. The idea is to measure the emitted cyclotron radiation of the electron in a magnetic field. Using this technique called cyclotron radiation emission spectroscopy, the tritium is confined in a volume within a uniform magnetic field. The frequency of the cyclotron radiation of the decay electron is then measured, which is proportional to the magnetic field and inversely proportional to the kinetic energy of the electron. In the coming phases, Project 8 aims to demonstrate that it is possible to use atomic tritium for the measurement to avoid possible systematic uncertainties in the final states of the molecule. Finally, the experiment strives to achieve a sensitivity of 40 meV. [Obl20]

Calorimetry

An alternative isotope with a smaller Q-value of 2.8 keV is holmium. It decays via electron capture to dysprosium:

$$^{163}\mathrm{Ho} + \mathrm{e}^- \rightarrow {}^{163}\mathrm{Dy} + \nu_\mathrm{e} \ . \tag{2.15}$$

The energy released after a decay of holmium is measured by calorimeters. Because the beta source is embedded in the detector, the total energy released in the decay can be detected, except for the fraction carried by the neutrino. The technology has the advantage of avoiding uncertainties that can arise due to excited final states and energy losses that can occur in the source.

Two experiments HOLMES and ECHo are currently being set up. HOLMES will build a large array of low temperature microcalorimeter. The experiment uses Mo/Cu transition edge sensors coupled to a gold absorber and will reach sensitivities below 2 eV [Gia+21].

ECHo will use metallic magnetic calorimeters with a paramagnetic temperature sensor placed in the magnetic field to investigate the electron neutrino mass in the sub-eV range. Due to temperature changes caused by deposited energy in the absorber, this leads to magnetization in the sensor. The magnetization change will then be measured as a flux change with a SQUID magnetometer [Gas+14].

Chapter 3.

The KATRIN experiment

The KATRIN experiment offers a direct and model-independent method to determine the neutrino mass scale, and aims to determine the neutrino mass with a sensitivity of 0.2 eV (90 % C.L.) after five years of measurement time [Ake+19]. With the current upper limit for the neutrino mass of $m_\nu < 0.8\,\mathrm{eV}$ (90 % C.L.), the KATRIN experiment has already improved the upper limit from the previous experiments in Mainz and Troitsk by more than a factor of two [Ake+21a; Ase+11; Kra+05].

This chapter first describes the measuring principle of the KATRIN experiment. Then, the setup and the main components are presented. Finally, the data acquisition software is discussed and the analysis software that was used in this thesis is introduced.

3.1. Measurement principle

In the tritium source of the KATRIN experiment, 10^{11} electrons per second are produced and emitted isotropically in the radioactive beta decay of gaseous tritium. Then a strong magnetic field is used to guide the electrons towards the spectrometers. The high-pass filter in the main spectrometer is based on the MAC-E filter principle, which stands for magnetic adiabatic collimation combined with an electrostatic filter [Pic+92]. Figure 3.1 illustrates the working principle of the MAC-E filter based on the main spectrometer of KATRIN.

MAC-E filter

The electrons, which are guided by the magnetic field, perform a cyclotron motion around the magnetic field lines and have a total energy E_{tot}, which can be divided into a parallel $E_{\parallel}$ and a transversal $E_{\perp}$ component:

$$E_{\mathrm{tot}} = E_{\parallel} + E_{\perp} \ . \tag{3.1}$$

Towards the center of the main spectrometer, the magnetic field B is reduced by about four orders of magnitude. Since the spatial variations of the magnetic field are small, the motion of the electrons is adiabatic and the conservation of angular momentum applies, which is associated with a constant magnetic moment μ [Zub12]. In a non-relativistic approximation, the transversal energy of the electron can then be expressed as follows [Col05]:

$$\mu = \frac{E_{\perp}}{B} = \mathrm{const} \ . \tag{3.2}$$

If the electron moves towards the center, most of the cyclotron energy is converted into analyzable longitudinal energy $E_{\parallel}$ [Pic+92]. Accordingly, the electron momentum is collimated parallel to

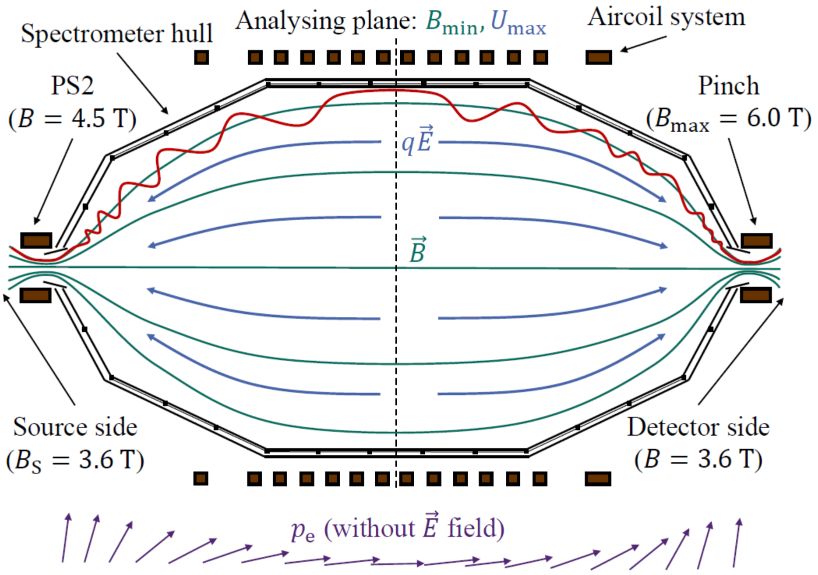

Figure 3.1.: Principle of the MAC-E filter in the KATRIN experiment. The widening of the magnetic flux tube leads to a drastic reduction of the magnetic field, which causes the transversal components of the electron momentum to be transferred to the longitudinal direction. If the electrons have a total energy that exceeds the retarding energy of qU_{max}, they reach the detector, whereas all other electrons are reflected. Figure taken from [Sei19].

the magnetic field, which is illustrated in figure 3.1. However, due to the non-vanishing magnetic field in the analyzing plane, not all of the transversal energy is converted into longitudinal energy, resulting in the so-called energy filter width:

$$\Delta E = E \cdot \frac{B_{\mathrm{min}}}{B_{\mathrm{max}}} \ . \tag{3.3}$$

Consequently, the energy resolution $\Delta E/E$ is limited by the ratio between the minimum and maximum applied magnetic field [LS85]. With the KATRIN design values for the magnetic field of $B_{\mathrm{max}} = 6\,\mathrm{T}$ at the pinch magnet and $B_{\mathrm{min}} = 3 \times 10^{-4}\,\mathrm{T}$ [Col05] in the analyzing plane and with electron energies near the end point $E_0 \approx 18.6\,\mathrm{keV}$, this results in a filter width of:

$$\Delta E \approx 0.93\,\mathrm{eV} \ . \tag{3.4}$$

The analyzing plane is located where the maximum electric field is applied and it does not have to be in the center. During the preparation of the thesis, it is common to use a shifted analyzing plane (SAP). The negative retarding potential $U \approx -18.6\,\mathrm{kV}$ applied to the spectrometer acts as an electrostatic barrier. Exceeding the energy qU, the electrons are re-accelerated and collimated onto the detector. The remaining electrons, whose energy is not high enough to overcome the potential barrier, are reflected back.

Now the retarding potential can be varied and the corresponding count rate of the electrons is recorded at the detector. From this, the integral beta spectrum for the determination of the neutrino mass is obtained.

Magnetic mirror effect

Since the electrons in the source are created isotropically [Ste+13] with a random angle θ between the momentum vector $\vec{p}$ and the magnetic field vector $\vec{B}$, electrons with large angles will travel longer distances and suffer energy losses due to scattering effects. Consequently, it is favorable to sort out electrons with large pitch angles. To reduce the with the energy loss of the electrons associated systematic effects, the so-called magnetic mirror effect is used. Moving from areas of small to large magnetic fields, the longitudinal energy $E_{\|}$ is reduced until the particle has no more momentum in forward direction. The magnetic mirror is therefore the reverse effect of magnetic collimation [Ste+13].

With the KATRIN design value of the magnetic field in the source of $B_{\mathrm{S}} = 3.6\,\mathrm{T}$ [Col05], this corresponds to a maximum acceptance angle of:

$$\theta_{\max} = \arcsin\sqrt{\frac{B_{\mathrm{S}}}{B_{\max}}} \approx 50.8° \ . \tag{3.5}$$

Accordingly, all electrons with pitch angles $\theta > \theta_{\max}$ are rejected 3.3.

Neutrino mass analysis
The integral beta spectrum is then compared with a fit model, which contains four free fit parameters [Kle14]:

A_{sig} : signal amplitude of the electron rate
A_{bg} : background rate
E_0 : effective endpoint energy
m_ν^2 : neutrino mass squared

The upper plot of figure 3.2 shows all fit parameters and their effect on the integrated beta spectrum. Shown is a simulated tritium beta spectrum near the endpoint for a hypothetical neutrino mass of $m_\nu = 350\,\mathrm{meV}$ compared to the theoretical model expectation for $m_\nu = 0\,\mathrm{meV}$. In the middle plot one can see the effect of a non-vanishing neutrino mass. A non-zero neutrino mass would then be expected at the maximum distortion, which can be seen at retarding energies of about 4 eV below the endpoint at nominal background conditions. The bottom plot shows the measurement time distribution (MTD) over the retarding potential.

3.2. Overview of hardware components

For a successful measurement of the tritium beta spectrum in the KATRIN experiment, a complex system of hardware components is required. An overview of the entire setup of the KATRIN experiment is given in this section.

Figure 3.3 shows the KATRIN setup, which is over 70 meters long and divided into the following components. The rear section (RS) is used for calibration and monitoring purposes and also contains the rear wall (RW), which defines the plasma potential in the windowless gaseous tritium source (WGTS). The tritium gas is injected in the WGTS and then removed in the differential pumping section (DPS) and cryogenic pumping section (CPS). The beta electrons produced during the tritium decay are guided along magnetic field lines into the pre-spectrometer (PS), where most beta electrons can be rejected with a filter potential.[1] Beta electrons with energies

---

[1] Meanwhile, the PS is used only for test measurements and for monitoring that no ions enter the spectrometers during neutrino mass measurements.

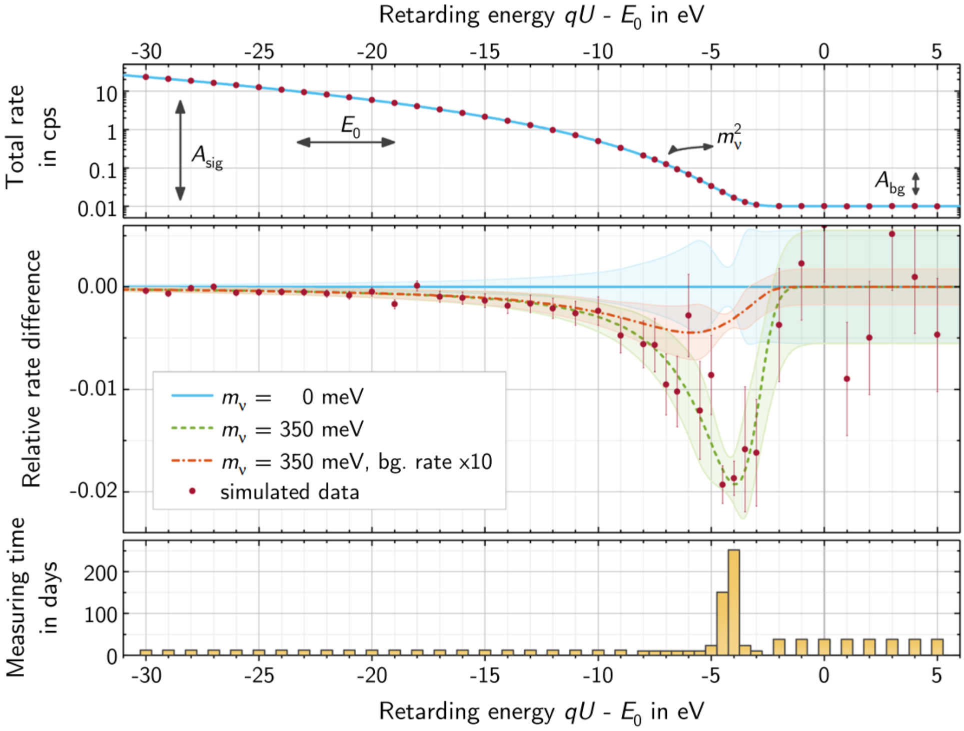

Figure 3.2.: Simulated integral beta spectrum for a neutrino mass of 350 meV. The simulated data are compared with the theoretical model for $m_\nu = 0\,\text{meV}$. The upper plot also shows the effect of the four free fit parameters on the theoretical model of the beta spectrum. A non-vanishing mass causes a deficit in the relative rate difference near the endpoint, which can be seen in the middle plot. The lower plot shows the MTD, which indicates the measurement time at the corresponding retarding potential. Figure taken from [Kle+19].

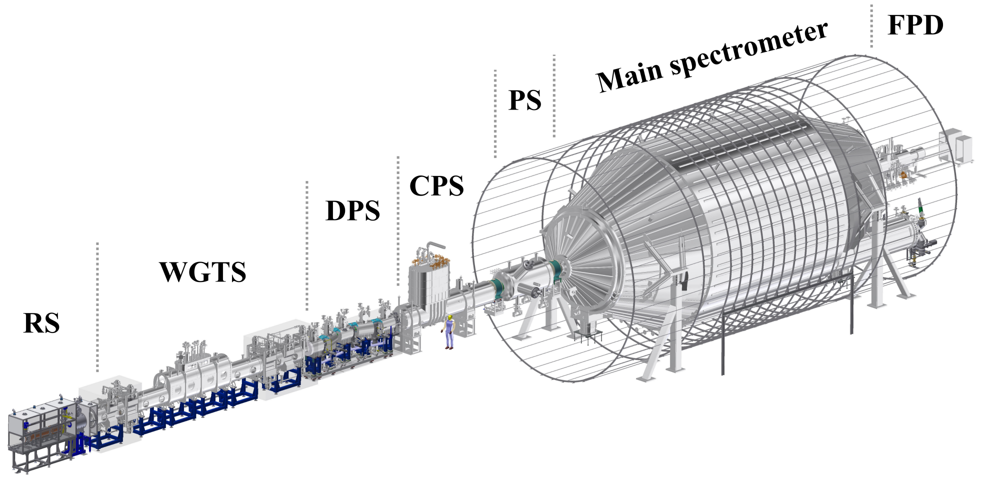

Figure 3.3.: Setup of the KATRIN experiment. Figure taken from [Kle19].

close to the endpoint are then investigated with the MAC-E filter of the main spectrometer (MS). If the electrons overcome the retarding potential, they are finally counted with the focal plane detector (FPD).

3.2.1. Source and transport section

The supply of the beta electrons takes place in the source, where the tritium gas is injected. The electrons are then guided to the spectrometers via the transport section. Hereafter, these components are introduced.

Windowless gaseous tritium source

The WGTS consists of a 10 m long cylindrical beam tube with a diameter of 90 mm (see fig. 3.4). The tritium gas is injected in the center of the WGTS. After the tritium decay, the beta electrons are guided along the magnetic field towards the spectrometer and the RW by superconducting magnets. The large number of beta electrons leads to the ionization of the tritium gas, producing ions and secondary electrons that form a cold and magnetized plasma in the source (see chapter 4).

Beyond the central 10 m long WGTS beam tube are the differential pumping sections DPS1-R and DPS1-F. With two pump ports on both sides, which are equipped in the first stage with turbomolecular pumps (TMPs) of type Leybold Turbovac MAG W 2800 [Ake+21b], the tritium gas is pumped out and subsequently fed back into the injection system after circulation and purification through tritium loops. The circulation system consists of the inner and outer tritium loops. In addition, the composition of the gas is monitored in real time with a laser Raman spectroscopy (LARA) cell [PSB15].

The injection is continuous to ensure a stationary gas density profile. The gas profile is characterized by the column density ρd, which is the integrated gas density along the length of the WGTS [Mar20]. With a tritium purity of $\epsilon = 95\,\%$, the WGTS yields a nominal activity of 1.7×10^{11} Bq with the corresponding design column density of $5 \times 10^{17}\,\mathrm{m}^{-2}$ [Col05]. To achieve the sensitivity it is necessary to stabilize the column density to 0.1 % [Bab+12].

The WGTS can be operated at temperatures of around 30 K, 80 K and 100 K. This is done in

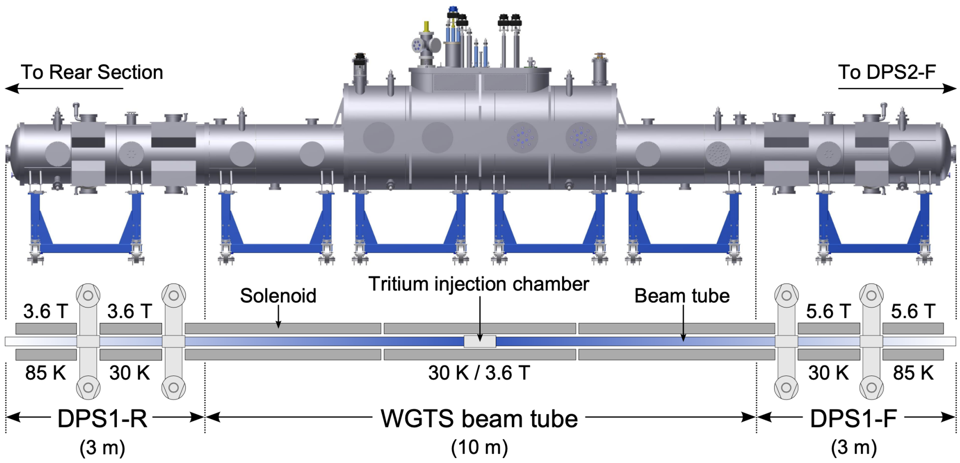

Figure 3.4.: Windowless gaseous tritium source. The entire 16 m long cryostat is shown at the top. The tritium gas is injected via capillaries into the central beam tube of the WGTS. Outside the 10 m beam tube in the rear and front direction are the four pump ports, which constitute the DPS1-R/F, where the tritium gas is subsequently pumped out with TMPs. The superconducting magnets guide the beta electrons in the rear and front directions. Figure taken from [Har15].

the central area of the WGTS of the beam tube with a two-phase cooling system. In the case of 30 K neon and at 80 K nitrogen is used as the coolant. The current default temperature setting for neutrino mass measurements is 80 K. In the outermost beam tube elements only gaseous nitrogen is used [Ake+21b].

Differential Pumping Section

The DPS forms after the WGTS the second differential pumping stage DPS2-F whose task is to reduce the neutral tritium flow together with the first pumping stage DPS1-F by at least seven orders [Col05]. To ensure this, six TMPs of type Leybold Turbovac MAG W 2800 are directly connected to five pump ports [Ake+21b] (see fig. 3.5). The pump ports are connected to five beam tube elements, each inclined at 20° to one another to improve the removal of neutral gas.

Five individual superconducting magnets in the DPS are used to transport the beta electrons adiabatically. However, not only the beta electrons needed for the measurement of the neutrino mass are guided by the magnetic field but also positive and negative ions, which unfortunately cannot be removed with the TMPs. [Ake+21b]

To avoid contamination with tritium ions in the MS, the associated background and systematic effects on the neutrino mass measurement, five ring electrodes were installed along the beamline to block positive ions with a positive electrostatic potential. Two of the ring electrodes are mounted in the last beam tube element 5 (BT5) and in pump port 5 (PP5) of the DPS (see fig. 3.6) [Fri20]. If the positive ions were only blocked at the ring electrodes, positive space charge may arise which might lead to plasma instabilities and distortion of the beta electron spectrum, resulting in a systematic effect on the neutrino mass measurement [Kle19].

Four dipole electrodes were installed in the DPS to remove the accumulated positive ions (see fig. 3.6). The negative electric dipole field in the electrodes is able to remove the positive ions via the $\vec{E} \times \vec{B}$ drift. In the gap of the dipole electrodes, vertical lobes are welded to each of the electrodes, where the ions are neutralized and then pumped out as a neutral gas. The

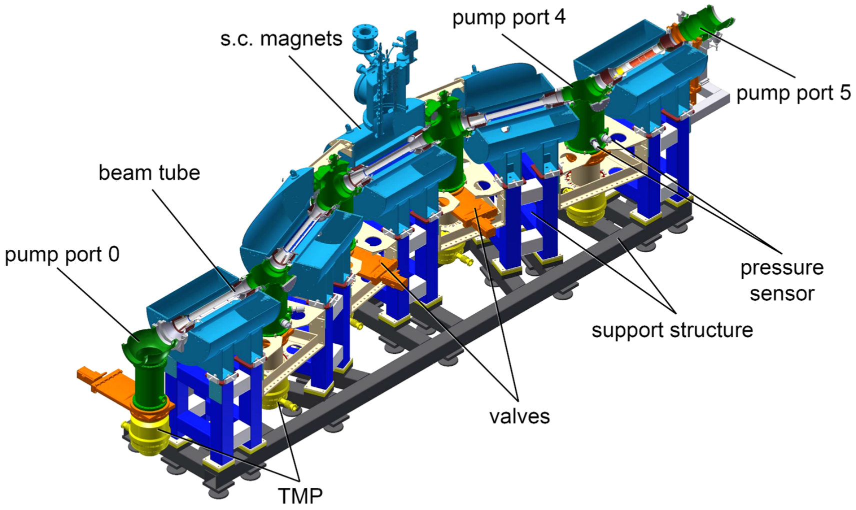

Figure 3.5.: CAD drawing of the DPS. The five beam tube elements are connected via pump ports attached with two TMPs each. In addition, the beam tube elements are surrounded by superconducting solenoid magnets and the pump ports zero and five connect DPS, WGTS and the cryogenic pumping section (CPS). Figure taken from [Fri+19].

neutralization current can then be measured with ammeters. [Kle19] For the electric dipole field, the first three upper electrodes of the DPS are set to $(-15 \ldots -85)$ V, whereas the lower electrodes are always set to -5 V. Meanwhile, positive voltages are applied to the DPS4 dipole electrodes.

Cryogenic Pumping Section

To reduce the remaining gas flow from the DPS further by seven orders of magnitude, an argon frost layer is used, which is located in the CPS on the surfaces of the gold-coated inner walls of the beam tube. The tritium molecules can then adsorb onto the 3 K cold surface by cryosorption. The beam tube elements are also tilted as in the DPS to prevent particles from passing directly into the spectrometers. In addition, the probability for pumping is increased. [Röt19] At the end of the CPS in spectrometer direction in the outer rim of the flux tube is the foward beam monitor (FBM), which is used to monitor the source activity [Ell19].

3.2.2. Rear section

The rear section is a system used for calibration and monitoring. For calibration purposes, an electron source (e-gun) is used, which provides a beam of quasi-monoenergetic and angular-selected photoelectrons [Bab14; Sch21]. Furthermore, the rear section contains the rear chamber (see fig. 3.7), which houses two Beta Induced X-ray Spectrometry (BIXS) detectors that monitor the activity of the tritium source [Röl15].

The BIXS detectors measure the bremsstrahlung induced by beta electrons as they impinge on the RW, which is also contained in the rear chamber. The RW intersects the magnetic field lines and thus serves as a boundary for the electrons and ions [Fri20].

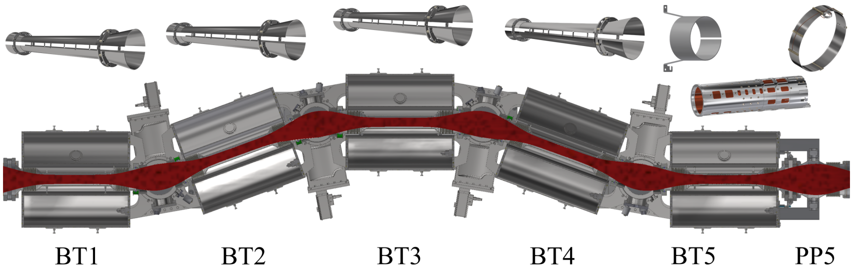

Figure 3.6.: CAD model of the DPS with ring and dipole electrodes. The electrodes shown above are located at the corresponding positions in the DPS shown below. The ring electrodes are placed at the beginning of beam tube element five (BT5) and at pump port five (PP5) to block ions with a positive potential. To prevent the ions from accumulating and leading to possible distortions of the beta spectrum, they are removed with four dipole electrodes via the $\vec{E} \times \vec{B}$ drift. To distinguish the different ion species, a cylindrical FT-ICR mass spectrometer unit was installed between the two ring electrodes. Figure taken from [Ake+21b].

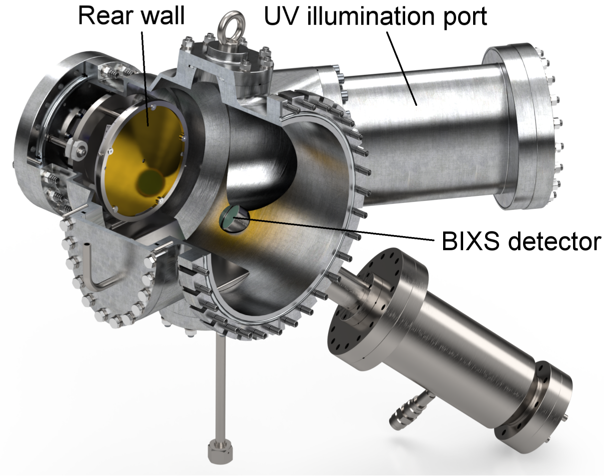

Figure 3.7.: Rear chamber and view of the interior components. Figure taken from [Fri20].

Rear wall

With a diameter of 145 mm, the RW is a gold-coated stainless steel disc on which the magnetic field lines terminate. The ions and electrons from the WGTS, enclosed in a flux tube of 135 T cm^{-2}, can impinge on the surface where they are continuously measured with a picoammeter. In addition, a bias voltage of ±500 V can be applied to adjust the surface potential of the RW. Due to the charged particles coming from the WGTS plasma, the plasma potential can also be manipulated. Influencing the plasma potential is essential because it serves as the starting potential for beta electrons. Therefore, it is desirable to achieve a plasma potential that is as homogeneous as possible. [Ake+21b]

There is also the possibility to supply the plasma with additional electrons. A Cermax xenon UV lamp is used for this purpose, which is directed at the RW. Due to the photoelectric effect, electrons can be produced, which improve the conductivity of the plasma and maintain the quasineutrality of the plasma. [Ake+21b]

3.2.3. Spectrometer and detector section

In the following section, the two spectrometers and the main detector used in the KATRIN experiment for the purpose of selection and detection are introduced.

Pre-Spectrometer
The pre-spectrometer (PS) can serve as a pre-filter for the MS, reducing the flux of beta electrons with a retarding potential of $-18.3\,\mathrm{kV}$. The pre-filtering can reduce the probability of possible ionization of residual gases in the MS which minimizes the associated background rate. [Col05] Meanwhile, the PS is used only for test measurements and for monitoring that no ions enter the spectrometers during neutrino mass measurements. The PS consists of an ultra-high vacuum vessel with a length of 3.4 m and a diameter of 1.7 m and is also based on the MAC-E filter principle as the MS [Frä+11].

Main Spectrometer
With a diameter of 9.8 m, a length of 23.3 m and a weight of about 200 t, the MS is a high-pass filter which, like the PS, is also based on the MAC-E filter principle [Are+16]. To obtain the required ultra-high vacuum conditions of $1 \times 10^{-11}\,\mathrm{mbar}$ in the MS vessel, non-evaporable getter pumps and TMPs are used [Ake+21b; Are+16]. The applied retarding potential can be fine-tuned with inner wire electrodes attached to the inner wall of the stainless steel UHV vessel. In addition, the inner wire electrodes prevent secondary electrons induced by cosmic rays from entering the UHV volume [Val11]. To fine-tune the magnetic field inside the vessel and to compensate the influence of the earth's magnetic field, an air coil and solenoid system were installed around the MS [Erh+18].

Focal plane detector
The FPD is the last component where the beta electrons finally hit a sensitive surface with a diameter of 90 mm. The detector consists of a single silicon wafer with 148 pixels of p-i-n diodes. The array is divided into twelve concentric, equal-area rings with twelve pixels each and an additional bull's eye consisting of four pixels. This arrangement allows to investigate radial and azimuthal effects with the FPD. Before detection, the beta electrons are accelerated with a post acceleration electrode (PAE) to bring the energy signal into regions of low intrinsic detector background. [Ams+15]

3.3. Software for data acquisition and analysis

An enormous amount of data is generated at the KATRIN Experiment, which must first be acquired and then made available to the user for analysis.

Data acquisition
The KATRIN experiment distinguishes between two types of data. The first group is the so-called run-based data, which consists of events observed at the detector system. Run-based data is collected with the object-oriented real-time control and acquisition (ORCA) DAQ software and the main detector system for this group of data is the FPD.

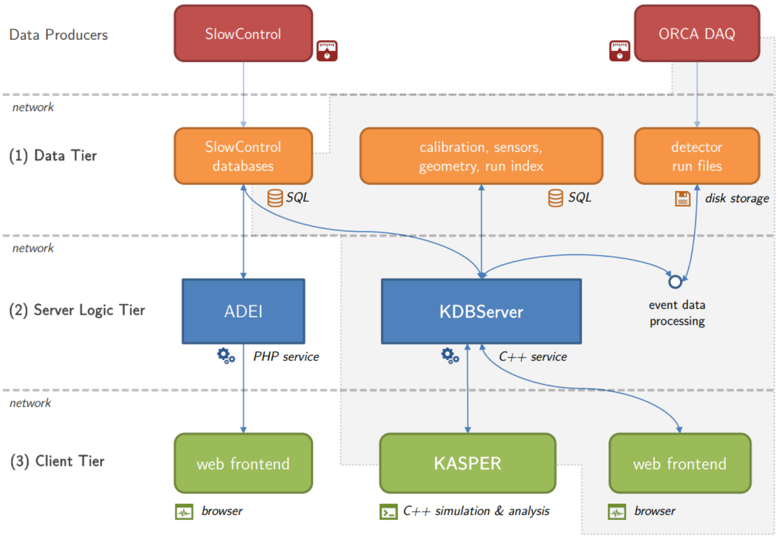

Figure 3.8.: Data infrastructure of the KATRIN experiment. The slow control and run-based data types enter the data tier, where the data is processed and stored. Afterwards, the data enters the server logic tier, this area combines the software modules that are responsible for data management. The client tier contains the software that allows data to be requested for analysis. Figure taken from [Kle14].

The second type is slow control data, consisting of all recorded information that not include detector data (FPD or FBM). The slow control data is continuously recorded and then stored in SQL databases. The raw data from the databases is then collected with the Advanced Data Extraction Infrastructure (ADEI). [Kle14] ADEI also offers its own web front-end, allowing the slow control data to be visualized and downloaded by the user for further analysis (see fig. 3.8) [Chi+10].

Data analysis

Most of the simulation and analysis modules are located in the C++ based software framework KASPER. Besides modules for particle tracking (Kassiopeia) and electromagnetic field solving (KEMField), the module KaFit provides a set of statistical methods to extract the neutrino mass from observed data [Kle14].

For most of the analyses in this thesis, the software framework Pancreas was used. Pancreas (Python ANalysis software for Currents at the REAr wall and dipole electrodeS) was developed specifically for the analysis of plasma-induced currents on the RW and on the DPS dipole electrodes.[2] The slow control data required for the analysis is downloaded with the ADEI extractor[3] via a web request. Pancreas can be used to perform near-time analysis during neutrino mass measurements. In particular, the so-called optimal RW voltage can be determined from the IU-scans, which is important for determining the plasma potential and serves as an indicator of the homogeneity of the plasma. But also for more sophisticated analyses, Pancreas provides the first stage by allowing to download the necessary data.[4]

---

[2] Pancreas can be downloaded from the KATRIN git repository: `https://nuserv.uni-muenster.de:8443/katrin-git/currentanalysis`.

[3] Developed by Alexander Marsteller.

[4] Detailed documentation can be found in: `https://ikp-katrin-wiki.ikp.kit.edu/katrin/index.php/Current_analysis_with_PANCREAS`.

Chapter 4.

Plasma in the KATRIN tritium source

Due to the decay of the tritium molecules taking place in the WGTS, daughter ions are produced together with the beta electrons. The beta electrons produce secondary electrons by ionization processes in the tritium gas. The secondary electrons together with the ions form a plasma whose electric potential serves as the starting potential of the beta electrons.

In this chapter, the basic plasma-defining criteria related to the source plasma in the WGTS are first discussed. Then, the importance of the boundaries and their effect on the homogeneity of the plasma potential is described. Finally, methods are presented to determine the optimal RW voltage that implies maximum spatial homogeneity of the plasma potential.

4.1. Properties of the plasma in the tritium source

Plasma is a state of matter in which free charge carriers are present; consequently, it is also referred to as an electrical conductor. The separated charge carriers like electrons, ionized atoms or ionized molecules exert forces on additional charge carriers with the help of long-range electromagnetic fields. This leads to the emergence of collective phenomena defining the new state of matter [Str11].

Plasma is also present in the WGTS, but it is very different from the usual conditions found in nature or in other experiments. Based on the characterization in density and temperature, it can be seen in figure 4.1 that there is a plasma with comparatively low density of charged particles of about $10^5 - 10^6\,\mathrm{cm}^{-3}$ and low temperature $T = 80\,\mathrm{K}$ in the WGTS [Col05; Kuc16].

Different from plasma, where the high temperature or strong external electric fields lead to the formation of the plasma state, in the WGTS the tritium β-decay initiates this process. The decay electrons now have a certain probability of ionizing the neutral gas in the source. Subsequently, low-energy electrons and ions are produced, which mainly form the plasma in the WGTS. Furthermore, the plasma is confined and strongly magnetized by superconducting solenoids. Consequently, the electrons have a negligible conductivity transverse to the magnetic field lines. In contrary ions have a much higher transversal conductivity due to scattering processes on neutral gas particles. [Bab14]

Nevertheless, the plasma in WGTS fulfills the criteria to be called as the fourth state of matter. For the definition of the criteria, it is first necessary to describe the concept of Debye Shield-

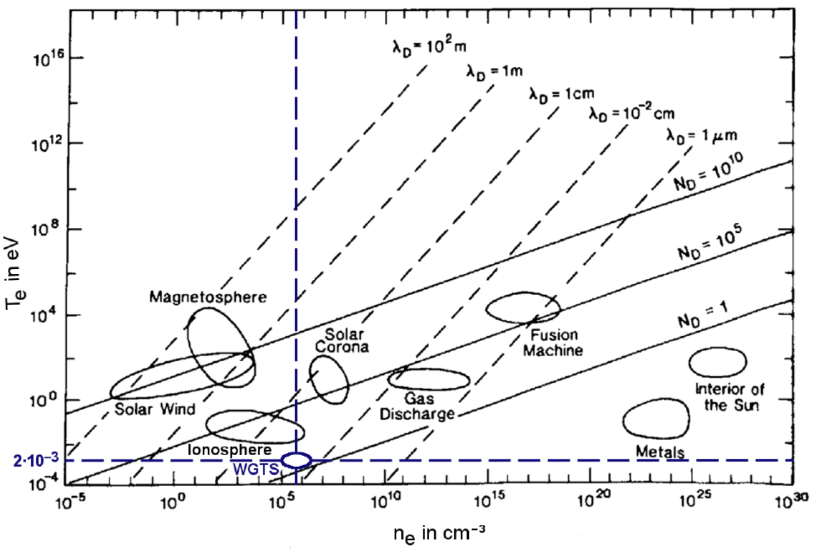

Figure 4.1.: Characterisation of plasmas according to particle density and temperature. The plasma in WGTS differs from most of the listed plasma from nature and technology insofar as it has a comparatively low density and exists at only 30 K. Figure taken from [Fri20] slightly modified version of [Gal12].

ing. As a consequence of the collective effects of a plasma, the charged particles can arrange themselves in such a way that within a length λ_D called Debye length any electrostatic fields are effectively shielded. The Debye length is given by:

$$\lambda_\mathrm{D} = \left(\frac{\epsilon_0 k_\mathrm{B} T}{n_\mathrm{e} e^2}\right)^{1/2} , \tag{4.1}$$

with electron number density n_e, the vacuum permittivity ϵ_0, the Boltzmann constant k_B, the elementary charge e and temperature T. When considering volumes, it is useful to define a so-called Debye sphere with the radius λ_D as $4/3\pi\lambda_\mathrm{D}^2$. [Bit13]

In the absence of external forces and with the effect of Debye shielding, the plasma is able to neutralize all microscopically appearing space charges, hence it is called a macroscopically neutral plasma. Due to the possibility of the charged particles to move freely in the plasma and to compensate excess charges, macroscopic neutrality can also be maintained over distances greater than λ_D. [Bit13]

If a boundary surface is introduced, a disturbance is created in the plasma in the form of a plasma sheath directly in front of the surface. The width of this sheath is of the order of λ_D where a deviation from macroscopic electrical neutrality can occur. Nevertheless, the outer domains still remain macroscopically neutral but under the condition that after the introduction of the surface there is still enough space for a plasma to be maintained [Bit13]. This leads to the first of four necessary conditions for a plasma to form. Hereby, the characteristic length L is introduced, which describes the size of the system available for the plasma. If there is not enough space, the shielding effect cannot occur. Therefore, the *first criterion* is:

$$L \gg \lambda_\mathrm{D} . \tag{4.2}$$

For the WGTS conditions with a temperature of $T = 80\,\mathrm{K}$ this corresponds to a Debye length of about $10^{-4}\,\mathrm{m}$. Comparing the beam tube length $L = 10\,\mathrm{m}$ and diameter $d = 90\,\mathrm{mm}$, the condition is fulfilled.

The *second criterion* is that the number of electrons in a Debye sphere must be very large in order to maintain the shielding effect:

$$n_\mathrm{e}\lambda_\mathrm{D}^3 \gg 1\ . \tag{4.3}$$

with WGTS at $T = 80\,\mathrm{K}$ this corresponds to $n_\mathrm{e}\lambda_\mathrm{D}^3 \approx 10^2$.

The *third criterion* describes the macroscopic neutrality, which is fulfilled when the electron density n_e and ion density n_i are equivalent in the absence of external disturbances:

$$n_\mathrm{e} = \sum_j Z_j n_{i,j}\ , \tag{4.4}$$

with Z_i as the charge number of a specific ion species j [Din+05; Bit13]. This criterion is only guaranteed under the circumstance that the boundary conditions, such as the RW, fulfill certain conditions. If a high positive voltage is applied to the RW, electrons are predominantly drawn out of the plasma and the macroscopic density of ions exceeds. The same also applies to the ions with a high negative voltage, here only ions are removed from the plasma. [Fri20]

The *fourth* and final *criterion* for the existence of a plasma relates to the interaction of electrons with neutral particles, because collisions between them can affect the collective properties of the plasma. But before the criterion is explained in more detail, the plasma frequency must first be introduced.

It is important for the stability of the plasma that disturbances of the macroscopic space charge neutrality are immediately compensated by collective motion of the charged particles. In particular, the much lighter and more mobile electrons are considered here, which, after neutralization of the disturbance, form a counter-field due to inertia and thus oscillate around ions. On statistical average, however, macroscopic neutrality is maintained. This oscillation is called plasma oscillation and due to the comparably large mass of the ions, it is dominated by the electrons:

$$\omega_\mathrm{p} \approx \omega_\mathrm{pe} = \left(\frac{n_\mathrm{e}e^2}{\epsilon_0 m_\mathrm{e}}\right)^{1/2}\ . \tag{4.5}$$

To ensure that the plasma frequency is not significantly damped by the neutral gas and that the electrons remain independent of the movement of the neutral particles, the collision frequency must be lower than the plasma frequency $\nu_\mathrm{en} < \nu_\mathrm{pe}$. From this, the *fourth criterion* can be formulated as follows:

$$\omega_\mathrm{p}\tau > 1\ , \tag{4.6}$$

where ω_p stands for the plasma frequency and $\tau = 1/\nu_\mathrm{en}$ as the average time an electron travels between collisions with neutral particles. [Din+05; Bit13]

Considering the plasma in the WGTS, the plasma frequency ranges from $\sim$ 18 to 56 MHz, depending on which electron density is used. With a mean collision time of $\tau = 0.5 \times 10^{-6}\,\mathrm{s}$, the value of $\omega_\mathrm{p}\tau$ is in the range of 10 to 31. [Fri20]

4.2. Boundary surfaces and their effect on the plasma potential in the WGTS

For the stability of the plasma potential, the boundaries are of utmost importance. On the one hand, the stainless steel beam tube confines the plasma in the radial direction and is by

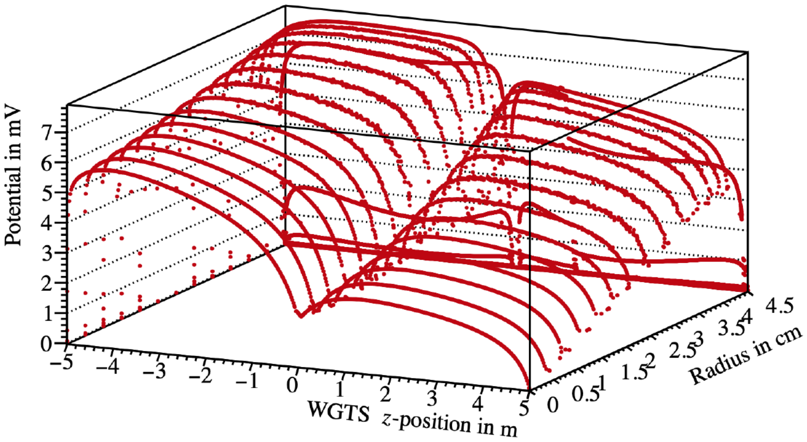

Figure 4.2.: Plasma potential within the WGTS simulated at $T = 30\,\mathrm{K}$. Simulation was performed with an axially symmetric model where the RW was set at $z = -5\,\mathrm{m}$. With the potential of the RW and the beam tube set to zero, this leads to a steep decrease of the potentials at the boundaries. The deformation in the center is related to the injection point of the WGTS. Figure taken from [Mac21] with data from [Kuc16].

definition on ground. On the rear side, the gold coated RW is the limiting surface. Here the RW voltage U_{RW} can be adjusted as desired to control and stabilize the properties of the plasma. On the front side, the ions and electrons are blocked by electric potentials in the DPS electrodes and spectrometers.

The boundary potentials of the plasma are the surface potentials ϕ of RW and beam tube and are defined as follows:

$$\phi_{\mathrm{RW}}(t) = U_{\mathrm{RW}} - \frac{\Phi_{\mathrm{RW}}(t)}{e} \tag{4.7}$$

$$\phi_{\mathrm{BT}}(t) = U_{\mathrm{BT}} - \frac{\Phi_{\mathrm{BT}}(t)}{e} \ , \tag{4.8}$$

with $\Phi(t)$ as the time dependent work function of the specific boundary. The work function is defined as the energy required to remove an electron from a solid into the vacuum right above the surface [AM+76]. Since the boundaries have large surface areas, especially the beam tube, spatial variations of the work function can occur. There are also temporal variations, e.g., different amounts of impurities can accumulate on the surface by adsorption and significantly change the surface properties [Kuc16].

It is essential to know the shape of the potential because it serves as the starting potential of the beta electrons in the WGTS. Spatial and temporal variation would lead to systematic effects appearing in the neutrino mass analysis. As can be seen in figure 4.2, the boundary conditions are responsible for the radial and longitudinal inhomogeneity of the plasma potential.

Based on steady state plasma argumentation, it is assumed that the plasma potential must be between the beam tube and the RW surface potential. A first possibility is that the plasma potential in the range of $\phi_{\mathrm{RW}} < U_{\mathrm{Pl}} < \phi_{\mathrm{BT}}$. In this case, the ions are blocked by the beam tube and the electrons would not reach the RW and due to the magnetic field, the electrons are restrained from moving radially. Because they are also trapped on the front side by electric potentials in the DPS and spectrometers, the trapped electrons will most likely be drifted to the beam tube walls by plasma instabilities [Bla21].

One other option is that the surface potential of the RW is the highest $\phi_{\mathrm{BT}} < U_{\mathrm{Pl}} < \phi_{\mathrm{RW}}$, in this case, the electrons would leave over the RW and ions over the beam tube and DPS dipole electrodes.

When the potentials are approximately equalized $\phi_{\mathrm{BT}} \approx U_{\mathrm{Pl}} \approx \phi_{\mathrm{RW}}$, the ions can leave via the DPS dipole electrodes as well as via the RW. As in the previous case, the electrons also flow off via the RW and it is expected that under these conditions the plasma is predominantly flat and accordingly the spacial inhomogeneities are at their minimum.

Without a longitudinal electric field, the charged particles have a longer stay time and are more likely to recombine. This reduces the rate of outgoing particles, which presumably produces a peak in the current measurements. (see section 5.1.3 and 5.3.5).

The only possibility to minimize the inhomogeneities that remains is to change the RW bias to influence the plasma potential, it is therefore necessary to know at which RW voltage the plasma potential is flat.

4.3. Optimal rear wall voltage and absolute plasma potential

Now the bias voltage of RW can be set to equalize RW and beam tube potentials to minimize the inhomogeneities of the plasma potential as desired. By using equations 4.7 and 4.8 with $U_{\mathrm{BT}} = 0$ as the reference voltage for all purposes in KATRIN one obtains:

$$U_{\mathrm{opt}}(t) = \frac{\Phi_{\mathrm{RW}}(t)}{e} - \frac{\Phi_{\mathrm{BT}}(t)}{e} = \frac{\Delta\Phi_{\mathrm{RW-BT}}(t)}{e} \; . \tag{4.9}$$

At this voltage, called the optimal RW voltage a homogeneous plasma potential is expected. The derived optimal RW voltage can now be used to define the absolute plasma potential.

Since a change in the RW voltage does not translate one-to-one into a change in the plasma potential [Fri+19], an empirical quantity, the coupling strength is introduced:

$$\Delta U_{\mathrm{Pl}} = c \cdot \Delta U_{\mathrm{RW}} \; . \tag{4.10}$$

The coupling can be measured with two different methods, which observe the energy scale as a function of the RW voltage: PRO-KATRIN and krypton calibration electrons.

PRO-KATRIN consists of three different measuring steps:

- **RW-scan:** In this measurement, the relationship between the step-wise adjusted RW voltage and the FPD rate is measured, keeping the retarding potential U_{ret} in the MS constant in each case.
- **MS-scan:** Now the retarding potential is adjusted step-wise at a fixed RW voltage. The variation of the FPD rates is then compared with the obtained variation from the RW-scan. From the comparison of both measurements, the coupling between RW and the plasma potential can be determined.
- **Deep MS-scan:** Here, a scan is performed deep in the beta spectrum, changing the retarding potential in defined steps at a fixed RW bias. Subsequently, the radial distribution of the endpoints can be determined from the performed fits. With the previously performed RW and MS scan, the radial endpoint distribution for all RW voltages can now be determined.

A more detailed description of the measurement and analysis process of PRO-KATRIN can be found in the PhD thesis of Fabian Friedel [Fri20].

The coupling can be divided into the following sections:

- **Good coupling:** Being in the region of good coupling $c \approx 1$, the plasma potential follows the RW bias.

- **Bad coupling:** The RW bias has a weaker influence on the plasma potential in the range of $0 < c < 1$ and in the radial direction of the beam tube the influence becomes stronger.

- **Decoupled:** With $c = 0$ the plasma potential does not follow the RW bias at all, there is a small remaining coupling of about 5 %, but not significant. Decoupling occurs at high negative but also at high positive RW voltages.

Using the coupling constant, the absolute plasma potential can now be defined.

With the effect that the plasma aims to reach an equilibrium potential between its boundaries, there should accordingly be a RW voltage at which all potentials are equalized: $\phi_{\mathrm{RW}} = U_{\mathrm{Pl}} = \phi_{\mathrm{BT}}$. Using equations 4.7 4.8 for the surface potentials, two reference values $U_{\mathrm{Pl}} = -\Phi_{\mathrm{BT}}/e$ and $U_{\mathrm{RW}} = \Delta\Phi_{\mathrm{RW-BT}}/e$ are obtained [Kle+ep].

Now using 4.10, this leads to the equation for the absolute plasma potential:

$$eU_{\mathrm{Pl}} = -\Phi_{\mathrm{BT}} + c \cdot \left(eU_{\mathrm{RW}} - \Delta\Phi_{\mathrm{RW-BT}}\right) . \tag{4.11}$$

This model only considers averaged boundary work functions, which can also be time-dependent due to various effects on the surfaces.

As can be seen from the equation 4.11, the absolute plasma potential is dependent on work function differences of the boundaries. Furthermore, this work function difference can be compensated with a RW bias, so only the work function of the beam tube would define the plasma potential.

If variations in the plasma boundaries occur, spatial inhomogeneities in the plasma potential will result. Accordingly, it is important to minimize them by adjusting the RW voltage to the optimal RW voltage.

Optimal RW voltage with PRO-KATRIN

The optimal RW voltage can be measured with PRO-KATRIN. The deep MS-scan is used for this purpose. After measuring deep in the spectrum at a fixed RW reference voltage, a ring-wise fit is performed. Because each variation of the endpoint corresponds to a change of the plasma potential, a RW voltage can be found where the slope of the radial distribution of the endpoints vanishes. For the other RW voltages, the results from the previous two steps of PRO-KATRIN, the RW scan and the MS scan can be used. The optimal RW voltage determined in this way is called Zero radial slope of E_0.

Optimal RW voltage from Krypton measurements

The optimal RW voltage can also be determined with krypton measurements. For this the gaseous $^{83\mathrm{m}}$Kr, which serves as electron source, is injected into the WGTS and co-circulated with tritium gas. With the well known quasi-monoenergetic electron spectrum, krypton offers

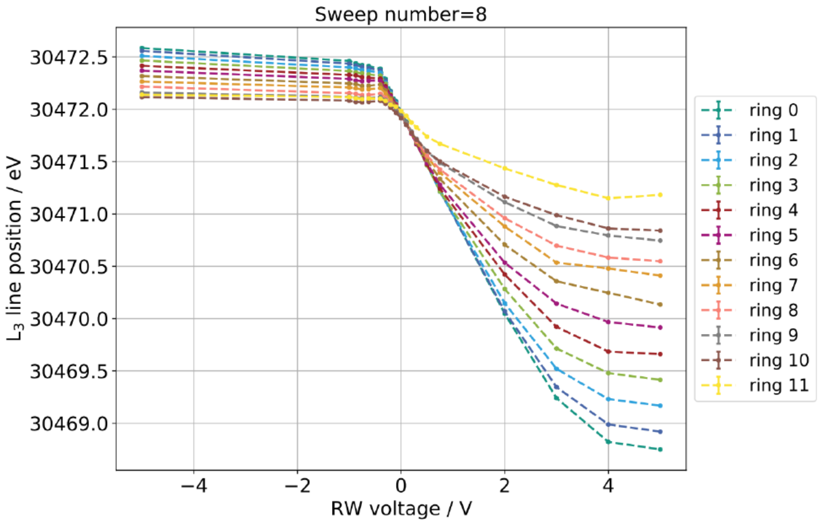

Figure 4.3.: Position of L_3 line as a function of RW voltage. At the RW voltage where the L_3 lines cross, the plasma potential is maximally radial and thus longitudinally homogeneous, which corresponds to the optimal RW voltage. Furthermore, it can also be seen that the plasma potential does not follow the RW voltage linearly and that there are different coupling regimes. The coupling also depends on the radius, which can be seen from the ring-wise visualization. Figure taken from [Ost19].

the possibility to investigate systematic effects of the plasma potential in the source, which lead to shifts or broadening in the spectrum [Mac21].

Figure 4.3 shows the position of an L_3 line from the Krypton spectrum in dependence of the applied RW voltage. It can be seen that the measured plasma potential, which is proportional to the line position, does not follow the RW voltage linearly throughout, indicating the different coupling regions. Additionally a radial dependence of the coupling can be seen by the ring dependent representation. Furthermore, the minimum radial inhomogeneity of the plasma is present where the L_3 lines cross. Because the radial and longitudinal homogeneity correlate with each other [Kuc16], this RW voltage corresponds to the optimal RW voltage. The optimal RW voltage determined in this way is called Zero radial slope of L_3 line position.

Since Krypton and PRO-KATRIN measurements require a lot of time and effort and cannot be easily carried out during neutrino mass measurements, the optimal RW voltage can be determined using currents with less effort and and this method is presented in the following chapter in section 5.1.

Chapter 5.

Monitoring of the optimal rear wall set voltage with current measurements

The plasma potential in the tritium source of the KATRIN experiment defines the starting potential for the beta electrons. Spatial variations of the plasma potential lead to a distortion of the measured beta spectrum which have an impact on the analysis of the neutrino mass. The boundaries, such as the RW and the beam tube define the plasma potential. The relationship can be expressed by equation 4.11 and is described in more detail in section 4.3. According to the definition of the plasma potential, the work function difference between the RW and the beam tube, the so-called optimal RW voltage, is included, which corresponds to the minimum spatial inhomogeneities of the plasma potential. It is therefore an important quantity to monitor the conditions in the source.

This chapter first discusses how current measurements can be used to determine the optimal RW voltage. Then it is examined how reliable this method is in comparison with detector-based measurement methods. Subsequently, the systematic and statistical uncertainties of the Zero WGTS current are quantified, which is a current-based method for determining the optimal RW voltage. Furthermore, possible correlations of the observed optimal RW voltage drift with the source parameters are analyzed. Afterwards, the observed drifts of the optimal RW voltage during several measurement campaigns are discussed with regard to the possible physical causes. Finally, it is investigated whether the observed peak in the total DPS current is also suitable for observing the drift of the optimal RW voltage. A time overview of the IU-scans used for the analyses in this thesis can be found in table 5.1.[1]

5.1. Methods for determining the optimal rear wall voltage

One method of investigating the optimal RW voltage and its variation over time uses the currents measured continuously in the WGTS. The electrons and ions in the plasma have the possibility to leave the source via the RW or via the DPS dipole electrodes. Figure 5.1 shows the measurement setup for the source currents. There are four independent currents and two currents, which are calculated from them. The three separately measured currents at the DPS dipole electrodes are

---

[1] A detailed chronological overview of the IU-scans can be found on:
`https://ikp-katrin-wiki.ikp.kit.edu/katrin/index.php/Rear_wall_voltage_scan_(IU_scan)`.

Table 5.1.: Overview of the dates of the first and the last IU-scan considered in this thesis. Except otherwise noted, the IU-scans were performed at 75 % CD.

Phase	First IU-scan	Last IU-scan	Comments
KNM3a	23.06.2020	06.07.2020	Analysis of the peak in the total DPS current in section 5.3.5, 40 % CD
KNM3b	20.07.2020	24.07.2020	Analysis of the peak in the total DPS current in section 5.3.5
KNM3test	04.08.2020	05.08.2020	Drift analysis of IU-scans in section 5.3
KNM4	01.09.2020	29.11.2020	Drift and systematic analysis of IU-scans in section 5.3 and 5.2, Excluded T+Kr with 40 % CD
KNM5a	05.03.2021	13.04.2021	Drift analysis of IU-scans in section 5.3
KNM5b	27.04.2021	05.05.2021	Drift analysis of IU-scans in section 5.3
KNM5c	10.05.2021	24.05.2021	Drift and systematic analysis of IU-scans in section 5.3 and 5.2
KNM5Kr	10.06.2021	26.06.2021	Drift analysis of IU-scans in section 5.3

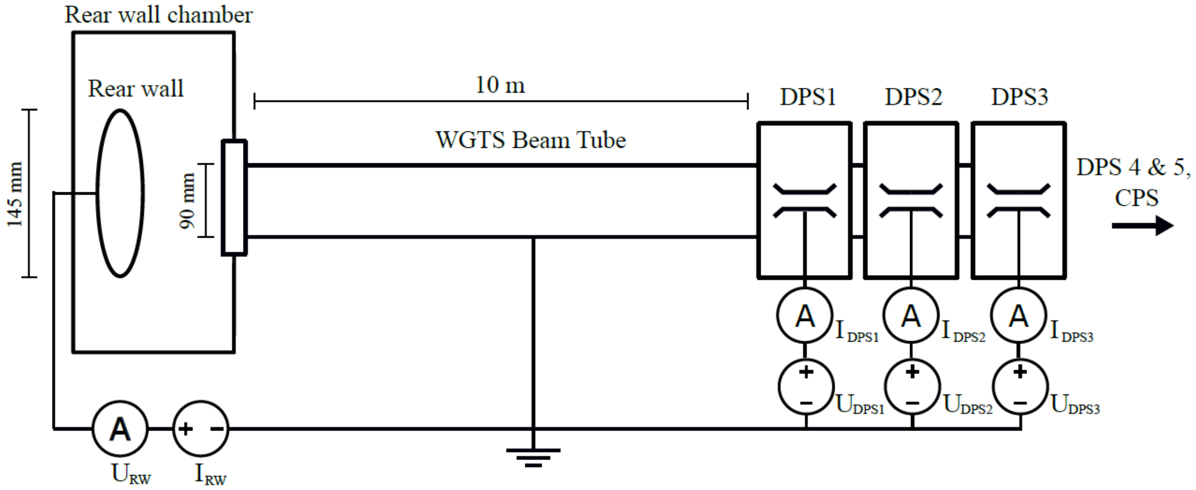

Figure 5.1.: Measuring arrangement for determining the currents from the WGTS. Depending on the polarity applied to the RW, electrons and ions are measured. Due to the applied negative voltage, the DPS dipole electrodes detect positive ions, which are removed from the source via the $\vec{E} \times \vec{B}$ drift. Figure taken from [Bla21].

combined to total DPS current:

$$I_{\mathrm{DPS}} = I_{\mathrm{DPS1}} + I_{\mathrm{DPS2}} + I_{\mathrm{DPS3}} \ . \tag{5.1}$$

Only positive ions are measured at the dipole electrodes, whereas electrons and ions can be measured as I_{RW} at the RW, depending on the voltage setting.

After combining the total DPS dipole current with RW current, the so called total WGTS current is obtained, which represents the total measured current from the source:

$$I_{\mathrm{WGTS}} = I_{\mathrm{DPS}} + I_{\mathrm{RW}} \ . \tag{5.2}$$

Assuming that the continuity equation applies, the total detected current I_{WGTS} must correspond to the undetected current with inverse sign, which flows on the beam tube wall:

$$I_{\mathrm{WGTS}} = -I_{\mathrm{BT}} \ . \tag{5.3}$$

Considering the absolute value I_{WGTS} as the current flowing on the beam tube, in the case of vanishing current, there would be no radial electric fields inside the source. This would mean that the radial inhomogeneities of the plasma potential are minimized due to the disappearance of the electric fields. The minimization of longitudinal inhomogeneities is also given due to the correlation with radial inhomogeneities [Kuc16].

5.1.1. The characteristic current-voltage curve (IU-curve)

In order to obtain the optimal RW voltage, so-called continuous IU-scans are performed. A triangular voltage ramp is applied to the RW and a defined RW voltage range is scanned. During the IU-scan a distinction is made between upward sweeps and downward sweeps, depending on whether the voltage is currently on the rising or falling ramp. At the same time, $I_{\mathrm{DPS1,2,3}}$ and I_{RW} are measured. An example of IU-curves can be seen in figure 5.2.

The Pancreas analysis code can now be used to download the currents and to extract the optimal RW voltage U_{opt} from the total WGTS current by determining the zero crossing. In the following sections of this thesis, the optimal RW voltage determined by this method is also referred to as Zero WGTS current. With this method, the optimal RW voltage can now be monitored in neutrino mass measurement phases between the individual beta scans. Based on these fast measurements of about 15 min, the RW bias can be adjusted.

One reason why special emphasis is given to the distinction between upward and downward sweeps is the hysteresis observed between both sweeps as a systematic effect of the IU-curve during an IU-scan. A possible physical reason could be charging effects due to dielectric patches leading to a change of the effective surface potential [Fri20]. The RW bias compensates this change and a characteristic shift occurs (see appendix B.1).

5.1.2. Comparison between detector- and current-based determination of optimal rear wall voltage

To verify the reliability of the Zero WGTS current method for the determination of the optimal RW voltage, krypton measurements can be used. A brief introduction of krypton measurements and determination of optimal RW voltage can be found in chapter 4.3. At the RW voltage where

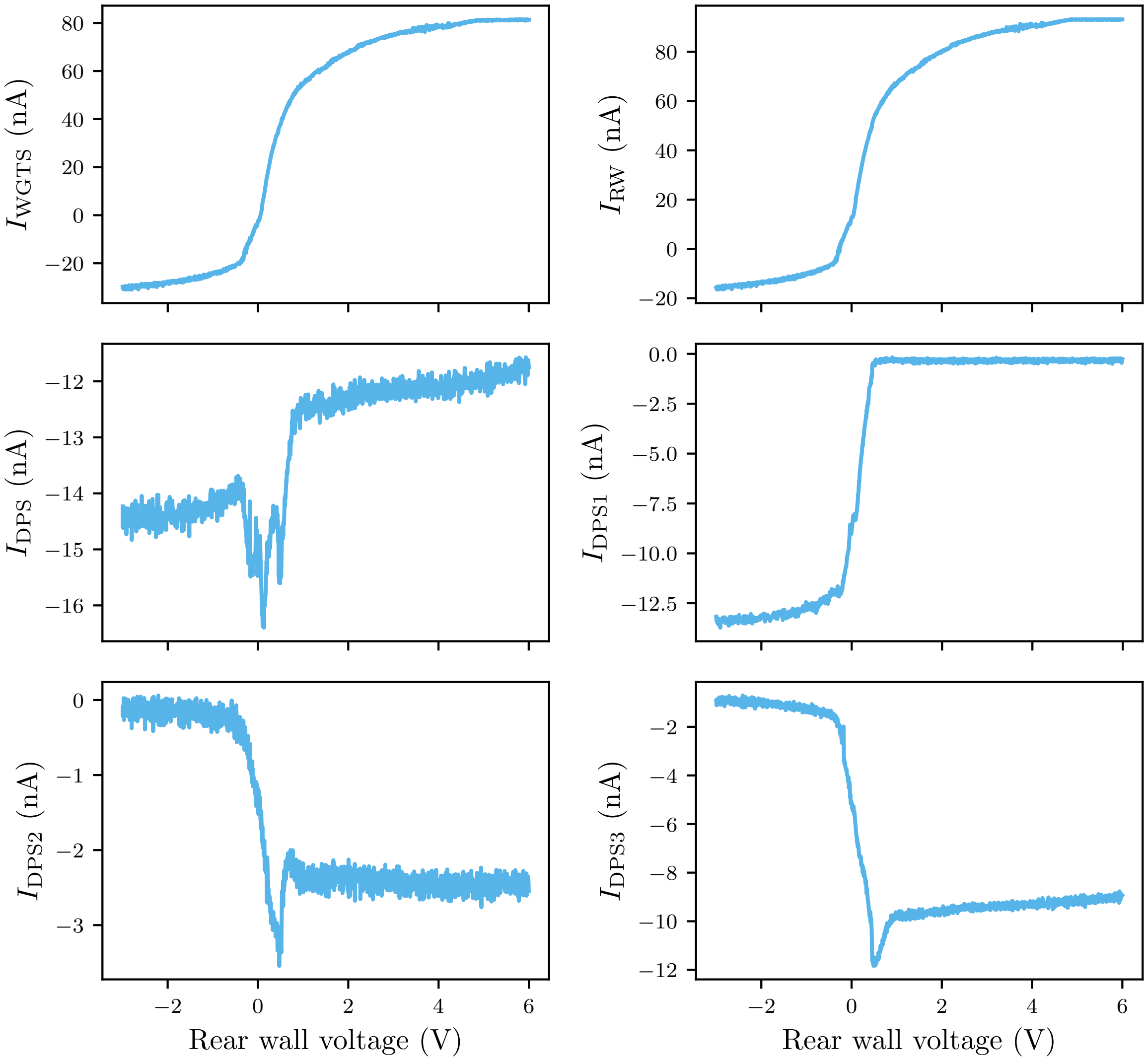

Figure 5.2.: Currents from the IU-scan of the 05.06.2020 during KATRIN neutrino mass measurement phase (KNM)3. Example of IU-curves of the scan, which was carried out at a source temperature of $T = 80\,\mathrm{K}$, with directly measured currents $I_{\mathrm{DPS1,2,3}}$ and I_{RW} and with equations 5.15.2 calculated currents I_{DPS} and I_{WGTS}. The nominal column density is about 38 %. It can be clearly seen that the curve saturates at 6 V, where only electrons hit the RW. The optimal RW voltage can be determined at vanishing total WGTS current.

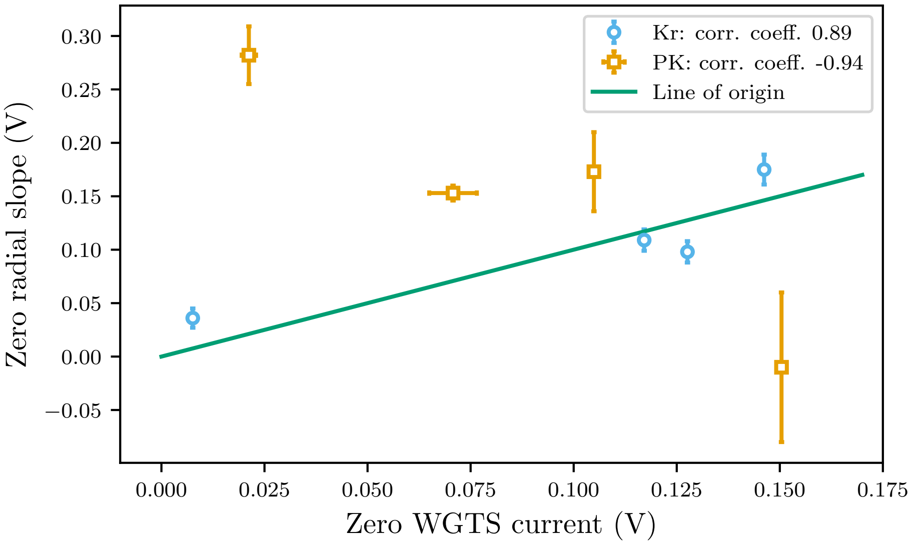

Figure 5.3.: Comparison of detector-based and current-based optimal RW voltages during KNM3. The optimal RW voltage, which was determined with discrete IU-scans in KNM3 during PRO-KATRIN and Krypton measurements is compared with optimal RW voltage determined with two different detector-based methods. There is good agreement with the the krypton measurements and no agreement with PRO-KATRIN. The deviation in PRO-KATRIN could come from the use of a third measurement step, the deep scan (see chapter 4.3), where time passes between the first two steps during which surfaces conditions can drift and distort the determination of optimal RW voltage. In addition, there may be other systematic effects in the deep spectrum that are not considered in the fit model.

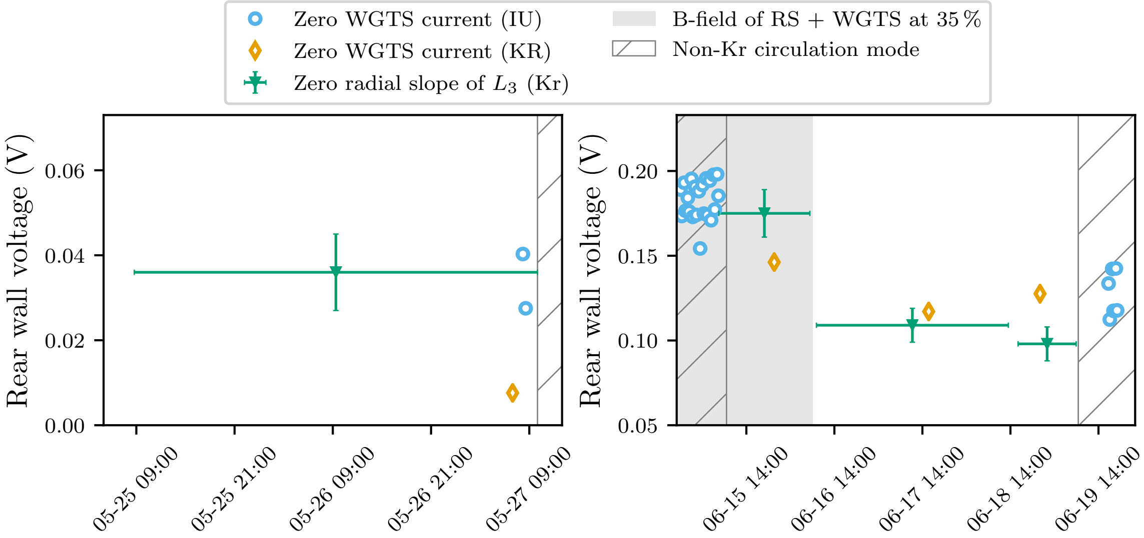

Figure 5.4.: Consistency of step-wise and continuous IU-scans compared to Zero radial slope of L_3 during KNM3.

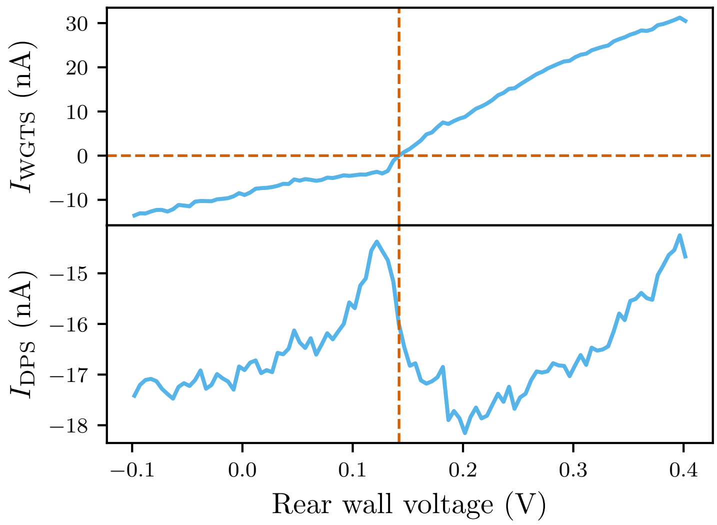

Figure 5.5.: Example sweep of total DPS dipole current peak from 29.06.2020 during KNM3a. The total DPS current peak appears near the Zero WGTS current, here marked with dashed lines.

all L_3 lines cross, a flat plasma potential is expected. In figure 5.3 the detector-based methods for the determination of the optimal RW voltage are compared with the step-wise IU-scan, which is obtained automatically from the voltage changes during the krypton measurements. The results from the krypton measurements agree well with the step-wise Zero WGTS current method. A disagreement is observed with the PRO-KATRIN measurement. Since the determination of the Zero radial slope of E_0 requires an deep scan (see chapter 4.3) as an additional step in the PRO-KATRIN measurement to obtain the ring-wise distribution of the absolute endpoint E_0, further drifts of the surface configurations may occur in the time that passes between the deep scan and the RW and MS scan, which would lead to the deviation for PRO-KATRIN shown in figure 5.3.

However, IU-scans performed step-wise during krypton measurements cannot be directly compared to continuous IU-scans, which are actually performed between beta scans. The reason for this is that in the step-wise IU-scans the surface properties of the boundaries have the possibility to equilibrate. Nevertheless, as can be seen in figure 5.4, the subsequent continuous IU-scans and the corresponding optimal RW voltages are in good agreement with the step-wise measurement values.

5.1.3. Total DPS dipole current peak

Another possible method to find the optimal RW voltage is to determine the RW voltage of the characteristic peak in the total DPS current (see. fig. 5.5). The ‘peak’ actually corresponds to a decrease of the measured ions in the DPS dipole electrodes. The local minimum of ions is taken as an indication that at this voltage the recombination rate of charged particles in the source is high.

For the optimal RW voltage it is expected that the existing electric field is too small to draw electrons or ions out of the plasma. Accordingly, the charge carriers have a longer time of stay and a higher probability to recombine in the plasma. The position of the total DPS peak is observed near the Zero WGTS current, which is to be expected because at the optimal RW voltage the current on the beam tube walls vanishes.

5.2. Systematic effects of the IU-curve

In this section, the possible uncertainties on the optimal RW voltage from a single IU-scans are discussed. Subsequently, the obtained uncertainties are compared to the experimental data from KNM4 and KNM5 under the assumption of a linear drift

5.2.1. Calculation of uncertainties on individual data points of the optimal rear wall voltage

The zero crossing of the total WGTS current is calculated sweep-wise in the Pancreas analysis code. The algorithm first searches for sign changes in the total WGTS current of individual sweep. The optimal RW voltage is then linearly interpolated using the nearest current measurement data points where the sign change occurred. Since there can be several zero crossings due to noise in the individual sweeps, the mean value of all zero crossings is then calculated.

In the following, the uncertainties on the determined optimal RW voltage are discussed:

- **Ramp speed**: A systematic effect can occur due to the finite ramp speed of the RW voltage and the associated resolution. It is usually about $2\,\mathrm{mV\,s^{-1}}$ during a sweep. However, linear interpolation is a good approximation for the selected resolution, the effects due to the ramp speed can be neglected, assuming that there are no spikes in the currents.

- **Spikes**: Potential sources of uncertainty are spikes in the current measurements and the associated uncertainty is difficult to quantify. Nevertheless, larger spikes, which can significantly change the optimal RW voltage, are already being removed with the z-score method: Data points deviating from the mean of a defined narrow window in a sweep by $5\,\sigma$ are removed from the total WGTS current.

- **Measuring devices**: Additionally, there are uncertainties caused by the current measuring devices. The RW currents are measured with a *Keithley-6487* and the DPS dipole currents with a *rbd 9103*. The accuracy and offset values required for the calculation were taken from the data sheets of the corresponding devices and can be found in appendix C. The measurement range for the RW and DPS1,2 is 200 nA and for the DPS3 the range is 20 nA. By using propagation of uncertainty, this gives an uncertainty on the total WGTS current from the devices of $\pm\,0.17\,\mathrm{nA}$.

  For the calculation of the uncertainty on the optimal RW voltage, typical values of the measured current near the zero crossing during KNM4 and KNM5 were used. The approximate value for the RW is 40 nA. For the dipole electrodes DPS1,2 this results in 30 nA and for DPS3 one gets 10 nA. To convert the currents into voltages, the slope of the IU-curves are fitted for the KNM4 and KNM5 in the vicinity of the optimal RW voltage. For this purpose, the IU-curves were used, which were also considered later in the calculation of the statistical uncertainty (see fig 5.6 and 5.7). Then the median of the fitted slopes is used to obtain the uncertainty on the voltage. For KNM4 and KNM5 this results in an uncertainty of about $\sigma_{\mathrm{dev}} = \pm\,1\,\mathrm{mV}$.

- **Noise**: Another factor influencing the calculation of the optimal RW voltage is the intrinsic noise of the currents. A rough estimation can again be carried out with a linear fit of the $I_{\text{WGTS}}(U_{\text{RW}})$ curve by looking at the corresponding residuals. For this purpose, the curve was fitted at large positive voltages, where a predominantly linear curve can be observed. The translation into voltage can again be carried out with the already calculated slopes near the optimal RW voltage. For the KNM4 and KNM5 phases this results in an uncertainty σ_{noise} on the optimal RW voltage of about 1 mV for KNM4 and 1.5 mV for KNM5. The total systematic uncertainty σ_{sys} from the noise and the ampere meter can then be calculated by summing the squares of the individual uncertainties:

  $$\sigma_{\text{sys}} = \sqrt{\sigma_{\text{dev}}^2 + \sigma_{\text{noise}}^2}\ . \tag{5.4}$$

  The results can be seen in table 5.2. However, if there is no plasma in the source, the intrinsic noise is smaller, accordingly the noise in the current measurements must be plasma induced.

- **Leakage currents**: The previous points considered the accuracy of the optimal RW voltage, leakage currents in the DPS section but also in other unknown segments could cause a deviation relative to the true value. Assuming that this shift is constant, this would have no influence on the neutrino mass measurement, because only the time-dependent drifts of the optimal RW voltage are relevant.

- **Hysteresis**: Another source of uncertainty is the hysteresis, which occurs between upward and downward sweeps during an IU-scan (see section 5.1.1). However, due to the reduced scan range, the uncertainty during KNM4 and KNM5 is negligible.

5.2.2. Investigation of statistical uncertainty with linear model assumption

The optimal RW voltage measured with the IU-scans during KNM4 and KNM5 shows a drift over long time periods. There is also a characteristic burn-in phase observed after restart of the tritium circulation. This drifts corresponds to a drift of the work function differences of the plasma boundaries and is described in more detail in section 5.3. In this section, using the systematic uncertainty calculated in section 5.2.1, the statistical uncertainty of the IU-scans is estimated with the variance of the residuals of a fitted linear model.

For the calculation of the statistical uncertainty, phases were selected with a linear drift of the optimal RW voltage with a stable slope and with as many IU-scans as possible. A linear model is assumed because there is no physical explanation for the drift so far and this empirical model fits always very well for long-term drifts. Afterwards, the variance of the residuals is calculated. The previously discussed systematic uncertainties on the individual data points (see section 5.2.1) are included in the fit. Possible outliers, which are observed as deviations on single days are considered in the fit since a cause has not yet been determined.

Figures 5.6 and 5.7 show the corresponding sections from the KNM4 and KNM5c phases. A linear fit to the KNM4 data yields a significant drift, but a few significant outliers are visible. However, correlations with other parameters could not point to a clear origin. From KNM5c a region was chosen where the drift of the optimal RW voltage is less significant, here the fewest systematic effects are present, so that the statistical uncertainty can be well estimated.

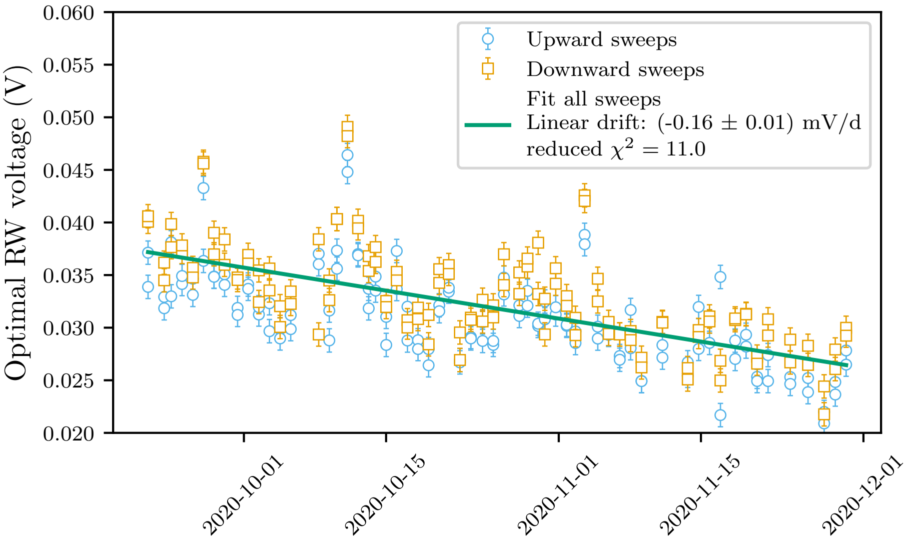

Figure 5.6.: Significant drift of the optimal RW voltage during KNM4 fitted with a linear model. In the linear course of the KNM4 phase clear structures are visible, whose origin is not yet clarified. The standard deviation of the residuals are shown in table 5.2.

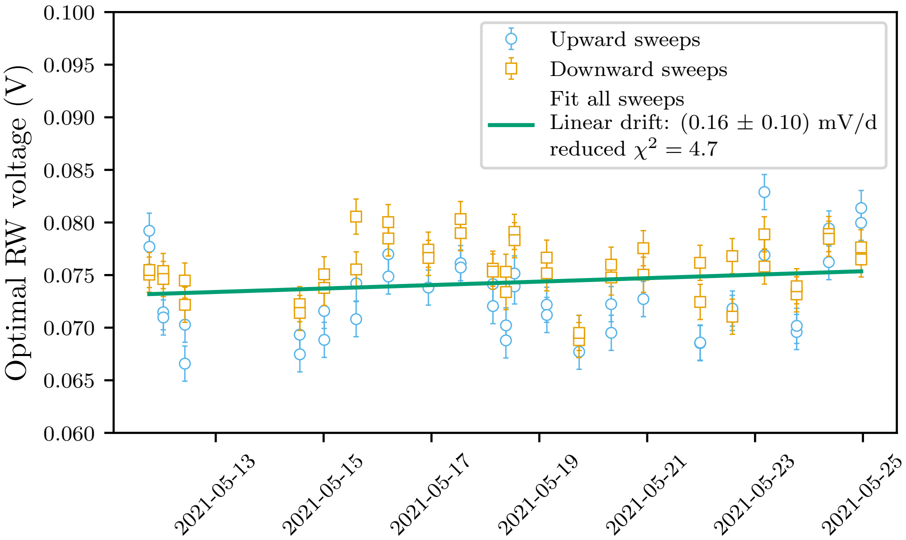

Figure 5.7.: Drift of the optimal RW voltage during KNM5c fitted with a linear model. Because of the less significant drift, the fit should suffer from fewer systematic effects than the fit during KNM4 in figure5.6. Comparing the reduced χ^2 of 11 during KNM4, the linear model in KNM5c fits better with $\chi^2 = 4.7$. The statistical uncertainty obtained using the fit are more reliable estimates. The standard deviation of the residuals are shown in table 5.2.

Table 5.2.: Systematic and statistical uncertainties of optimal RW voltage. In the second column is the estimated systematic uncertainty σ_{sys} of the sweep-wise optimal RW voltage values. These values are used to estimate, with an assumed linear model, the statistical uncertainty σ_{res} of the optimal RW voltage for individual sweeps during KNM4 and KNM5c from the corresponding residuals.

Phase	σ_{sys} (mV)	σ_{res} (mV)		
		Up sweeps	Down sweeps	All sweeps
KNM4	± 1.11	± 3.34	± 3.65	± 3.68
KNM5c	± 1.67	± 2.82	± 3.15	± 3.52

Nevertheless, the linear model is not optimal, but it is possible that the systematic uncertainty on the individual data points was underestimated. The standard deviation of the residuals σ_{res} obtained from the fit can be taken from table 5.2. The uncertainty is about $\sigma_{\mathrm{res}} = 4\,\mathrm{mV}$ and it is slightly larger compared with the systematic uncertainty calculated in chapter 5.3, however, the order of magnitude are matching.

The statistical uncertainties of about 15 min long IU-scans are negligible for example compared to the sensitivity of approximately $40\,\mathrm{meV}^2$ per one hour run on the krypton N-line, which corresponds to determination of the plasma potential. The sensitivity only applies in krypton-V due to the high krypton activity and is even larger at other occasions with smaller statistics. Both observables will later be used in the neutrino mass analysis.

5.2.3. Correlation of the optimal rear wall voltage with source parameters

To investigate possible causes of the systematic effects during the drift, the correlations of the source parameters with the optimal RW voltage are investigated in this section.

Column density and optimal RW voltage

First, the possible relationship between the column density and the optimal RW voltage during KNM4 is investigated. The column density was determined by Fabian Block and Christoph Köhler with the FPD300-90 method, using two monitoring points at 90 eV and at 300 eV. The results are preliminary and for further details regarding the determination of the column density can be found in the PhD thesis of Fabian Block [Bloep].

The column density values are available for individual neutrino mass runs, and since the optimal RW voltage is measured with the IU-scans between the beta scans, the data points must be re-sampled. For this purpose, an interval of 15 h was chosen, which is the minimum time interval between the IU-scans during the beta scans in KNM4.

Figure 5.8 shows the averaged values of optimal RW voltage and re-sampled values of column density. The difference in column density uncertainties at the beginning of the measurement phase comes due to the different MTD.

A vanishing correlation of the two quantities can be observed in figure 5.10. Therefore, the column density cannot cause the drift of the optimal RW voltage. In addition, it is unlikely

---

[2] Value taken from Table 2 of ”The Krypton V campaign - measurement proposal”.

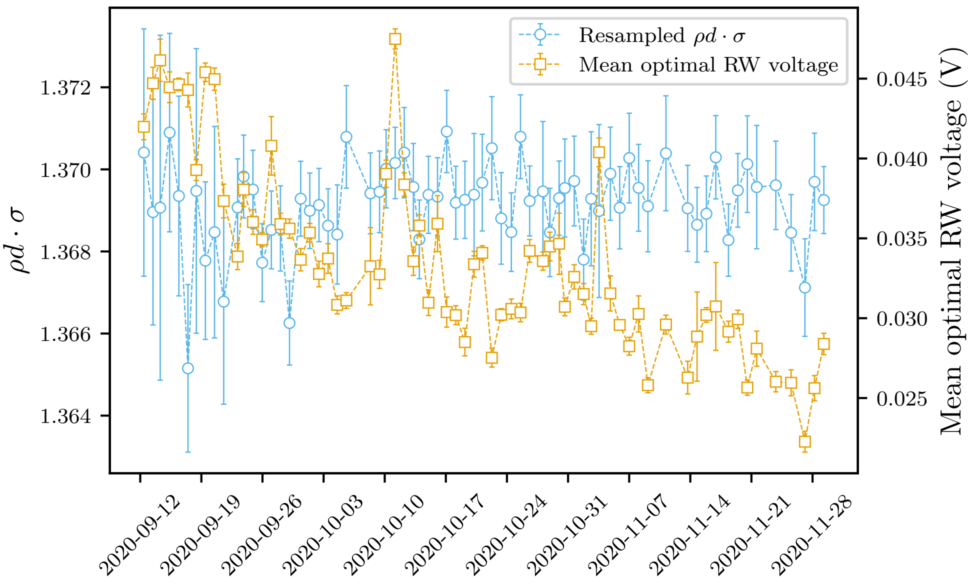

Figure 5.8.: Column density compared with the optimal RW voltage drift during neutrino mass measurements in KNM4.

that the systematic structures in the drift of the optimal RW voltage are caused by the column density.

Tritium purity and optimal RW voltage

The tritium purity ϵ_{T} indicates how many tritium atoms are in the gas relative to the total number of isotopologues when injected into the WGTS. The monitoring of the tritium purity is performed with laser Raman spectroscopy (LARA). Since impurities like hydrocarbons can accumulate on the surfaces of the boundaries, this could lead to changes in the work function and thus to a drift of the optimal RW voltage.

The continuously measured tritium purity was re-sampled to be compared with the measurements of the optimal RW voltage. For this purpose, as for the correlation with the column density, a time interval of 15 h was also chosen and the corresponding values were averaged.

The comparison can be seen in figure 5.9. Since there are also values for the tritium purity in the burn-in phase, it was also compared with the optimal RW voltage. During the burn-in phase there is a clear correlation which can be seen in figure 5.10. In contrast, the correlation worsens considerably after the burn-in phase. Around 09.10.2020 and at the end of the phase, there is sporadic good agreement in the course of the data.

It is quite possible that there is a systematic correlation between the two observables at least during the burn-in phase, indicating that adsorbed impurities such as hydrocarbons on the RW or on the beam tube are causing the change of work functions. However, no clear statement about the long-term drift is possible.

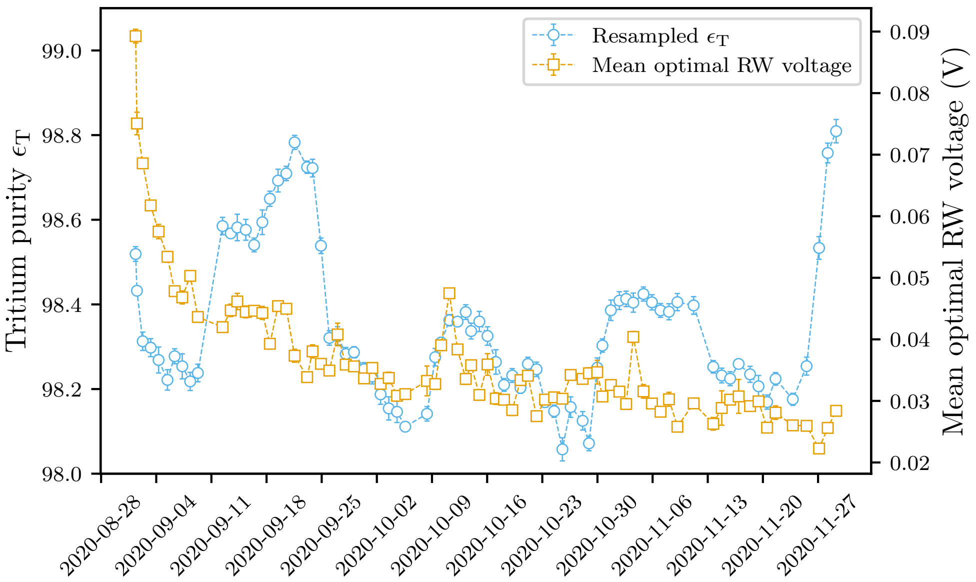

Figure 5.9.: Tritium purity compared with the optimal RW voltage drift during neutrino mass measurements in KNM4. During the burn-in phase in KNM4, the tritium purity shows a behavior similar to the optimal RW voltage. Afterwards, only a slight correlation can be seen.

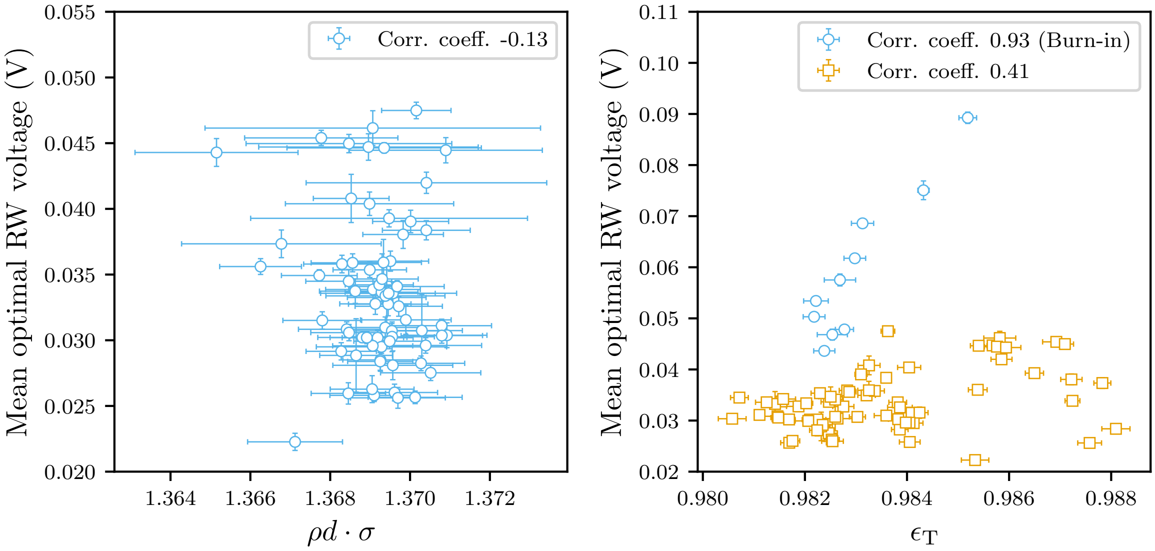

Figure 5.10.: Correlation between the source parameters and the optimal RW voltage. The correlation between the preliminary column density during KNM4 and the optimal RW voltage (left) is negligible. Thus, it is unlikely that the systematic structures of the drift originate from the fluctuation of the column density. The correlation with tritium purity (right) is strong in the burn-in phase but becomes much smaller in the phase of approximately linear optimal RW voltage drift.

5.3. Drift analysis with periodic IU-scans

At the beginning of each neutrino mass measurement phase, it is necessary to determine the optimal RW voltage, in order to create a homogeneous plasma potential. The optimal RW voltage determined with the IU-scan then is applied as the bias voltage of the RW. In the subsequent monitoring of the optimal RW voltage with the IU-scans, long-term drifts were observed in the various KNM phases. Therefore, it is necessary to constantly perform IU-scans to possibly adjust the RW bias. It is adjusted only if the optimal RW voltage has drifted out of the optimal window of about $50 - 70\,\mathrm{mV}$ more positive as the optimal RW voltage to allow the electrons to leave the WGTS. The continuous monitoring is also used for the analysis, to correct for drifts.

5.3.1. Drifts during neutrino mass measurements

If a new neutrino mass measurement phase is initiated and the tritium is injected, a so-called burn-in phase is observed with the IU-scans immediately afterwards, the physical origin of which is discussed in chapter 5.3.3. The first observation of the burn-in phase was after the change of the column density from 40 % to 75 % in the KNM3b phase. The course can be approximately described with an exponential curve. Subsequently, a transition to a linear drift of the optimal RW voltage is observed (see fig. 5.11). The characteristic was modeled with a combination of an exponential and a linear function for KNM4 and KNM5a:

$$U_{\mathrm{RW}}(t) = A \exp\left(-\frac{t - t_0}{\lambda}\right) + c\,(t - t_0) + d \ , \tag{5.5}$$

and the drift from these phases corresponds to the fit parameter c. The drifts from all other considered phases were fitted with a simple liner model.

Table 5.3 summarizes the linear drifts from different measurement phases. In addition, the average value of the measured optimal RW voltage from the last IU-scan was determined of each phase, which can also be found in the table. Starting from KNM3b, a column density of 75 % was chosen, with RW bias of 175 mV. Because the RW bias was the same as in KNM3a with 40 % CD, the new source and surface properties likely caused a drift to a new higher equilibrium value of the optimal RW voltage.

After KNM4, the RW was cleaned with ozone and free oxygen atoms created by UV irradiation at elevated pressure from ambient air so that the surface properties were significantly changed, which probably led to higher optimal RW voltages at the beginning of KNM5 (see fig. 5.17).

5.3.2. Influence of the rear wall bias change on the drift

To ensure maximum homogeneity of the plasma potential, it is important to know what causes the drift of the optimal RW voltage. At the end of the KNM3 phase, test measurements were performed to investigate how voltages at the RW affect the long-term drift. In KNM5a, the influence of the RW bias on the drift during normal operation could then be observed. In addition, there are clear observations during the krypton measurements at the end of KNM5, which are presented at the end of the section.

The test measurements were performed at 75 % column density (CD) and can be divided into three sections:

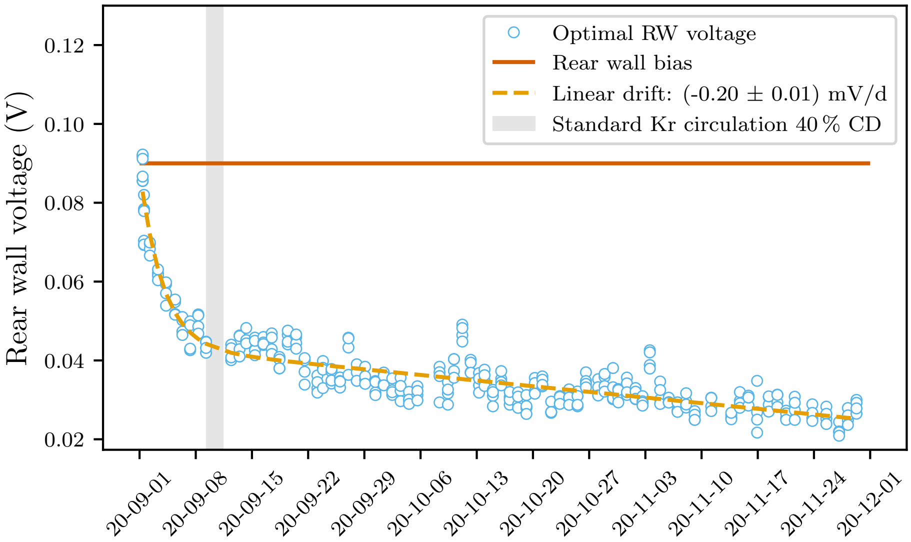

Figure 5.11.: Exponential burn-in phase followed by linear long-term drift during KNM4. A combination of an exponential and a linear model was used for the fit (see eq. 5.5). For the amplitude this results in a value of $A = (0.039 \pm 0.001)\,\mathrm{V}$ and for the time constant $\lambda = (2.84 \pm 0.23)\,\mathrm{d}$.

Table 5.3.: Linear drifts of optimal RW voltage starting from KNM3. All drifts except that of KNM3a occurred at 75 % column density. The large drift from KNM3b is likely because the equilibrium value of optimal RW voltage had not yet been achieved. In addition, the mean values of the optimal RW voltage from the last IU-scan $\overline{U}_{\mathrm{opt}}$ of the campaign are shown in the second column. For KNM4 and KNM5a the drift values were determined from a fit model composed of an exponential and linear function (see eq. 5.5) including the burn-in phase. For other phases, the burn-in phase was not considered and a simple linear model was used to determine the drift. The table does not include all IU-scans of KNM5 as used in the neutrino mass measurements.

Phase	Drift ($\mathrm{mV\,d^{-1}}$)	$\overline{U}_{\mathrm{opt}}$ (V)	U_{bias} (V)
KNM3a	0.54 ± 0.08	0.150 ± 0.004	0.175
KNM3b	3.97 ± 0.59	0.108 ± 0.019	0.175
KNM4	-0.20 ± 0.01	0.028 ± 0.010	0.090
KNM5a	-0.77 ± 0.05	0.175 ± 0.006	0.350 and 0.300
KNM5b	-1.56 ± 0.16	0.077 ± 0.012	0.300 and 0.150
KNM5c	0.16 ± 0.10	0.079 ± 0.012	0.150

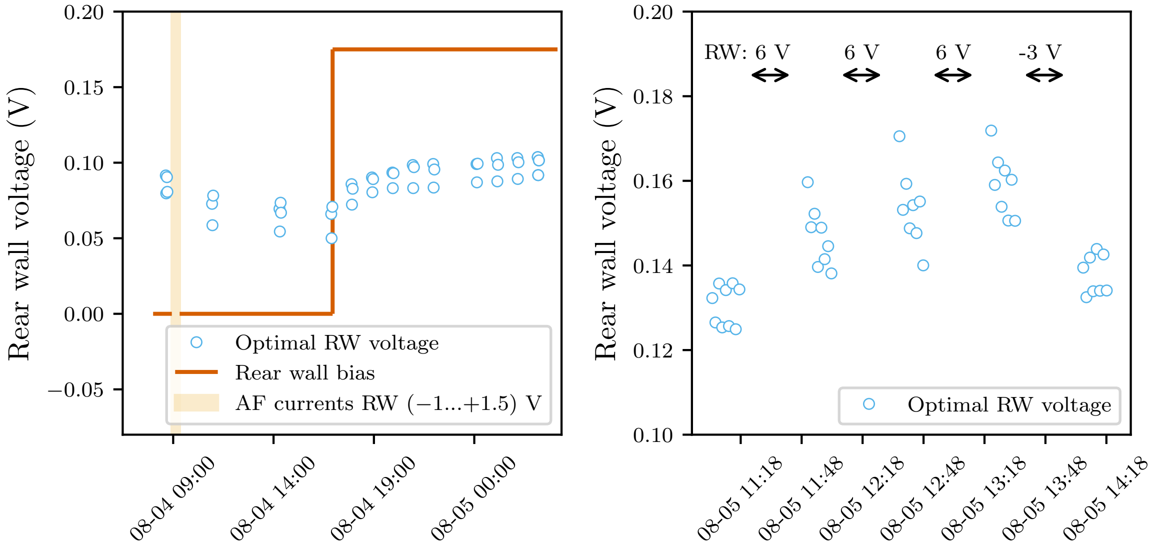

Figure 5.12.: Influence of RW bias on drift of the optimal RW voltage during test measurements in KNM3. After changing the RW voltage from 0 mV to 175 mV between the scans, the optimal RW voltage approaches a different equilibrium value (left). When applying high RW bias and then performing IU-scans (right) the same saturation behaviour is observed. The shift between IU-scans increases and is presumably going into saturation. It can be also seen that within the IU-scans the optimal RW voltage approaches a lower equilibrium value. This is probably due to the mean value of 150 mV of the scan range (−100 ... +400) mV compared to 6 V applied for 30 min before the scan. After applying −3 V the trend reverses.

- With a RW voltage scan range of (−100 ... +400) mV, approximately one scan per hour was performed over 15 h. Between the scans the RW bias was 0 mV and then at 175 mV, which was the default setting of the RW bias during KNM3a and KNM3b phases (see fig. 5.12 left). A triangular waveform of the RW voltage was applied with a period of 200 s for each scan.

- Right after that, a long IU-scan with a triangular waveform period of 3600 s was performed. This time a higher voltage scan range of (−3 ... +6) V was used (see fig. 5.13).

- A smaller range scan was performed immediately after the long period scan. Subsequently, 6 V were applied to the RW for 30 min, followed by an IU-scan. The process was repeated two additional times. This test measurement was completed with an IU-scan with −3 V applied to the RW for half an hour (see fig. 5.12 right). The IU-scans in this phase were each performed in the RW voltage range (−100 ... +400) mV with a period of 200 s.

Figure 5.12 shows the results of the test measurements. It can be clearly seen that the change of RW bias from 0 mV to 175 mV (see. fig. 5.12 left) results in a different equilibrium value being approached by the optimal RW voltage. When the equilibrium was approached, the exponential trend changes into a linear trend. The clear drift in the IU-scans in the right plot of figure 5.12 is due to the lower average voltage applied during the scan compared to the high RW bias of 6 V. Accordingly, a lower equilibrium value is approached during the scan.

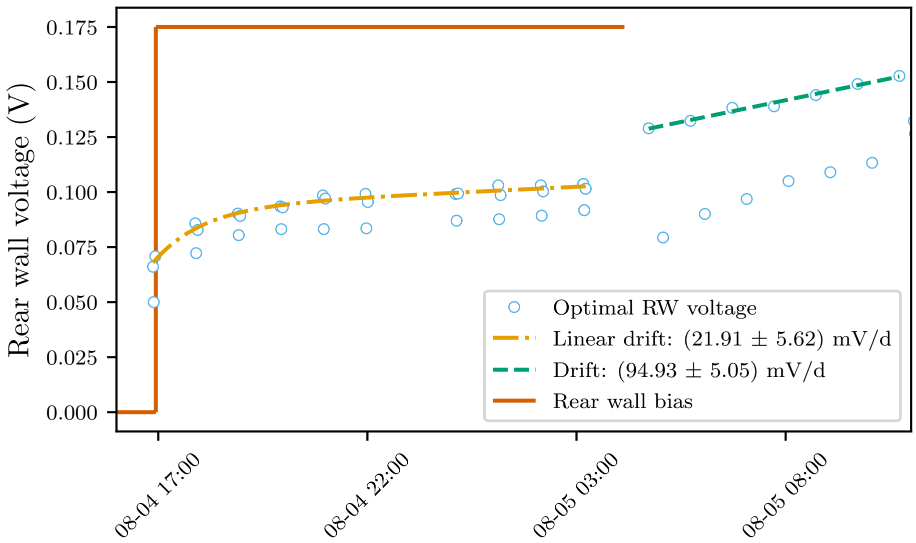

Figure 5.13.: Influence of RW scan range on drift during test measurements at the end of KNM3. After changing the RW scan range from $(-100\ldots400)\,\mathrm{mV}$ to $(-3\ldots+6)\,\mathrm{mV}$, an increase in drift of $(73.02 \pm 7.14)\,\mathrm{mV}$ with a significance of $10\,\sigma$ can be observed. In addition, an increase in hysteresis can be seen. The cause of the drift will be discussed in section 5.3.3. The fit was performed only with the downward sweeps to avoid the systematic uncertainty from the hysteresis.

Figure 5.13 also shows how the chosen RW voltage range affects the drift. There is a significant increase in drift by $(73.02 \pm 7.14)\,\mathrm{mV}$ between the values associated with the change of RW scan range from $(-100\ldots400)\,\mathrm{mV}$ to $(-3\ldots+6)\,\mathrm{mV}$ because the mean voltage during the scan is 1.5 V, much more than the set voltage before. The large hysteresis is most likely a consequence of the same drift, though it is not excluded that there is another effect (see section 5.3.3).

A significant example of the influence of the change in RW bias during running neutrino mass measurements can be seen in the KNM5b phase in figure 5.14. It can be clearly seen that after the change from 300 mV to 150 mV of the RW bias, a subsequent new distinct exponential phase occurs. Additionally, the krypton measurements running during the thesis writing process clearly show how the optimal RW voltage drifts behind the RW bias.

According to the observations, it can be summarized:

- A change in RW bias affects the optimal RW voltage: after the change, a drift is observed
- The drift tends to move in the direction of the voltage change
- The slope of the drift scales with the magnitude of the voltage change
- The drift is reversible

In addition, drifts within the IU-scans are observed, which probably have the same cause as the drifts of the individual IU-scans. Furthermore, besides the drifts that happen due to the change of RW bias, there are drifts observed in the burn-in phases, which could have a common physical cause.

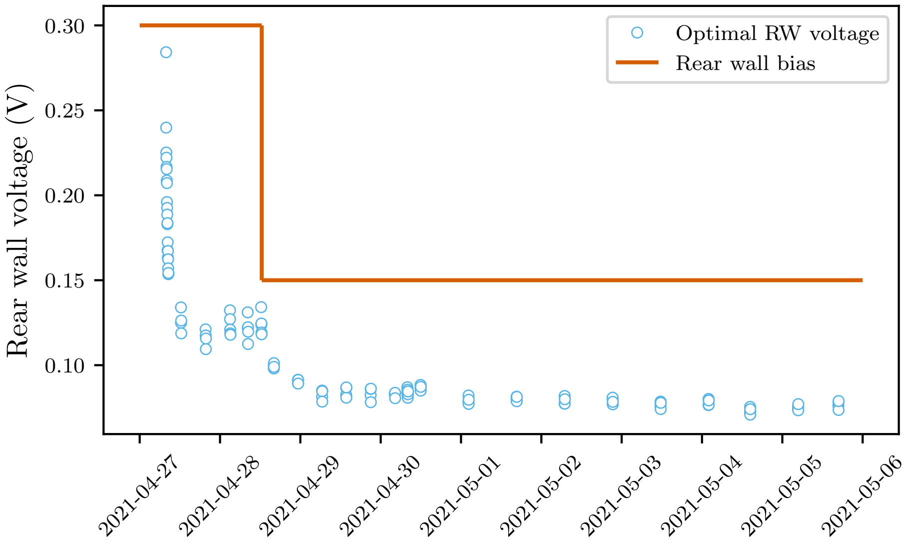

Figure 5.14.: Influence of the change in RW bias on the optimal RW voltage drift during KNM5b.

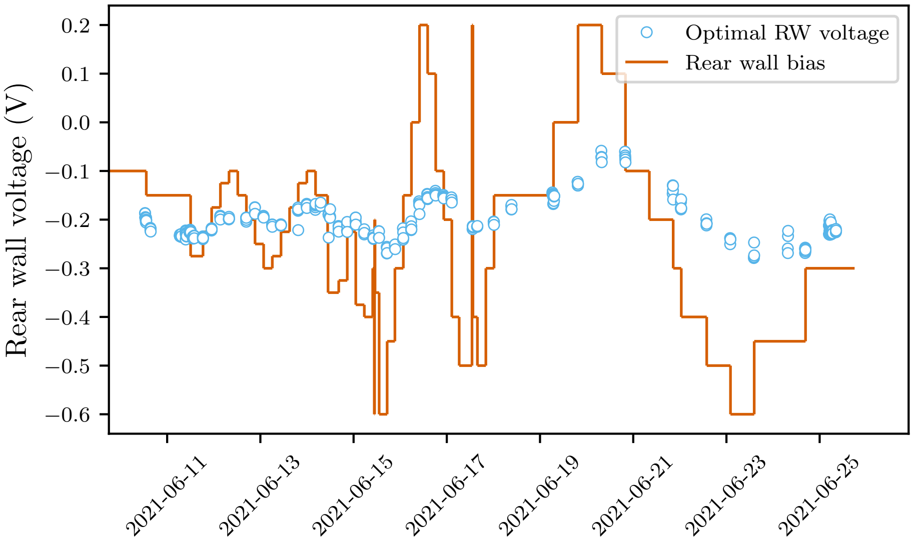

Figure 5.15.: Influence of RW bias changes on the optimal RW voltage during krypton measurements at the end of KNM5.

5.3.3. Cause of the drift

The previous section dealt with the evidence that RW bias has an effect on optimal RW voltage. It was shown that a drift is observed after the voltage change. This section is concerned with the physical origin behind the drift. The following two competing physical models, which have not been distinguished so far, are candidates for the cause of the drift:

- **Charging** refers to the effect of inadvertent insulating patches that can be located either on the surface of the RW, the beam tube or on both. These patches can be charged by ions or by electrons which leads to a change in the effective surface potential. The change in the effective surface potential then lead to a shift in the optimal RW voltage. These dielectric patches or films can be caused due to impurities with hydrocarbons [DAr74; FA03].

- **Adsorption** is an effect whereby, for example, hydrocarbons stick to the surface of the boundaries. Unlike charging, the work function of the material changes and the charge carriers can flow through the metal without accumulating on the surface. In this case, the change in work function causes the change in optimal RW voltage [Lüt13].

The influence of the change of the RW bias on the drift, as observed in the test measurements at the end of KNM3 (see fig. 5.12) and in KNM5b (see fig. 5.14), could come from adsorption as well as from charging effects. It is also difficult to say whether the burn-in phase is based on the same physical effect as for the change in RW bias.

There is good evidence that, at least in the burn-in phase of KNM5 (see fig. 5.17), the cause of the drift is due to adsorption of ions. Between KNM4 and KNM5 the tritium coverage of the RW was reduced significantly by exposure to ozone and free oxygen atoms. Measurements were made at the beginning of KNM5 to determine whether neutral gas or ions dominate adsorption at the RW and thus to clarify which type of particle is predominantly responsible for the increase in activity. With the shift of the magnetic flux tube to a small area of the RW to distinguish the interaction of ions from neutral gas, there is evidence that the ions contribute 20 times more, with an uncertainty of 1 % per pixel (see fig. 5.16), than the neutral gas to the activity of the RW and adsorb more effectively on the RW surface. The results can be found in the PhD thesis of Max Aker [Akeep].

Another indication is the large amplitude of the burn-in phase before KNM5 compared to KNM4, where the optimal RW voltage was predominantly in the range between 20 mV and 100 mV (see fig. 5.11). At the start of KNM5, the optimal RW voltage was about 700 mV. The difference of about 600 mV would match the difference between the measured work function of the RW before KNM1 and KNM5, assuming that the work function has not changed much during KNM1 to KNM4. This suggests that the drift was predominantly from the RW in KNM5 at least in the burn-in phase.

The comparison of the observed duration of the burn-in phases in KNM5 could provide further evidence for the adsorption model. At the transition from KNM5a to KNM5b (see fig. 5.17), the corresponding burn-in phase is faster, which could indicate that the deeper adsorbents in the RW have remained in the material and only changes at the top layer after the empty source cause the visible and fast decrease in optimal RW voltage. Moreover, the equilibrium value of optimal RW voltage after the burn-in phase in KNM5b is lower than the optimal RW voltage values at the end of KNM5a with the same RW bias. This could indicate that after adsorption, the ions diffuse into to deeper layers. However, it could also be that without the change in RW bias in KNM5b, the equilibrium value would have returned to the optimal RW voltage values

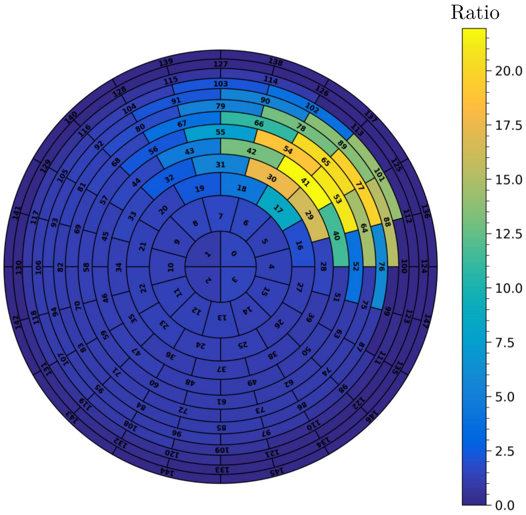

Figure 5.16.: Comparison of the RW activity caused by ions and neutral gas at the beginning of KNM5. It shows the ratio of the RW activity with respect to the mean value obtained from the pixels of the lower left quarter. The shifted flux tube is located in the upper right corner, only there the ions impinge on the RW. The preliminary analysis of Simon Tirolf shows that the activity caused by ions is 20 times larger, with an uncertainty of 1 % per pixel, than the activity from the neutral gas. Figure and analysis done by Simon Tirolf.

at the end of KNM5a as after change from KNM5b to KNM5c, where the last IU-scan achieved approximately the same mean optimal RW voltage as in the last IU-scan of the previous phase.

In general, with respect to the physical cause of the drifts, whether it is charging or adsorption could not be fully clarified. It is likely that adsorption on the RW during burn-in phase in KNM5 is involved, but it is not possible to distinguish whether it is a global change in work function or charging of insulating patches.

5.3.4. Influence of the rear wall bias change on the endpoints

The qualitative analysis in section 5.3.2 showed that a change in the RW bias causes a drift in the optimal RW voltage. This section quantitatively examines from which boundary the observed drift originates. For this, the endpoints that depend on the absolute plasma potential via the equation 4.11 are investigated:

$$E_0 = eU_{\mathrm{Pl}} + A_{\mathrm{off}} \ , \tag{5.6}$$

with endpoint E_0 and the effective offset value A_{off}. Scan-wise averaged optimal RW voltages of KNM5b and window blind endpoints $(300-41\,\mathrm{eV})^3$ were used for the analysis. For comparability with the window blinded endpoints, the optimal RW voltage was linearly interpolated to the start times of the used runs.

In figure 5.18 it can be seen that there is a shift of the endpoints in the opposite direction relative to optimal RW voltage by $(0.123 \pm 0.026)\,\mathrm{eV}$. For the calculation of the shift, the difference between the mean value of all endpoints during KNM5b before and after the change

---

[3] Endpoints were provided by Simon Tirolf.

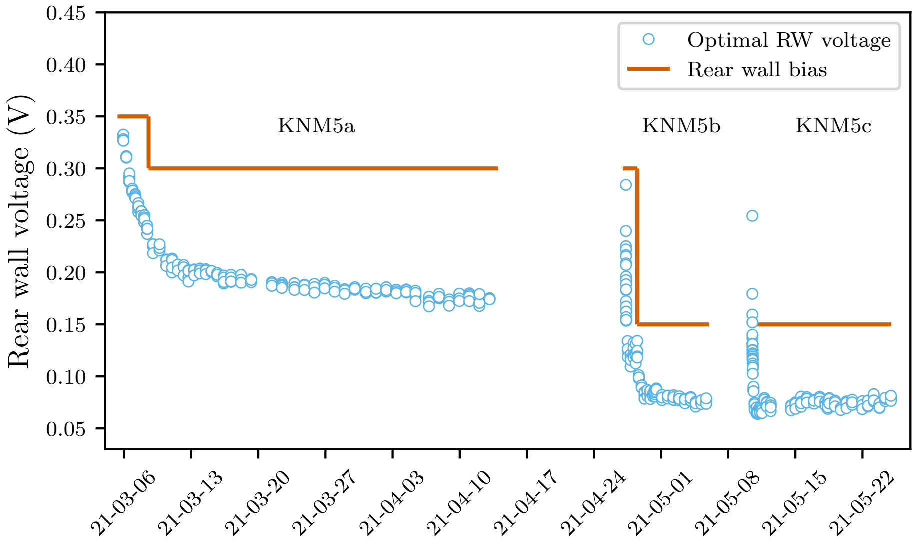

Figure 5.17.: The variation of optimal RW voltage after the start of beta scans during KNM5. The burn-in phases at the beginning and after the two interruptions show a faster saturation time, moreover, an equilibrium state of optimal RW voltage seems to have been reached in KNM5c because a less significant drift was observed. In KNM5b after the burn-in phase, the optimal RW voltage has reached a lower value than in the previous phase at RW bias of 300 mV. Possibly these are adsorption effects of the ions; the ions could diffuse into deeper layers and change the work function of the RW. The figure does not show all IU-scans of KNM5 as used in the neutrino mass measurements.

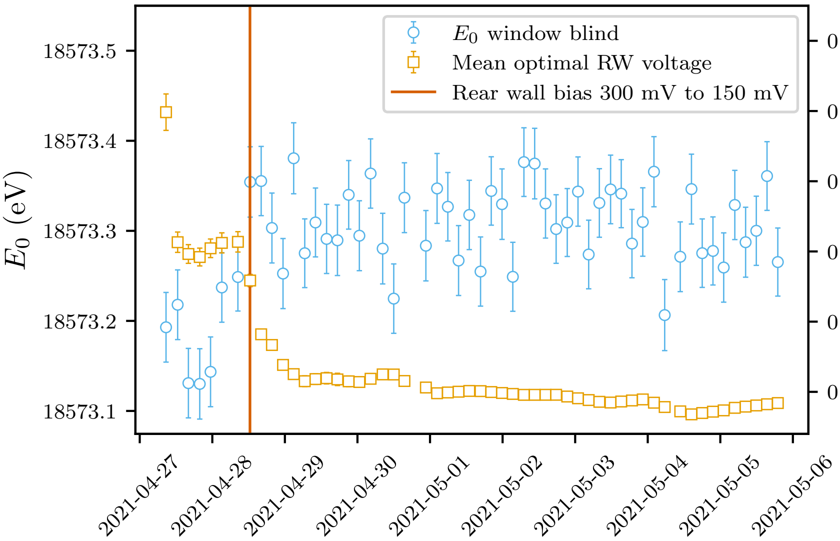

Figure 5.18.: Linearly interpolated optimal RW voltage compared with window blind endpoints during KNM5b. Before and after the change of the RW bias by 150 mV, there is a shift in the endpoints of (0.123 ± 0.026) eV.

of the RW bias was used.

With the combination of equations 4.11 and 5.6 it can be calculated how the change in RW bias affects the beam tube work function:

$$\Phi_{\mathrm{BT}} - A_{\mathrm{off}} = -E_0 + c \cdot (eU_{\mathrm{RW}} - \Delta\Phi_{\mathrm{RW-BT}}) \ . \tag{5.7}$$

The coupling required for the determination is obtained with equation [Kle+ep]:

$$c(r) = c_0 \left(1 - \left(\frac{r}{r_{\mathrm{max}}}\right)^x\right) \ , \tag{5.8}$$

with the normalization constant c_0 mostly depending on the coupling regime, x as the exponent of the model, depending also on source conditions and r_{max} is the maximum radius of the beam tube. The fit model is based on the electric potential of a homogeneously distributed charge in a cylinder geometry. For the coupling, the fitted values $c_0 = 1.009 \pm 0.006$, $r_{\mathrm{max}} = (45.755 \pm 0.532)$ mm and $x = 6.717 \pm 0.453$ were taken from PRO-KATRIN measurements performed at 75 % CD and 80 K in a good coupling regime during KNM3.[4] The endpoint is not considered radially dependent in this analysis. Accordingly, the weighted average of the coupling is calculated ring-wise using the preliminary golden pixels from KNM5. Two phases are considered depending on the the RW bias, 350 mV and 150 mV.

Figure 5.19 shows the results for the difference between the work function of the beam tube and the effective offset after substituting the available values into equation 5.7, taking into account the propagation of uncertainty. One of the determined drifts is insignificant, one is slightly significant (1 σ) and the shift of (0.085 ± 0.032) eV is almost significant at 3 σ.

In addition, the drift of the RW work function was investigated, using equations 5.7 and 4.9:

$$\Phi_{\mathrm{RW}} - A_{\mathrm{off}} = \Phi_{\mathrm{BT}} - A_{\mathrm{off}} + \Delta\Phi_{\mathrm{RW-BT}} \ . \tag{5.9}$$

---

[4] The coupling from PRO-KATRIN measurements was taken from: `https://ikp-katrin-wiki.ikp.kit.edu/katrin/index.php/Radial_plasma_potential_from_coupling_strength_(PRO-KATRIN)`.

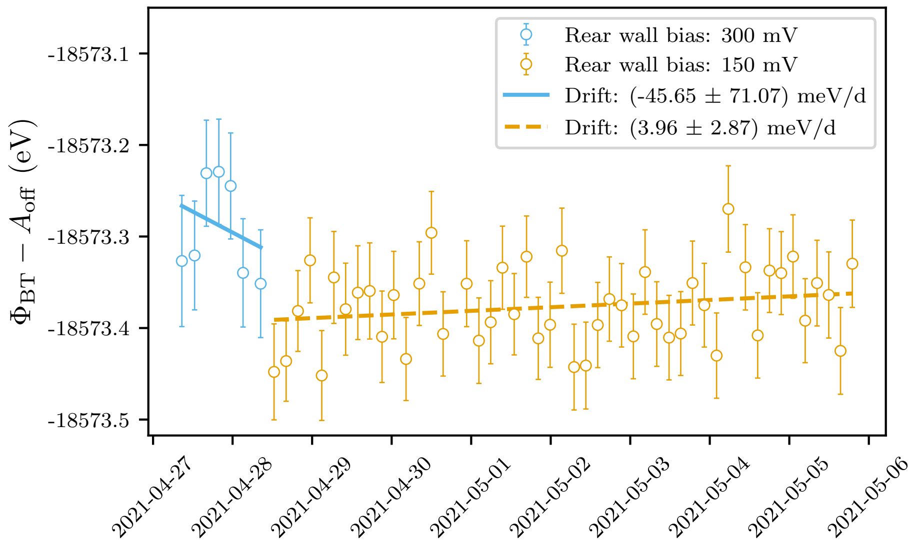

Figure 5.19.: Difference between the beam tube work function and the effective offset. The observed shift between the RW bias change is (0.085 ± 0.032) eV.

The result for the difference between the RW work function and the effective offset can be seen in figure 5.20. There is a significant shift of (0.131 ± 0.031) eV between the change of the RW bias. The larger shift indicates that it is the RW work function that changes between the change in RW bias rather than the beam tube work function. Unfortunately, due to the matching uncertainties of these two shifts, it is not possible to say clearly from which boundary the work function dominates.
Krypton measurements are performed during the writing process of this thesis. With a more accurate measurement it will be possible to find out whether the RW or the beam tube work function is causing the subsequent long-term drift.

5.3.5. Comparison between optimal rear wall voltage with voltage at total DPS dipole current peak

During the IU-scans, a characteristic peak in the total DPS current is observed. It is assumed that the peak is caused by neutralization processes in the source. The 'peak' actually corresponds to a decrease of the measured ions in the DPS dipole electrodes. Since the total DPS current peak may be suitable for determining the optimal RW voltage, it is of interest to investigate whether the peak also exhibits the same drift behavior as the optimal RW voltage determined by the Zero WGTS current method. The possible physical origin of the peak is introduced in section 5.1.3.

In the absence of the exact physical model the peak is approximated with a Gaussian distribution:

$$f(x) = A \cdot \exp\left(-\frac{(x-\mu)^2}{2\sigma^2}\right) + b\ . \tag{5.10}$$

The position of the peak can then be determined from the free fit parameter μ. In addition to the statistical uncertainty from the fit, a systematic uncertainty of ± 5 mV of the peak position was assumed, because spikes sometimes appear next to the peak which additionally distort the fitted peak position, but cannot be excluded as outliers because the physical origin is not clear.

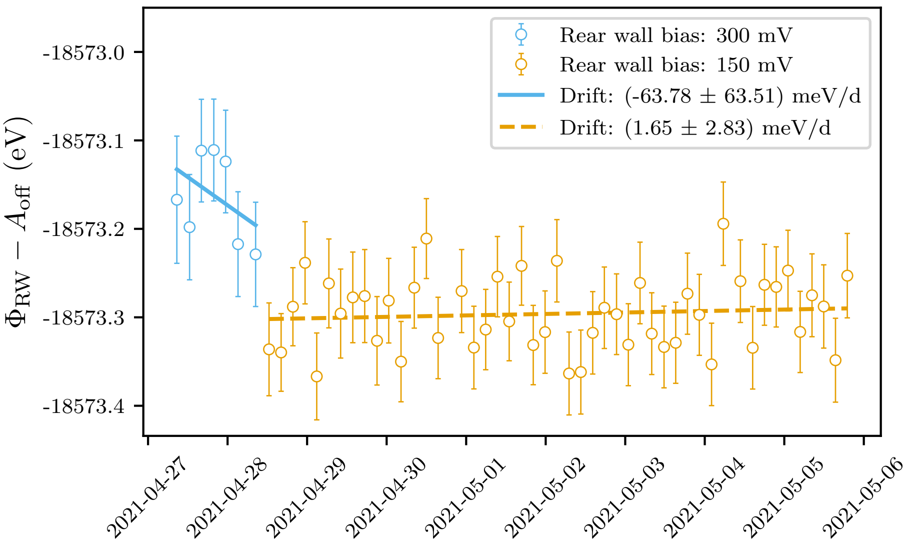

Figure 5.20.: Difference between the RW work function and the effective offset. The observed shift between the RW bias change is (0.131 ± 0.031) eV. The larger shift compared to (0.085 ± 0.032) eV indicates that it is the RW work function that changes between the change in RW bias rather than the beam tube work function.

Figure 5.21 shows the results for KNM4. In the burn-in phase, both curves show a similar decreasing behavior and the correlation coefficient is $r = 0.78$ (see appendix B.2). However, when looking at the subsequent long-term drift, it can be seen that the drift slopes differ significantly from each other. Similar observation was also noted in KNM3a (see appendix B.3) where there was a significant drift in the Zero WGTS current values of $(0.54 \pm 0.08)\,\mathrm{mV\,d^{-1}}$ but an opposite, less significant drift in the total DPS current peak of $(-0.19 \pm 0.07)\,\mathrm{mV\,d^{-1}}$.

However, in KNM3b after changing the column density from 40 % to 75 %, the Zero WGTS current values showed a high significant drift which was also evident in the total DPS current peak (see appendix B.4). A similar good correlation as during the KNM4 burn-in phase of $r = 0.89$ was observed, although the slope in the the total DPS current peak is slightly larger by a factor of 1.33 ± 0.26. It could be that KNM3b can rather still be counted as part of the burn-in phase.

It can be said that the measured drift cannot be reliably monitored using the DPS current peak method. Because it is assumed that the total DPS current peak arises from neutralization processes in the source, it may consider work function differences of the RW and the beam tube but additionally also drifts in the DPS. This could lead to the different behavior during the long-term drift phase compared to the Zero WGTS current method. However, the inconsistencies cannot be definitively resolved and it remains unclear what happens during the long-term drift phase. It cannot also be excluded that the physical origin of work function changes in the DPS are the same as for the work function changes for boundaries of the plasma.

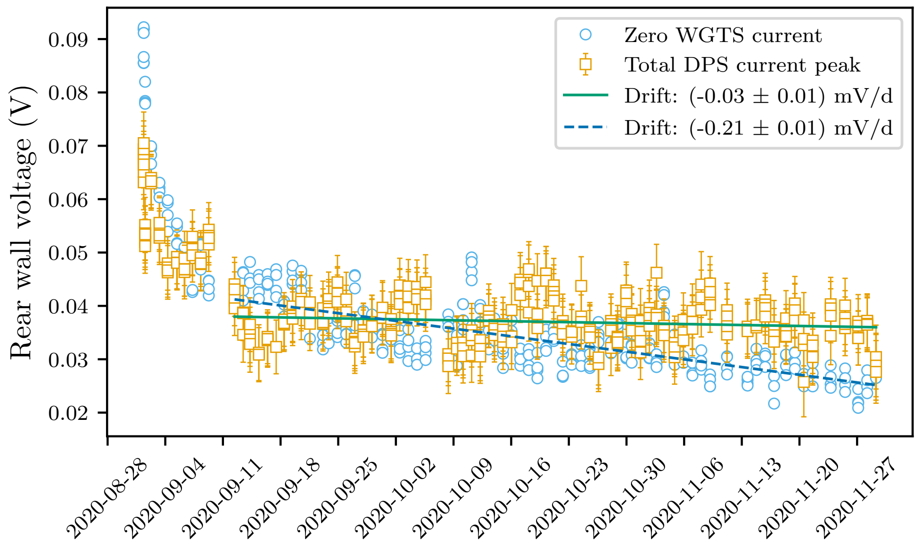

Figure 5.21.: Monitoring of the total DPS current peak and the optimal RW voltage with Zero WGTS current method during KNM4. While a similar drop in optimal RW voltages is observed in the burn-in phase, the two slopes differ significantly in the later course. One possible explanation could be that the total DPS current peak is additionally affected by work function differences in the DPS, which have no influence on the boundaries of the plasma. However, work function differences of the boundaries are captured by the Zero WGTS current.

5.4. Summary and conclusions

Measuring the optimal RW voltage using the currents from the source is a more precise and faster measurement method compared to the detector-based method with PRO-KATRIN. The optimal RW voltage from continuous IU-scans is comparable to the optimal RW voltage determined with discrete IU-scans during krypton measurements in KNM3 and also comparable to the krypton detector-based method. (section 5.1.2)

The uncertainty on a single data point of the optimal RW voltage from a single sweep is dominated by the noise of the currents. The estimated statistical uncertainty of the optimal RW voltage is $\sigma = 3.68\,\mathrm{mV}$ during KNM4 and $\sigma = 3.52\,\mathrm{mV}$ during KNM5c. (section 5.2.2)

No strong correlation with the column density after the start of beta scans in KNM4 was found. The drift during the burn-in phase in KNM4 has shown a strong correlation of 0.93 with the tritium purity, indicating that adsorbed impurities such as hydrocarbons on the RW or on the beam tube are causing the change of work functions. The subsequent rather low correlation of $r = 0.41$ of the tritium purity during the long-term drift phase does not allow a clear conclusion. (section 5.2.3)

It was demonstrated that the choice of RW bias voltage has an effect on the optimal RW voltage drift and its equilibrium value, which was shown in the test measurements at the end of KNM3 and during KNM5b. The correlation was also clearly observed during the krypton measurements at the end of KNM5, where the optimal RW voltage lagged behind the changed RW bias. Furthermore, the choice of the IU-scan range also has an influence on the slope of the drift, at least this could be shown in test measurements with a high voltage scan range of $(-3\ldots+6)\,\mathrm{V}$. (section 5.3.2) According to the endpoint analysis, it suggests that between the change in RW bias during KNM5b, the RW work function changed rather than the work function of the beam tube. (section 5.3.4)

Additionally, it was shown that the observation of the optimal RW voltage drift with the total DPS current peak differs significantly from the observations with the Zero WGTS current method, thus this method is unsuitable to observe the drift. (section 5.3.5)

A burn-in phase of the optimal RW voltage after injection of tritium was observed in several measurement campaigns, the physical origin of which probably points to the adsorption of ions at the RW, but it is not possible to distinguish whether it is a global change in work function or charging of insulating patches. (section 5.3.3) It is not possible to conclude whether the burn-in effect and the effect after the change of the RW voltage have the same underlining physical origin.

Chapter 6.

Neutral gas simulations between the WGTS and rear wall

In order to understand the plasma in the source, simulations of electric and magnetic fields are necessary. For this purpose, it is essential to know the particle density and the velocities of the neutral gas, which are used as input parameters in plasma simulations. So far, only gas simulations between the WGTS and CPS have been performed [Röt19]. The geometry of the experiment is not perfectly symmetrical between the rear and front direction. Thus simulations were performed with MolFlow+ between the center of the WGTS and RW in the context of this thesis. The RW chamber geometry was implemented specifically for the neutral gas simulations in MolFlow+.

This chapter first describes the basics of the MolFlow+ simulation package. Then the preparations for the simulation are presented. After that, the simulation results are shown and discussed, which can be incorporated into the KARL simulation package in near future. Finally, with the determined longitudinal velocity and the particle density, the transversal ion motion was estimated.

6.1. Molecular gas flow simulations with MolFlow+

MolFlow+ is a Monte Carlo simulation software for Windows, which was developed to calculate pressure profiles and conductances of ultra high vacuum systems [Ady16]. The random numbers are generated using the Mersenne-Twister algorithm [MN98].

Under ultra high vacuum conditions, the mean free path of molecules is much larger than the extent of the geometry. The dynamic behaviour of the gas can be described with the Knudsen number:

$$Kn = \frac{\lambda}{L} \ , \tag{6.1}$$

with the mean free path λ and L as characteristic dimension of the vacuum system. In general, a distinction is made between three gas flow regimes [Hän06]:

- $Kn \gg 1$: At these conditions, the free *molecular flow regime* is present, where collisions between molecules are negligible.

- $Kn \ll 1$: In the *continuum flow regime*, the gas is described with continuum mechanics.

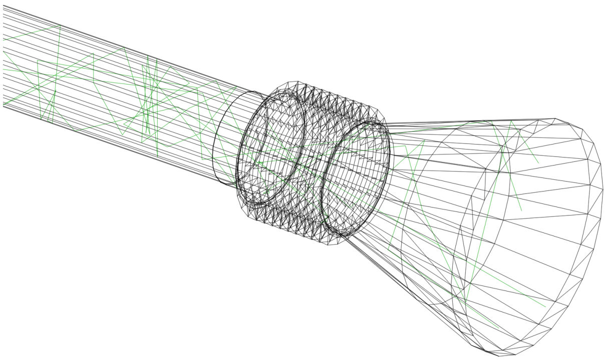

Figure 6.1.: Geometry and trajectories of the simulated particles in MolFlow+. The green straight lines illustrate the simulated paths of the generated particles between surfaces of two facets.

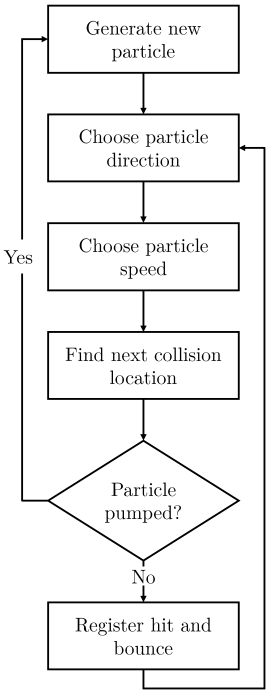

Figure 6.2.: Flow chart of the MolFlow+ algorithm. Figure inspired by [Ady16].

- $Kn \approx 1$: In the *transition regime*, the inter-molecular collisions cannot be neglected and the mean free path is comparable to characteristic dimension of the vacuum system.

In MolFlow+ for the Knudsen number it must hold $Kn \gg 1$ [Jou18] and the generated particles therefore only interact with the geometry; no interactions between the particles are considered.

The geometry of the vacuum system is partitioned into polygons, which are called facets [Ady16]. It is possible to import geometries created with CAD programs, which support STL file format. Otherwise, the user can also create simple geometries directly in MolFlow+.

Each facet can be assigned different physical properties such as temperature, outgassing rate or opacity. The outgassing rate can also be set for each facet, defining the points at which the test particles are inserted into the system. The value of the outgassing rate of a facet is used as a weight for the random selection of the starting facet of a new particle trace. The opacity $\in [0, 1]$ can be used to define whether the facet is transparent for the vacuum system. Facets with opacity 0 can be used as additional counters for measuring physical quantities. If the opacity is set to value 1, the facet is considered as a physical wall of the vacuum system.

In addition, the direction and the rebound behaviour of the generated particle can be set for a specific facet. It is assumed that the direction of the rebound particle is independent of the incoming direction. For this thesis Knudsen's cosine law is used and the direction of the rebound particle is described by:

$$\mathrm{d}s = \pi \cdot \mathrm{d}\omega \cdot \cos(\theta) \ , \tag{6.2}$$

where ds is the probability that a molecule leaves a facet in angle dω and θ is the angle between the normal surface vector of a facet and the direction of a particle [Knu67].

After the velocity and direction of the particle have been generated, a ray-tracing algorithm is used to find the next collision point. Figure 6.1 shows the straight trajectories of particles simulated in MolFlow+. In the following the particle has two possibilities: either the particle is pumped off at a facet or it bounces off which depends on the so-called sticking coefficient $\alpha \in [0,1]$. The coefficient indicates the probability that the particle will be pumped out. If this is the case, the present tracking ends and the next particle is generated, starting at a randomly selected facet with a non-zero outgassing rate. The basic steps of the algorithm are summarized in figure 6.2.

The sticking coefficient, which represents the pumps, can be converted into pumping speed through:

$$S = \frac{1}{4} \cdot v_{\text{avg}} \cdot A \cdot \alpha \ , \tag{6.3}$$

where A is the surface area of the pumping facet and $v_{\text{avg}} = \sqrt{\frac{8RT}{\pi M}}$ is the average molecular speed, which is automatically calculated with corresponding facet temperature T. MolFlow+ simulates only particles of the same gas species with a molar mass M, which can be specified before the simulation starts [AK+14]. The value of the mass has no direct influence on the particle tracking, but on the particle velocity.

Every interaction with a facet is registered by a hit counter. After a rebound in which momentum and energy transfer takes place, the so-called accommodation coefficient $A_{\text{acc}} \in [0,1]$ can be used to define which fraction of the kinetic energy before the interaction is taken over by the rebounded particle. The new kinetic energy is calculated with the equation (6.4)

$$v_{\text{new}}^2 = v_{\text{old}}^2 + A_{\text{acc}}(v_{\text{wall}}^2 - v_{\text{old}}^2) \ , \tag{6.4}$$

where v_{wall} is the new generated velocity according to the Maxwell–Boltzmann distribution, which takes into account the corresponding facet temperature. The accommodation coefficient is set to 1 by default, therefore the particle does not take over any kinetic energy it had before the hit.

The ray-tracing algorithm checks each facet to determine the shortest collision point, thus the simulations become slower with the number of facets. For large geometry models with many facets it is possible to shorten the simulation time by dividing the geometry into segments.[1]

For performance reasons the real physical number of particles in the system is represented with a smaller set of generated virtual test particles. A conversion factor can then be used to infer the actual physical quantities from a smaller set of test particles. [Ady16]

6.2. Geometry of the rear wall chamber

In the scope of this thesis, the existing MolFlow+ geometry model of the KATRIN experiment was extended with the RW chamber. For this purpose, an existing detailed CAD model of the rear section was used. The RW chamber was then isolated from the model, which had to be further simplified in additional steps.

In order to reduce the number of facets which leads to an improvement in statistics for the same simulation time, fasteners such as bolts, nuts and washers were removed. Since only the inner surfaces of the vacuum chamber are used, the outer surfaces on the atmospheric side of the

---

[1] Further details about segmentation can be found in the MolFlow+ use guide: `https://molflow.web.cern.ch/sites/molflow.web.cern.ch/files/molflow_user_guide.pdf`.

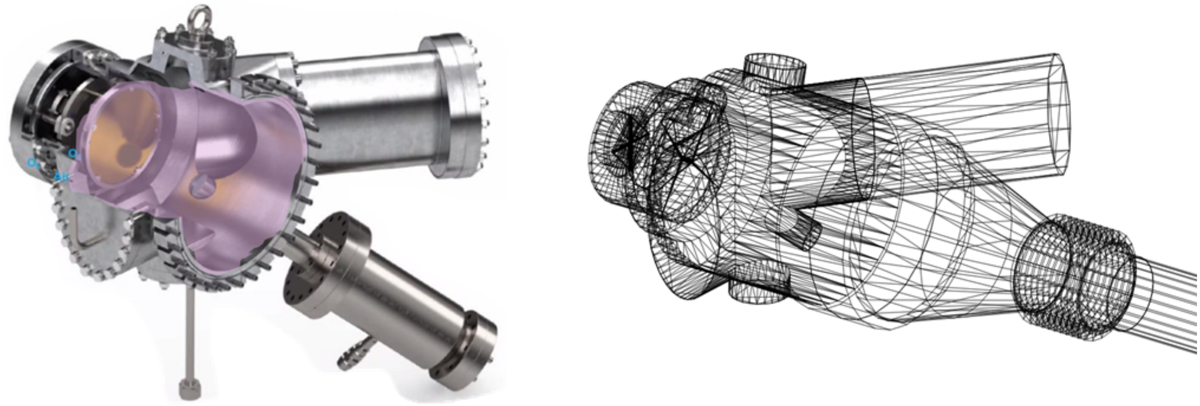

Figure 6.3.: Comparison between the CAD model (left) and the derived mesh (right), which is used in MolFlow+.

chamber walls were removed from the model. Figure 6.3 shows the transition from the detailed CAD model to the simplified mesh model, which was afterwards combined with the existing geometry in MolFlow+. After the combination a leak test was performed in test simulations. The test simulations are necessary because after the conversion from the CAD model to the mesh model for MolFlow+, conversion errors can occur. This results in misaligned facets with large leaks. Thus, misaligned facets were identified, deleted and new facets were created manually.

6.3. Simulation setup

In this section the simulation setup for the evaluation of the three gas parameters are introduced.

- For the measurement of the particle density in longitudinal direction z, xz-plane and yz-plane measurement facets were used (see fig. 6.4).[2] With this arrangement, the particle density can be investigated radially and longitudinally.[3] The setting of the measurement facets was set to two-sided so that the hits of the particles are recorded from all directions. Using square cells as local division of the measurement facets, a resolution of 1 cm was chosen.

- In order to measure the velocity distributions of the individual components, a coordinate cross arrangement of the measurement facets is created, which only register the orthogonal components of the velocity (see. fig. 6.4). Six one-sided planes are used for this purpose, which capture both directions of v_x, v_y and v_z.

- To simulate the absolute velocity, the same cross plane arrangement was used as for the measurement of the velocity components, except that the measuring surfaces were set to two-sided and the speed distribution instead of orthogonal velocity was selected in the profile setting. In this case, the magnitude of the velocity of all particles coming from all sides is measured which means that only three planes are necessary.

---

[2] The areas of the measurement facets were chosen larger than the geometry for simplicity. This does not affect the simulation results.

[3] The opacity of the measurement facets was set to 0 so that the surfaces have no influence on the simulation.

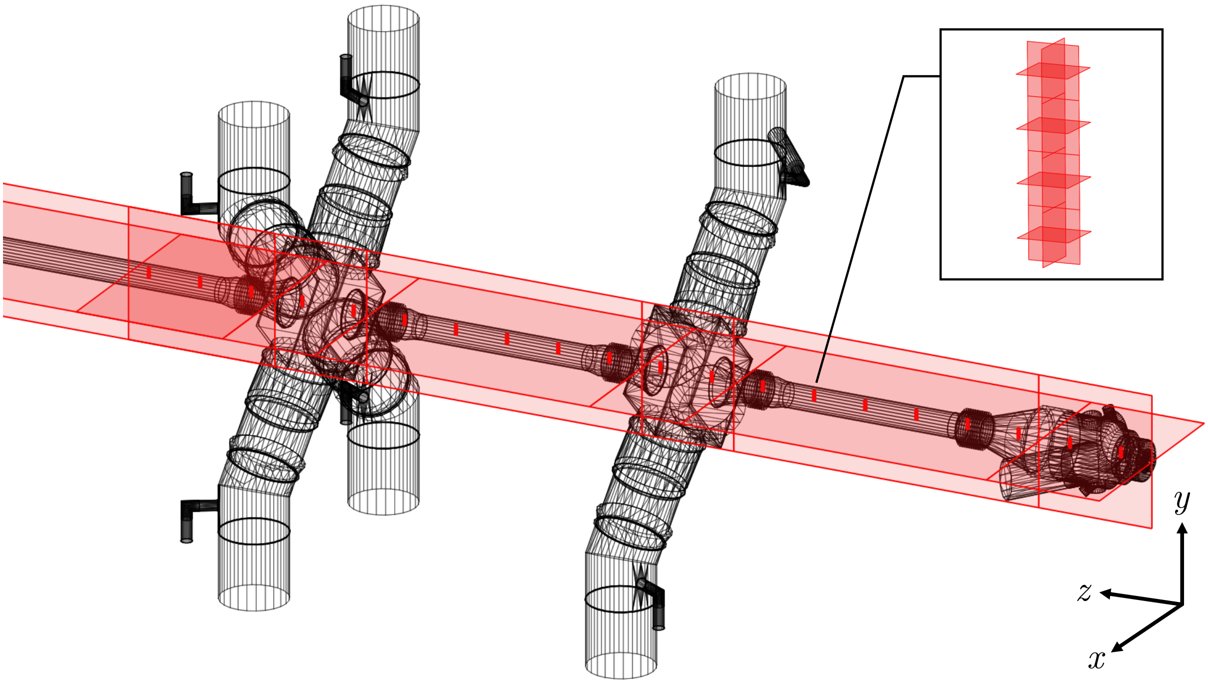

Figure 6.4.: Simulation setup after the combination with the RW chamber. Measuring facets for particle density in xz-plane and yz-plane. Drawn along the center of the beam tube (BT) is the plane cross arrangement for the measurement of the absolute velocity and the velocity components in radial and in z-direction.

The area of the coordinate cross arrangement was set to 1 cm^2 and the spacing was chosen so that the first arrangement starts immediately at the surface of the RW and is then spaced longitudinally at 20 cm intervals. In addition, further plane crosses were positioned in the radial direction with a resolution of 0.5 cm.

Two different temperature settings of the source were used in the simulation. Fist, to compare the results with previous simulations carried out at beam tube wall temperature $T = 30\,\mathrm{K}$ and second, to have results for the current standard setting at $T = 80\,\mathrm{K}$.

The effective pumping speed in the RW chamber is dominated by the small conductance through the hole, which was optimized for the transmission of the e-gun beam [Ake+21b]. Therefore the pumps behind the RW chamber are negligible. The value for the sticking coefficient was estimated at $\alpha = 0.1$.

For the 14 TMPs of the WGTS beam tube at DPS1-F/R the corresponding sticking coefficient $\alpha = 0.25$ with a systematic uncertainty of 20 % for mass $\mathrm{m} = 6\,\mathrm{g\,mol^{-1}}$ was taken into account [Mar+21; Mal07]. Facets that are not pumps have been assigned a sticking coefficient of 0. Therefore, no distinction is made between the type of material and the surface texture, and the test particles are always reflected.

The facets located in the center of the WGTS, which represent the injection chamber, are defined with an outgassing rate of $1\,\mathrm{mbar\,l\,s^{-1}}$ and the temperature of the facets corresponds to the temperature of the beam tube wall.

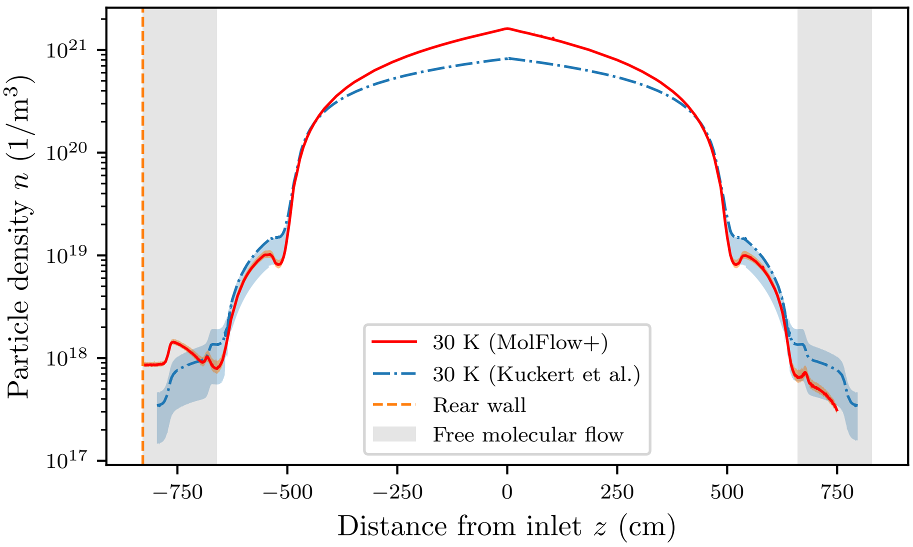

Figure 6.5.: Comparison of simulated particle density at $T = 30\,\mathrm{K}$. Shown are the simulation results of particle density with MolFlow+ and COMSOL at $T = 30\,\mathrm{K}$ normalized at $z_{\mathrm{Norm}} = -440.61\,\mathrm{cm}$. The gray areas indicate where the condition of the simulations with MolFlow+ is fulfilled. The small red uncertainty band comes from the uncertainty on the sticking coefficient. The COMSOL simulation for the front part is mirrored at the center of the WGTS and taken from [Kuc+18].

6.4. Particle density distribution of T_2

No significant radial differences of the particle density in the yz-plane and xz-plane could be found when analyzing the results for $T = 30\,\mathrm{K}$ and $T = 80\,\mathrm{K}$. Therefore, only the averaged results of the xz-plane are considered in the following. Due to the relatively small number of hits on the measurement facet N_{hits} compared to the total number of desorbed particles in a simulation run, Poisson distribution is a reasonable assumption for the calculation of the uncertainty of particle density Δn, which can be determined as follows:

$$\Delta n = \frac{n}{\sqrt{N_{\mathrm{hits}}}} \,, \tag{6.5}$$

the derivation of the equation can be found in appendix A.

Figure 6.5 shows the simulation results for $T = 30\,\mathrm{K}$ in comparison with COMSOL Multiphysics® simulation results of L. Kuckert et. al which was performed from the WGTS center in the spectrometer direction [Kuc+18]. For comparison, the values are mirrored in the direction of the RW. The MolFlow+ simulations were run several times to account for the uncertainty in the sticking coefficient. The upper limit of the uncertainty band represents the simulation performed with $\alpha = 0.2$ and the lower limit with $\alpha = 0.3$. The relative uncertainties on the particle density mean values are predominantly smaller than 0.6 % and are thus smaller than the line width of the curve.

To compare the curves, the values of MolFlow+ simulation were normalized at the position $z_{\mathrm{Norm}} = -440.61\,\mathrm{cm}$ with the value $n(z_{\mathrm{Norm}}) = 1.90 \times 10^{20}\,\mathrm{m}^{-3}$ from curve by L. Kuckert et. al. The comparison is necessary because COMSOL simulations cover all gas flow regimes and MolFlow+ only the molecular flow regime in the last beam tube element and in the rear chamber.

The particle density simulated with MolFlow+ from the normalization point towards the RW lies predominantly in the blue uncertainty band of the particle density simulated with COMSOL. In the central region, the deviation is large, due to the continuum flow regime where the MolFlow+ can only make very inaccurate statements about the particle density.

Also in the molecular flow regime in the direction of the RW a deviation of the two data sets can be observed. Figure 6.6 shows a zoomed in plot of two different normalization points. The red uncertainty band here represents the uncertainty of the differently chosen normalization points, which in the left plot is predominantly the uncertainty of the sticking coefficient. Only in the right plot the uncertainty on the new normalization point at $z_{\mathrm{Norm}} = -540\,\mathrm{cm}$ dominates due to larger range of uncertainty of the reference curve.

The simulated particle density between the RW and the WGTS is in good agreement with previous simulation and the emerging deviation of the curve comes from the weak pumping speed at the end of the RW chamber. This leads to an increase in particle density just before the neutral gas particles enter the RW chamber. However, this increase cannot be observed in the simulation at the transition from the WGTS to the DPS section which can be explained by the higher pumping speeds in the subsequent sections.

Due to unavailability of reference simulations at $T = 80\,\mathrm{K}$, the $T = 30\,\mathrm{K}$ curve was re-scaled (see fig. 6.7). For this, the ideal gas law was used and the existing inlet pressure of $p_{\mathrm{in}} = 0.7\,\mathrm{Pa}$ for the KNM4 phase with a column density of 75 %. The reference curve was simulated at an inlet pressure of $p_{\mathrm{in}} = 0.337\,\mathrm{Pa}$ and at 100 % CD.

Table 6.1 shows the simulation results for the particle density right in front of the RW for both beam tube temperatures $T = 30\,\mathrm{K}$ and $T = 80\,\mathrm{K}$. Even with the worst-case normalization at $z_{\mathrm{Norm}} = -540\,\mathrm{cm}$, the uncertainty band on the particle density with MolFlow+ is smaller in the molecular flow regime compared to the uncertainty band of COMSOL simulations.

6.5. Velocity distribution of T_2

Two cases are distinguished in the following: the first one is the one-dimensional distribution of the velocity components, the second one is the absolute velocity distribution. From the component-wise distribution v_z, the drift velocity $v_{z,\mathrm{drift}}$ is then extracted for a simplified description with few parameters as input for KARL. The absolute velocity distribution is used to calculate the gas temperature.

For the one-dimensional distribution, the one-dimensional Maxwell–Boltzmann distribution is

Table 6.1.: Particle density at RW. The significantly larger uncertainty for $z_{\mathrm{Norm}} = -540\,\mathrm{cm}$ is due to the choice of the normalization point, where the reference curve already has a large uncertainty.

Temperature (K)	Particle density (m^{-3})	
	$z_{\mathrm{Norm}} = -440.61\,\mathrm{cm}$	$z_{\mathrm{Norm}} = -540\,\mathrm{cm}$
30	$8.63^{+0.61}_{-0.30} \times 10^{17}$	$9.13^{+2.61}_{-2.09} \times 10^{17}$
80	$1.09^{+0.09}_{-0.05} \times 10^{18}$	$1.14^{+0.34}_{-0.27} \times 10^{18}$

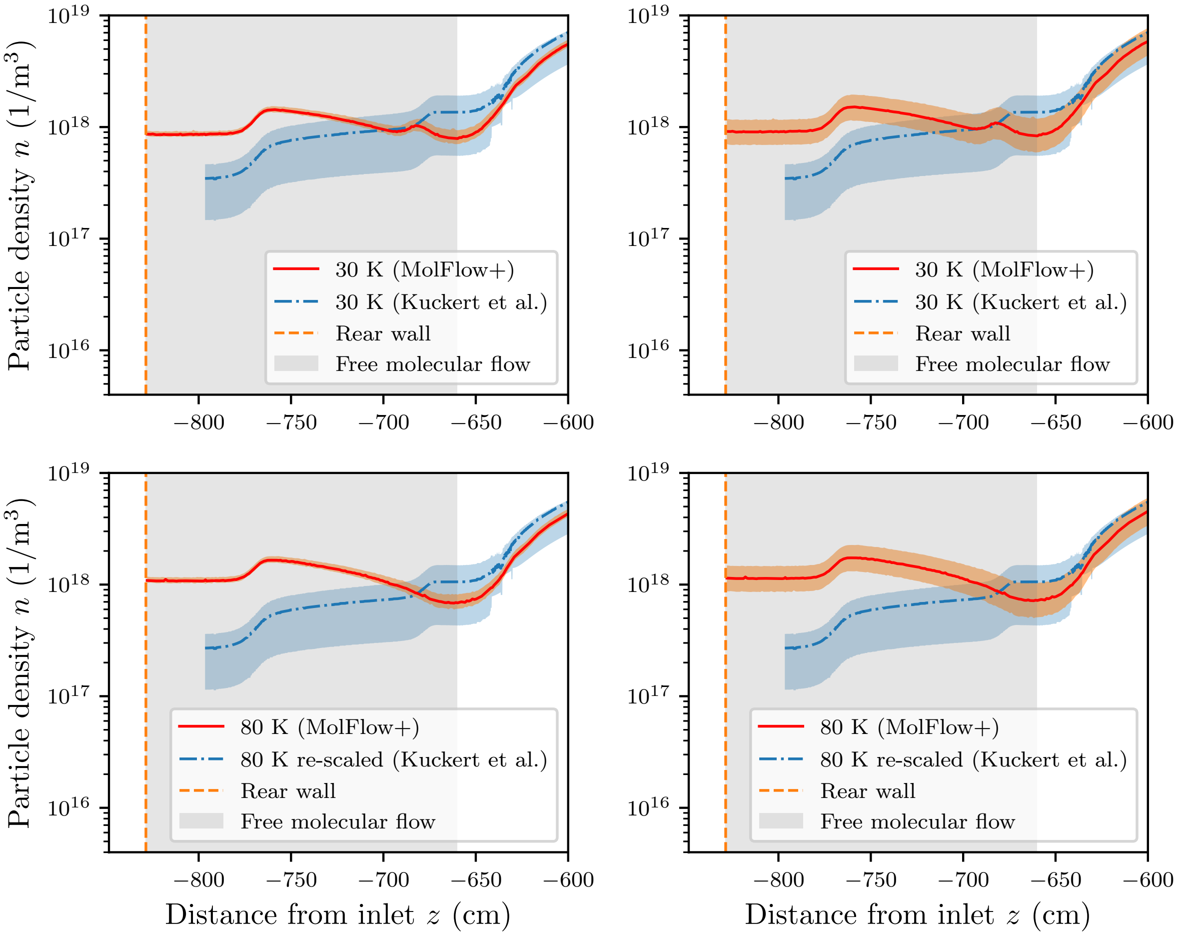

Figure 6.6.: Comparison of uncertainties at different normalization points for $T = 30\,\mathrm{K}$ (top) and $T = 80\,\mathrm{K}$ (bottom). The deviation due to the effective pumping speed dominated by the small conductance compared to the reference curve of the front part in blue which is mirrored at the center of WGTS can be seen. Depending on where the normalization point is chosen ($z_{\mathrm{Norm}} = -540\,\mathrm{cm}$ on the right and $z_{\mathrm{Norm}} = -440.61\,\mathrm{cm}$ on left side), different uncertainty bands arise. Even with the worst-case normalization at $z_{\mathrm{Norm}} = -540\,\mathrm{cm}$, the uncertainty band on the particle density with MolFlow+ is smaller in the molecular flow regime compared to the uncertainty band of COMSOL simulations.

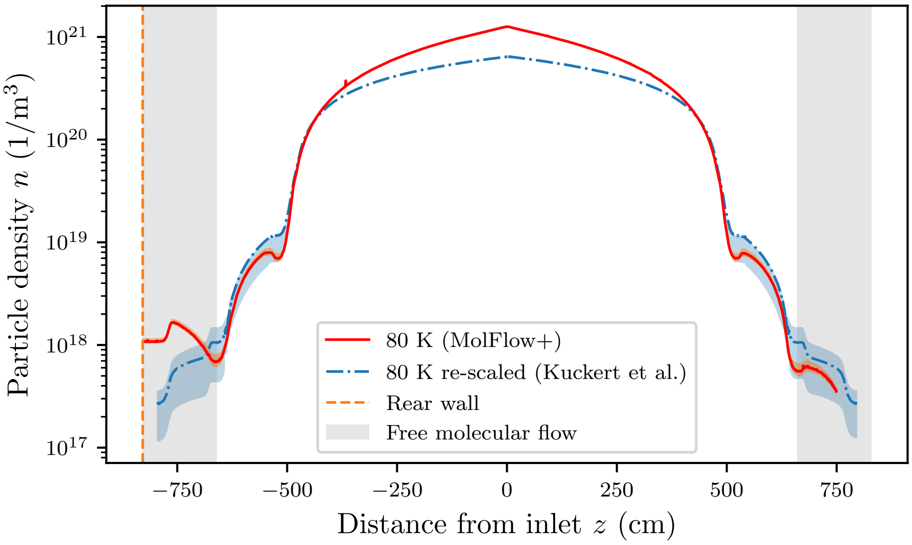

Figure 6.7.: Comparison of simulated particle density at $T = 80\,\mathrm{K}$. Shown are the simulation results of particle density with MolFlow+ and the re-scaled results from COMSOL at $T = 80\,\mathrm{K}$ normalized at $z_{\mathrm{Norm}} = -440.61\,\mathrm{cm}$. The gray areas indicate where the condition of the simulations with MolFlow+ is fulfilled. The small red uncertainty band comes from the uncertainty on the sticking coefficient. The COMSOL simulation for the front part is mirrored at the center of the WGTS and taken from [Kuc+18].

assumed as a fit model:

$$f_{1\mathrm{D}}(v_i) = \left(\frac{m}{2\pi k_{\mathrm{B}} T}\right)^{1/2} \exp\left(-\frac{m\left(v_i - v_{i,\mathrm{drift}}\right)^2}{2k_{\mathrm{B}}T}\right) \tag{6.6}$$

$$f_{1\mathrm{D}}(v_i) = A \exp\left(-\frac{\left(v_i - v_{i,\mathrm{drift}}\right)^2}{2a^2}\right) , \tag{6.7}$$

with the fit parameters $A = (m/(2\pi k_{\mathrm{B}} T))^{1/2}$ and $a^2 = k_{\mathrm{B}}T/m$. The free fit parameter $v_{i,\mathrm{drift}}$ is interpreted in this case as the drift velocity in the corresponding direction. This serves as a simplified assumption for the current version of KARL and allows a description of the plasma with few parameters. Using the three-dimensional Maxwell–Boltzmann distribution equation:

$$f_{3\mathrm{D}}(v) = \left(\frac{m}{2\pi k_{\mathrm{B}} T}\right)^{3/2} 4\pi v^2 \exp\left(-\frac{mv^2}{2k_{\mathrm{B}}T}\right) \tag{6.8}$$

$$f_{3\mathrm{D}}(v) = \sqrt{\frac{2}{\pi}}\frac{v^2}{a^3} \exp\left(-\frac{v^2}{2a^2}\right) , \tag{6.9}$$

the obtained simulation data of the absolute velocity distributions are fitted. Subsequently, the temperature of the gas can be calculated from the free fit parameter $a^2 = k_{\mathrm{B}}T/m$.

6.5.1. Longitudinal drift velocity $v_{z,\mathrm{drift}}$

In this section the drift velocity is calculated, which is used for a simplified description with few parameters for the plasma simulation software KARL.

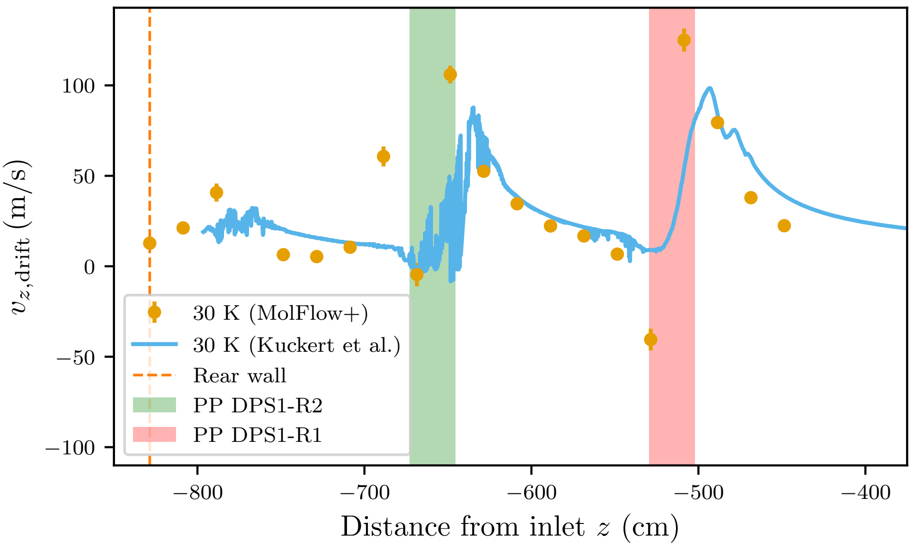

Figure 6.8.: Comparison of drift velocities at $T = 30\,\mathrm{K}$ between MolFlow+ and COMSOL. The drift velocities simulated with MolFlow+ predominantly agree with the mirrored COMSOL simulation results. In the pumping regions there are significant deviations from the model assumption, so that the values in these regions are not reliable.

Figure 6.8 shows the comparison of the simulation results with the mirrored drift velocity from COMSOL simulations. The drift velocities agree relatively well, except in the domains where the TMPs are located. At these locations, the drift is partially negative and the neutral gas particles would move in the direction opposite to the RW. One reason is that the velocities in these domains can no longer be well described by a Maxwell–Boltzmann distribution. In the areas of the TMPs there are strong temperature gradients, because the particles have not yet had the opportunity to interact with the walls near the measurement facet to obtain the corresponding low temperatures. Thus, the probability is high that particles are still detected that originate from the room temperature regime and either have not been pumped away or have simply been reflected by the surrounding walls near the pump facet. As an example, the figure 6.9 illustrates first, the comparison of distributions simulated in the region where the transitions between the different temperature domains occur and where a gradient has been set in the facets, and second, in the range of predominantly constant facet temperature regimes. In the region of constant facet temperature, the model assumptions agree well. In the temperature gradient regions of the facets, the simulated data have more contributions towards higher velocities and no longer match the fit model.

In figure 6.10 the drift velocities for $T = 80\,\mathrm{K}$ and for $T = 30\,\mathrm{K}$ are compared. The particles of the $T = 80\,\mathrm{K}$ simulation before the first and second pump ports are faster than the particles of the $T = 30\,\mathrm{K}$ simulation. After the second pump, the characteristic is reversed. A possible reason could be that after the second pump port most of the particles of the $T = 80\,\mathrm{K}$ simulation with high velocity contributions were pumped away. For particles coming from the $T = 30\,\mathrm{K}$ center of WGTS, which have correspondingly smaller average velocities, the pumping speed is weaker according to equation 6.3, so that possibly more particles with higher drift velocities have reached the region after the second pump port.

In addition, a negative drift velocity in the last beam tube piece was observed. Because only

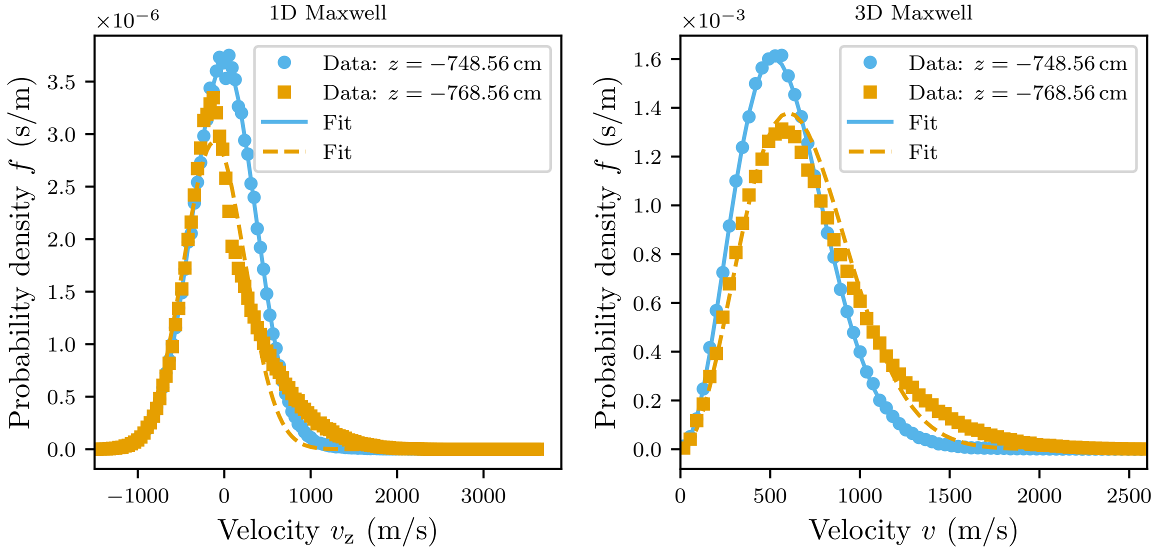

Figure 6.9.: Deviation from the 1D and 3D Maxwell–Boltzmann distribution model assumption. The figures on the left and right show the deviation from the corresponding 1D and 3D Maxwell–Boltzmann distributions fit models. The distributions are, first, at $z = -768.56\,\mathrm{cm}$ in orange, where the temperature gradient to room temperature is located. Here, a deviation to higher velocities and correspondingly higher energies can be clearly seen. Secondly, there is a good agreement with the model at $z = -748.56\,\mathrm{cm}$ in blue just before the temperature gradient in the last beam tube where the facet temperature is predominately constant.

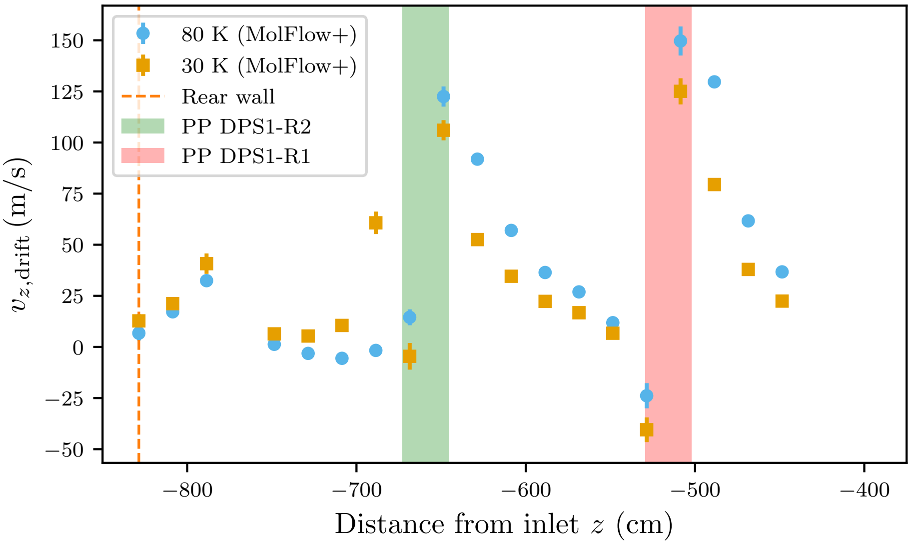

Figure 6.10.: Comparison of drift velocities at $T = 30\,\mathrm{K}$ and $T = 80\,\mathrm{K}$. The drift velocities at $r = 0\,\mathrm{cm}$ in the RW direction are higher for $T = 80\,\mathrm{K}$ as expected then to $T = 30\,\mathrm{K}$. After the second pump port the trend is reversed (see section 6.5.1). In the pumping regions there are deviations from the model assumption, so that the values in these regions are not reliable.

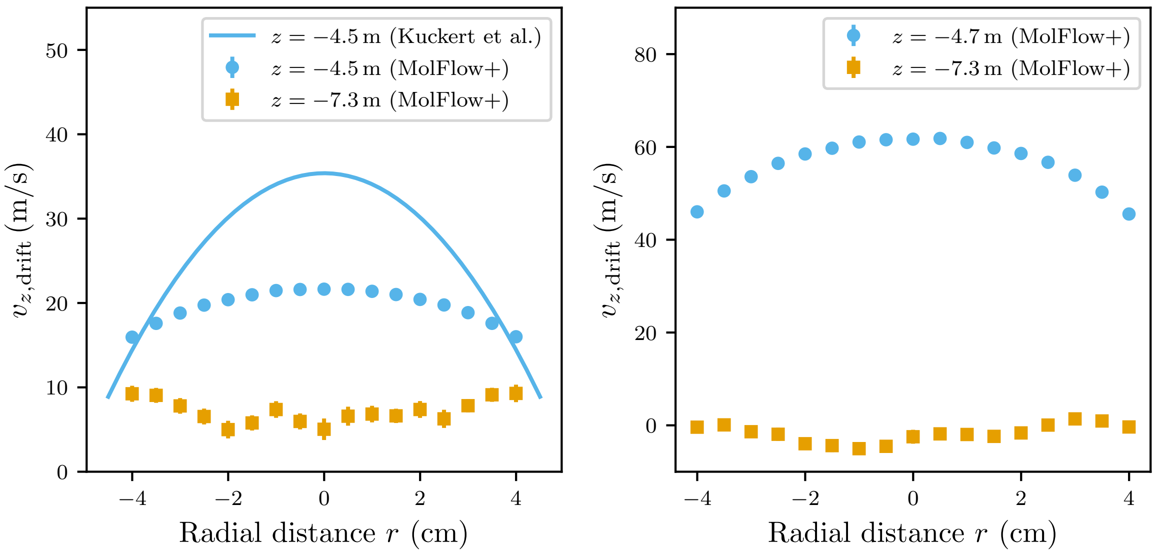

Figure 6.11.: Radial dependence of the drift velocity $v_{z,\mathrm{drift}}$ in comparison at different z-positions at $T = 30\,\mathrm{K}$ (left) and $T = 80\,\mathrm{K}$ (right). The comparison with the COMSOL simulations clearly shows that the radial velocities are underestimated at $z = -4.5\,\mathrm{m}$. This is due to the fact that at this point there is still the domain of the continuum flow. At $z = -7.3\,\mathrm{m}$ is the molecular flow regime and no previous simulations were available at this position. Most of the uncertainties for the MolFlow+ results are smaller than the marker size and no uncertainties were available for the COMSOL simulations.

the fit uncertainty was considered here the drift is most likely compatible with zero. And the particles move equally distributed in the front direction and in the direction of the rear wall due to the accumulation of particles in the last beam tube part which was discussed in section 6.4.

6.5.2. Radial dependence of $v_{z,\mathrm{drift}}$

In this section, the radial dependence of the drift velocity v_z is briefly discussed. In addition, it serves as a comparison of the deviation from the gas simulations with COMSOL. However, the simulations with COMSOL only extend to $z = -4.5\,\mathrm{m}$, so that only this position is compared in the following. Furthermore, like in the previous sections, the COMSOL values are only from the front side and mirrored at the center of the WGTS.

Figure 6.11 shows the comparison between the COMSOL and MolFlow+ simulations. At $z = -4.5\,\mathrm{m}$ the drift velocity is clearly underestimated compared to the COMSOL simulation. Due to the beaming effect the drift velocity has its maximum in the center of the beam tube and decreasing towards the beam tube surface. Moreover, the drift velocity is positive for all radii for $T = 30\,\mathrm{K}$. In this range the continuity regime prevails, so that the clear deviation was to be expected. At $z = -7.3\,\mathrm{m}$ and thus in the molecular flow regime, the shape of the curve changes and at $T = 80\,\mathrm{K}$ there are domains mainly in the center where the drift velocity is negative which would mean that the particles would drift away from the RW. Nevertheless, due to positive velocities particles at the edge of BT the particles still could reach the RW.

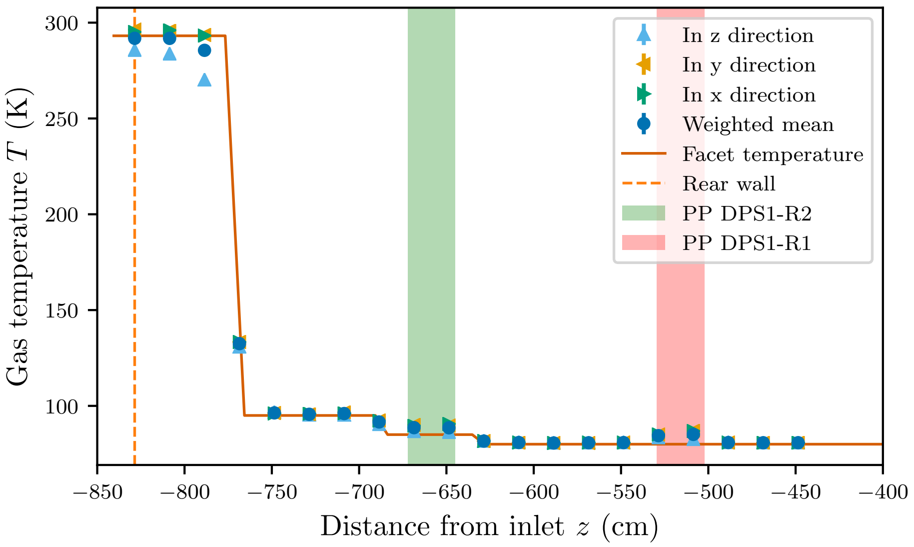

Figure 6.12.: Simulated gas temperature at $T = 80\,\mathrm{K}$. The temperature extracted from the Maxwell–Boltzmann distribution with the measurement facets perpendicular to x and y-direction is different from the facet perpendicular to z-direction. This could be because it is more likely that particles from cooler regions are detected in the z-direction. The weighted mean of the temperature takes into account the different number of hits on the three directional facets.

6.5.3. Gas temperature

The simulated velocity distributions can also be used to study the gas temperature of the neutral particles. In the frame of this thesis, gas temperature is used in section 6.6 to calculate the transversal motion of ions.

The absolute velocity distributions were also measured with the plane cross arrangement (see fig. 6.4). Since the measurement facets with the surface normal n_z measure more often the particles from the z-direction, the already existing facets with the surface normal in the y and in the x-direction, from the simulation of the velocity components are added for the calculation of the gas temperature. With a weighted average that takes into account the number of hits that the corresponding facets have been exposed to, an approximate estimate of the gas temperature can be made. A Poisson uncertainty was assumed on the number of hits. Using Gaussian error propagation, the uncertainty on the gas temperature was determined in combination with the fit uncertainty from the 3D Maxwell–Boltzmann distribution (see fig. 6.12).

With the gas temperature extracted from the 3D Maxwell–Boltzmann distribution of the absolute velocity, its longitudinal profile is now shown in figure 6.12. The deviation near the RW chamber could be due to the fact that the different orientations of the facets preferentially count the respective particles from the corresponding direction, so that in the z-direction, particles predominantly originate from the colder regions. The deviation is only clearly seen in the room temperature region of the RW chamber, where most of the neutrals have not interacted with the wall and are thus not yet at room temperature. The measuring facets oriented towards the wall mainly measure particles that have already interacted with the wall and have taken on its temperature. Therefore, the corresponding data points for the y- and x-direction lie well on top of each other.

Conclusion
It is now possible to perform gas simulations with MolFlow+ more precisely in rear direction. Furthermore, the simulated distributions of the individual velocity components can be implemented in the KARL code in the near future. To describe the motion of the neutral gas with few parameters, the drift velocity can be used as a rough description. The neutral gas density can describe the domain at the RW with the help of the COMSOL simulations, but reference simulations over the entire gas flow regime range at $T = 80\,\mathrm{K}$ are still needed. Further, it is possible to track the neutral gas temperature longitudinally and to infer the temperatures of the surfaces.

6.6. Mean free path and transversal motion of ions

In order to better understand the radial shape of the plasma, it is of interest to find out where along the beamline the ions mainly move to the beam tube wall. The ions reach the beam tube wall where the mobility has the highest values. With the results for the neutral particle density simulated in section 6.4, initial estimates can be made. More sophisticated investigations will be performed with the upcoming plasma simulations.

In the following, the experimental mobility of the dominant ion species ${T_3}^+$ [Kle19] is determined. The values are then compared with the theoretical determined results.

Experimental calculation
First the mobility of positive ions $\mu_\perp$ is calculated, which is required for the drift to the beam tube wall. For this, a homogeneous radial electric field $E_\perp$ is assumed:

$$E_\perp \approx \frac{U_{\mathrm{RW}} - \Delta\Phi_{\mathrm{RW-BT}}}{r_{\mathrm{BT}}} \, , \tag{6.10}$$

with U_{RW} as the applied RW voltage, optimal RW voltage $\Delta\Phi_{\mathrm{RW-BT}}$ and with radius of the beam tube r_{BT}.

The transversal current density can now be calculated with Ohm's law, which is composed of the conductivity $\sigma_\perp$ and the electric field $E_\perp$. Using the definition $\sigma_\perp = e\,n_{\mathrm{ion}}\,\mu_\perp$ the Ohm's law looks as follows:

$$J_\perp = \sigma_\perp \cdot E_\perp \tag{6.11}$$

$$= e\,n_{\mathrm{ion}}\,\mu_\perp \cdot E_\perp \, , \tag{6.12}$$

with n_{ion} as ion density and with elementary charge e.

The experimental values for ion mobility can be determined using an exemplary selected IU-scan. At a saturation voltage of $5.02\,\mathrm{V}$, only electrons reach the RW. This corresponds to the same rate of positive ions that are produced. With a saturation current at the RW of $248.91\,\mathrm{nA}$, this corresponds to a current density of $88.03\,\mathrm{nA}^2\,\mathrm{m}^{-1}$ evenly distributed over the $10\,\mathrm{m}$ BT mantle surface. The saturation current and voltage were taken from an IU-curve of a scan performed at $75\,\%$ CD and at $T_{\mathrm{WGTS}} = 80\,\mathrm{K}$ which are the same conditions as during tritium β-scans from KNM4 onward. For the ion density, a constant value of $n_{\mathrm{ion}} = 1 \times 10^{12}\,\mathrm{m}^{-3}$ based on MC simulations on ionization and recombination by Ferenc Glück is assumed.

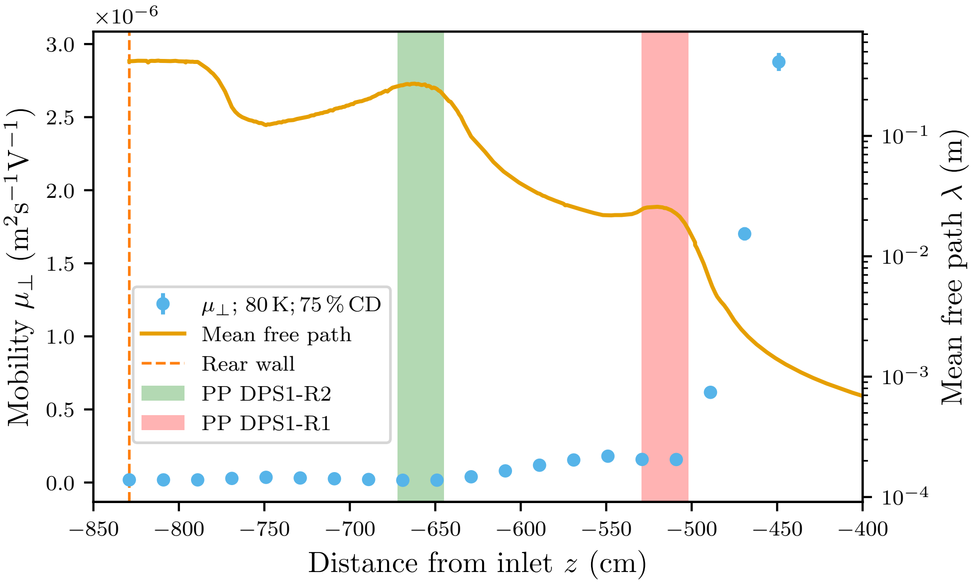

Figure 6.13.: Transversal mobility and mean free path of ions. The mobility of the ions is negligible from RW to the first pump port and increases from the first pump port towards the center of the WGTS.

Now the mobility of the ions can be calculated with:

$$\mu_\perp = \frac{J_\perp}{e\, n_{\text{ion}}\, E_\perp} \approx 5.05 \times 10^{-3}\, \text{m}^2\, \text{V}^{-1}\, \text{s}^{-1} \ . \tag{6.13}$$

Theoretical estimation

Furthermore, the transversal mobility can be determined with:

$$\mu_\perp = \frac{\nu_c}{\nu_c^2 - \Omega_{\text{ion}}^2} \cdot \frac{e}{m_{\text{ion}}} \ , \tag{6.14}$$

with the collision frequency of ions with neutral gas ν_c, Ω_{ion} as gyro frequency and m_{ion} as mass of $T_3{}^+$ [Bit13].

The probability of a collision can now be calculated with $P = s/\lambda$, with the distance s traversed at a corresponding density. Using $s = v{\cdot}t$ the collision frequency $\nu_c = P/t$ can now be determined as $\nu_c = v/\lambda$. Here, the velocity v was used with which the neutral gas particles move in the rest system of the bulk.

Due to missing values of the elastic scattering cross section $\sigma(E)$ for $T_3{}^+$ the corresponding cross section for $H_3{}^+$ are used for the calculation of the mean free path λ [TS00]:

$$\lambda = \frac{1}{\sigma(E) \cdot n(z)} \ , \tag{6.15}$$

where $n(z)$ denotes the neutral particle density in the source. In addition, it is assumed that the ions have the same temperature as neutral gas, which is justified by the obtained, small mean free path. For the calculation of the energy-dependent cross-section $\sigma(E)$, the simulation results shown in figure 6.12 are used.

Figure 6.13 shows the longitudinal distribution of the ion mobility. When the experimental and theoretical ion mobility are compared, it is found that they differ by three orders of magnitude from the RW to the first pump port. But the mobility was only calculated up to 400 mm away from the gas injection. As the T_2 density increases, the mobility increases linearly according to eq. 6.14 and 6.15 with $\nu_c \ll \Omega_{ion}$. If one further assumes that the ions continue to be drifted radially the closer they get to the WGTS center, one obtains mobilities of the order 1×10^{-5}, which still differ from the experimentally estimated value by two orders of magnitude. Moreover, the deviation from the experimental estimate cannot be improved in retrospect by a smaller area of the beam tube on which the ions impinge. A large uncertainty factor is the density of the ions, which is assumed to be constant but is in fact longitudinally dependent. This could be a possibility to explain the deviation. In summary, it can be said from the theoretical estimation that the predominant drift of the ions occurs in the center of the WGTS.

Chapter 7.

Conclusions and outlook

The KATRIN experiment measures the neutrino mass using the energy spectrum of tritium beta decay. A non-vanishing neutrino mass leads to a deformation of the spectrum, which is most distinct near the kinematic endpoint. To achieve the necessary count rates of 1 count per second (cps) on average in this region, KATRIN uses a high-luminosity windowless gaseous tritium source (WGTS) that provides 10^{11} beta electrons per second. As a consequence of beta decay, a self-ionizing plasma is formed in the WGTS, which is magnetized by the strong magnetic guiding field of 2.5 T and cooled down to 80 K or even 30 K. The plasma boundaries are provided by the rear wall (RW), which terminates the magnetic flux tube on the rear side and WGTS beam tube. These boundaries define the plasma potential, which serves as the starting potential for the beta electrons in the source. Spatial and temporal inhomogeneities of the plasma potential lead to a distortion of the measured beta spectrum causing a neutrino mass shift that needs to be accounted for.

Minimal radial inhomogeneity is expected at the so-called optimal RW voltage, which corresponds to the work function difference between RW and WGTS walls and can be determined with current measurements in the source during sweeps of the RW voltage (IU scans). The currents are caused by ions and electrons from the plasma, which are neutralized at the RW (rear side) and dipole electrodes in the differential pumping section (DPS; front side).

Within the scope of this thesis an uncertainty on the optimal RW voltage was derived. The calculated sweep-wise statistical uncertainty on the optimal RW voltage data points from IU-scans is 3.68 mV during KATRIN neutrino mass measurement phase (KNM)4 and 3.52 mV in KNM5c for of about 15 min IU-scans. Compared to about three hours long high activity krypton-V measurements with an uncertainty of approximately 10 meV to the N23-line positions from a uniform fit[1], this uncertainty is negligible. (section 5.2.2)

During the operation of the tritium source a drift of the optimal RW voltage was observed. The drifts can be divided into several categories including burn-in phase after the restart of the tritium circulation, a long-term drift during the tritium circulation and hysteresis effect during IU-scans. The drift during the burn-in phase has shown a strong correlation of 0.93 with the tritium purity, indicating that adsorbed impurities such as hydrocarbons on the RW or on the beam tube are causing the change of work functions. In the case of long-term drift, no strong correlation with tritium purity or column density was found. (section 5.2.3) Hysteresis was not explicitly investigated, but a strong qualitative correlation with RW voltage changes was observed. (section 5.3.2)

---

[1] Matthias Böttcher, internal communication, July 9th, 2021.

Regarding the physical cause of the drifts, if it is charging or adsorption, could not be fully resolved. It is likely that adsorption on the RW during burn-in phase in KNM5 is involved, but it is not possible to distinguish whether it is a global change in work function or charging of insulating patches. (section 5.3.3)

It was observed that a change in the RW bias causes a drift in the optimal RW voltage in the direction of the voltage change. In addition, the drift scales with the magnitude of the voltage change and can be reversed. (section 5.3.2) There is also indication that between the change of the RW bias, the work function of the RW changes more compared to the work function of the beam tube. (section 5.3.4)

During the IU-scans, a characteristic ‘peak’, which actually corresponds to a decrease of the measured ions, in the total DPS current is observed. It is assumed that the peak is caused by neutralization processes in the source. The total DPS current peak shows a good correlation of 0.78 with the optimal RW voltage during the burn-in phase in KNM4. However, in the linear long-term drift phase, the drifts differ significantly by a factor of 7. Therefore, the monitoring of the optimal RW voltage drift is not possible with the total DPS current peak. The reason for the different drifts could be that in addition to the drifts of the RW and beam tube work functions, drifts in the DPS are possibly also measured. (section 5.3.5)

Since no evidence for the cause of the long-term drift could be found, further investigations are necessary in the future to be able to eliminate it.
For the evaluation of continuous currents, the use of neural networks in terms of determining the optimal RW voltage is being investigated. Uncertainties of about 3 mV, comparable to like those determined in this thesis have already been achieved. Neural networks also provide a possibility to determine the work function differences between the periodic IU-scans based on an implicit model for the voltage dependence of the currents measured at the RW and DPS dipole electrodes.
Coincident spikes in the continuous current measurements at the RW and the DPS could indicate extended plasma instabilities. Such a temporal variation of the plasma potential would lead to a neutrino mass shift, which could be avoided by cutting out the FPD data measured during the spikes.

To understand the plasma in the source, simulations of electric and magnetic fields are necessary. For this purpose, it was essential to know the particle density and the velocities of the neutral gas. The results can be incorporated as input parameters in the KARL simulation software in the near future. Before the start of this thesis, only gas simulations between the WGTS and cryogenic pumping section (CPS) had been performed. Simulations of the particle density (section 6.4) and velocities (section 6.5) of the neutral gas particles from the center of the WGTS to the RW with MolFlow+ for 30 K and for 80 K were successfully performed. The simulation results were compared with already available COMSOL simulation, which was performed over the entire gas flow regime at 30 K. The values of COMSOL are from the front side and were mirrored at the center of WGTS.

A significant difference in particle density was found near the RW, this is due to the weak pumping speed at rear section compared to the high pumping speeds in the DPS. Furthermore, the uncertainty on the particle density obtained with MolFlow+ is smaller in the molecular flow regime compared to the reference simulation.

Using the simulation results for the gas density and velocity, an estimate of transversal ion mobility could be made. According to the theoretical estimation, the transversal drift of ions in the central 10 m of the WGTS beam tube dominates (section 6.6). Compared to the center of the WGTS, the ion drift between WGTS and RW can be considered negligible. The Monte Carlo simulations by Ferenc Glück and plasma simulations with a two-dimensional axially symmetric three-fluid model by Laura Kuckert [Kuc16] could still provide consistent conclusions about the plasma potential. Because the RW was placed at the end of the central 10 m beam tube in these plasma simulations, therefore effects occurring between the WGTS and the actual position of the RW were not considered. However, since rough assumptions were made in the theoretical calculation of the transversal ion mobility, the current new microscopic particle-in-cell simulations will be needed from Jonas Kellerer to investigate the plasma effects between RW and WGTS.

Appendix A.

Calculations

The pressure p on a facet is proportional to the number of particles that have hit the facet divided by the number of total desorbed particles:

$$p \propto \frac{N_{\mathrm{hits}}}{N_{\mathrm{des}}} \ . \tag{A.1}$$

This leads to an uncertainty on the pressure of:

$$\Delta p \propto \frac{\Delta N_{\mathrm{hits}}}{N_{\mathrm{des}}} \ . \tag{A.2}$$

The assumption that the hits are poisson distributed results in an uncertainty of $\Delta N_{\mathrm{hits}} = \sqrt{N_{\mathrm{hits}}}$. After dividing the equation A.2 by A.1 and using the proportionality of pressure and particle density, this gives an uncertainty in particle density of

$$\Delta n = \frac{n}{\sqrt{N_{\mathrm{hits}}}} \ . \tag{A.3}$$

Appendix B.

Additional figures

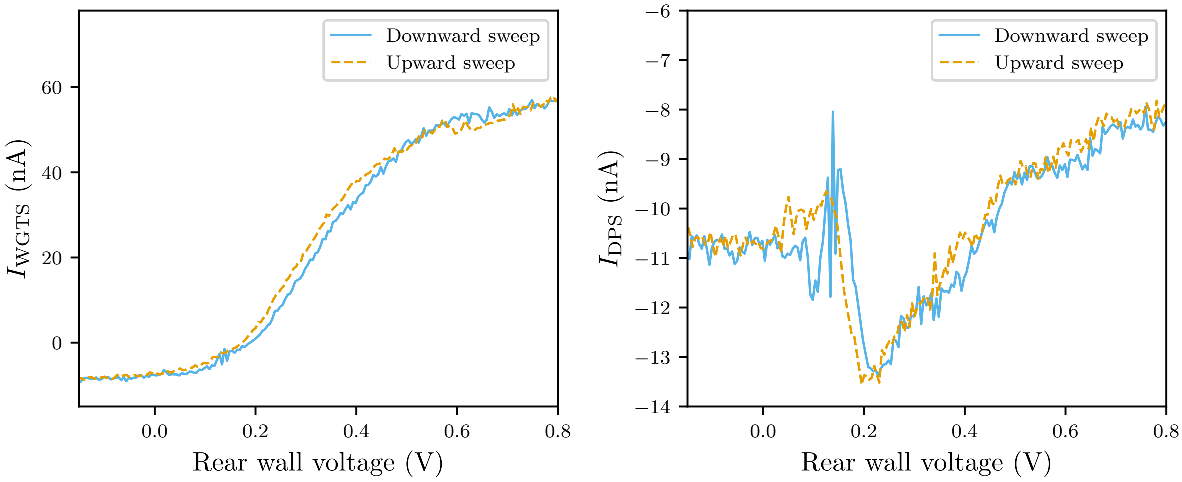

Figure B.1.: Hysteresis effect of an IU-scan during KNM3. A possible physical reason could be charging effects due to dielectric patches leading to a change of the effective surface potential. The hysteresis shown was measured at 35 % CD with a source temperature of $T = 80\,\mathrm{K}$ on 14.06.2020 with a RW voltage scan range of $(-3 \ldots +6)\,\mathrm{V}$.

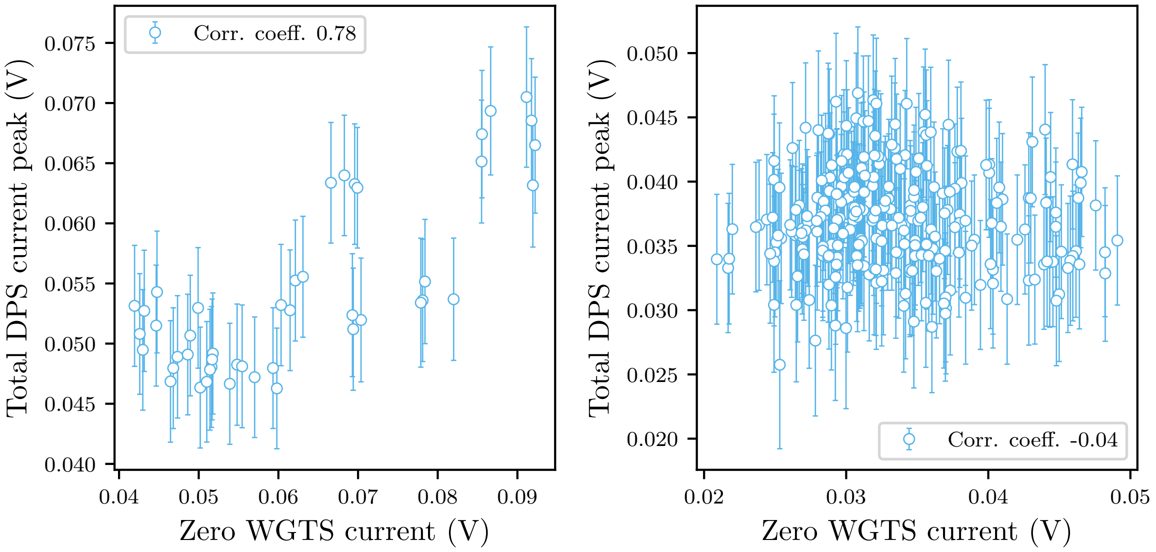

Figure B.2.: Correlation between the total DPS current peak and Zero WGTS currents during burn-in (left) and the linear long-term drift phase (right) in KNM4.

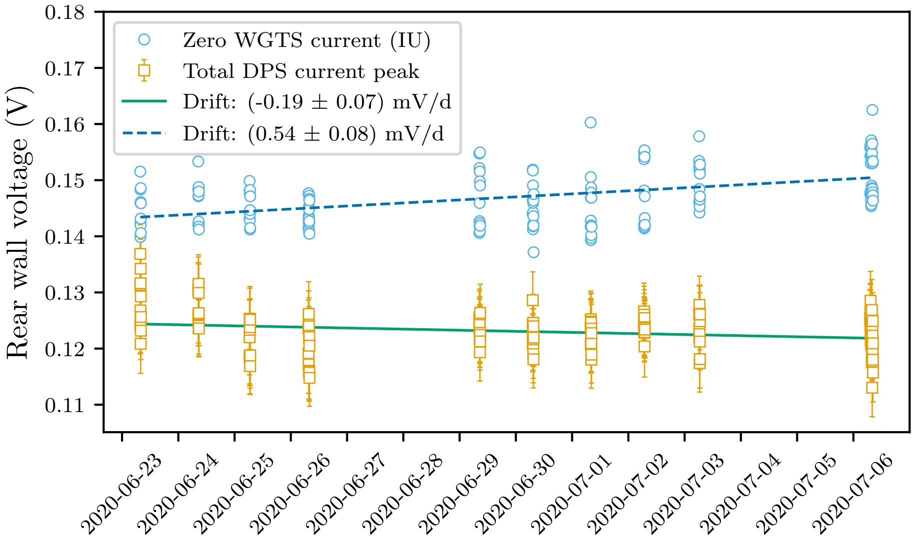

Figure B.3.: Comparison of Zero WGTS current and total DPS current peak drifts during KNM3a.

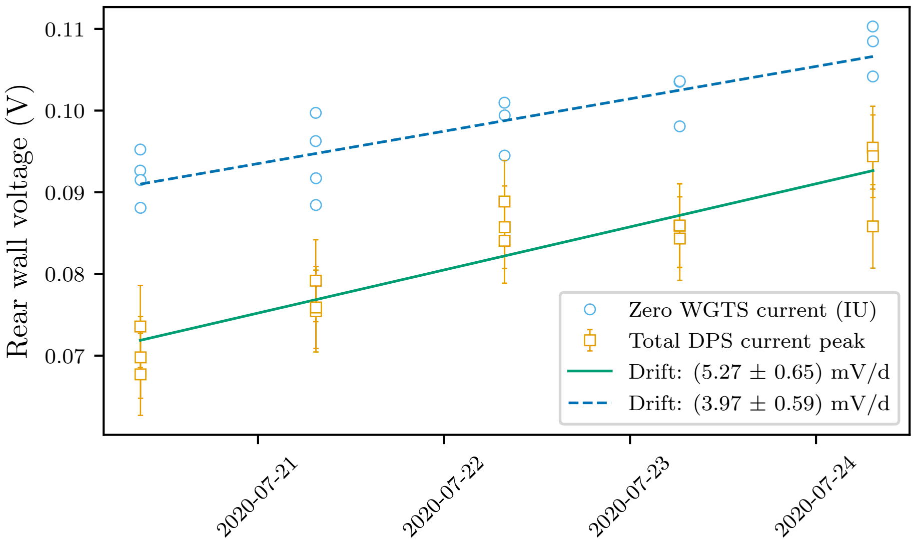

Figure B.4.: Comparison of Zero WGTS current and total DPS current peak drifts during KNM3b at 75 % CD.

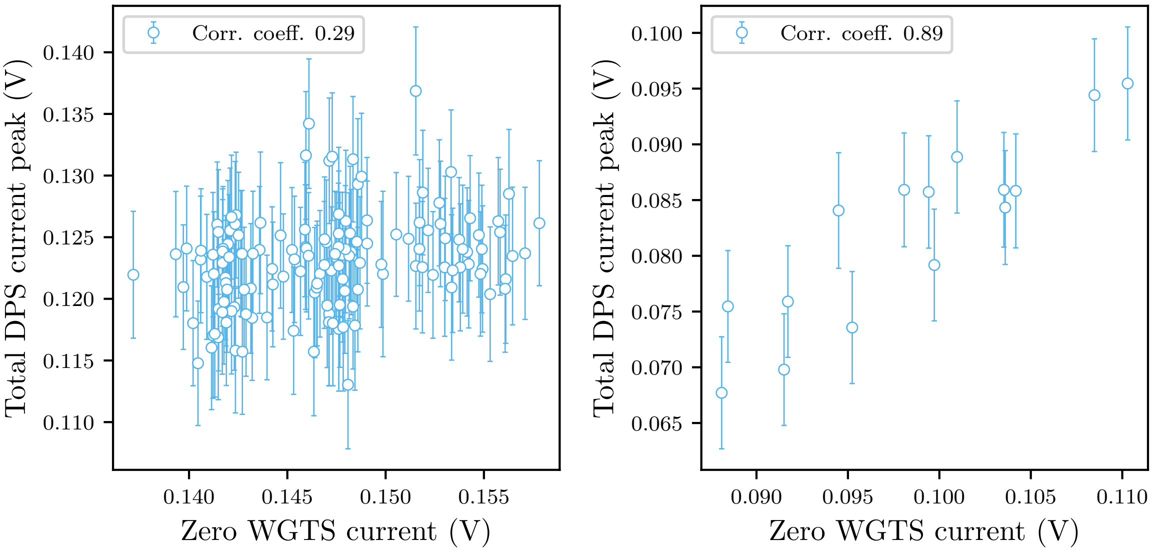

Figure B.5.: Correlation of Zero WGTS current and total DPS current peak drifts during KNM3a (left) and KNM3b (right).

Appendix C.

Data sheets

C.1. rbd 9103

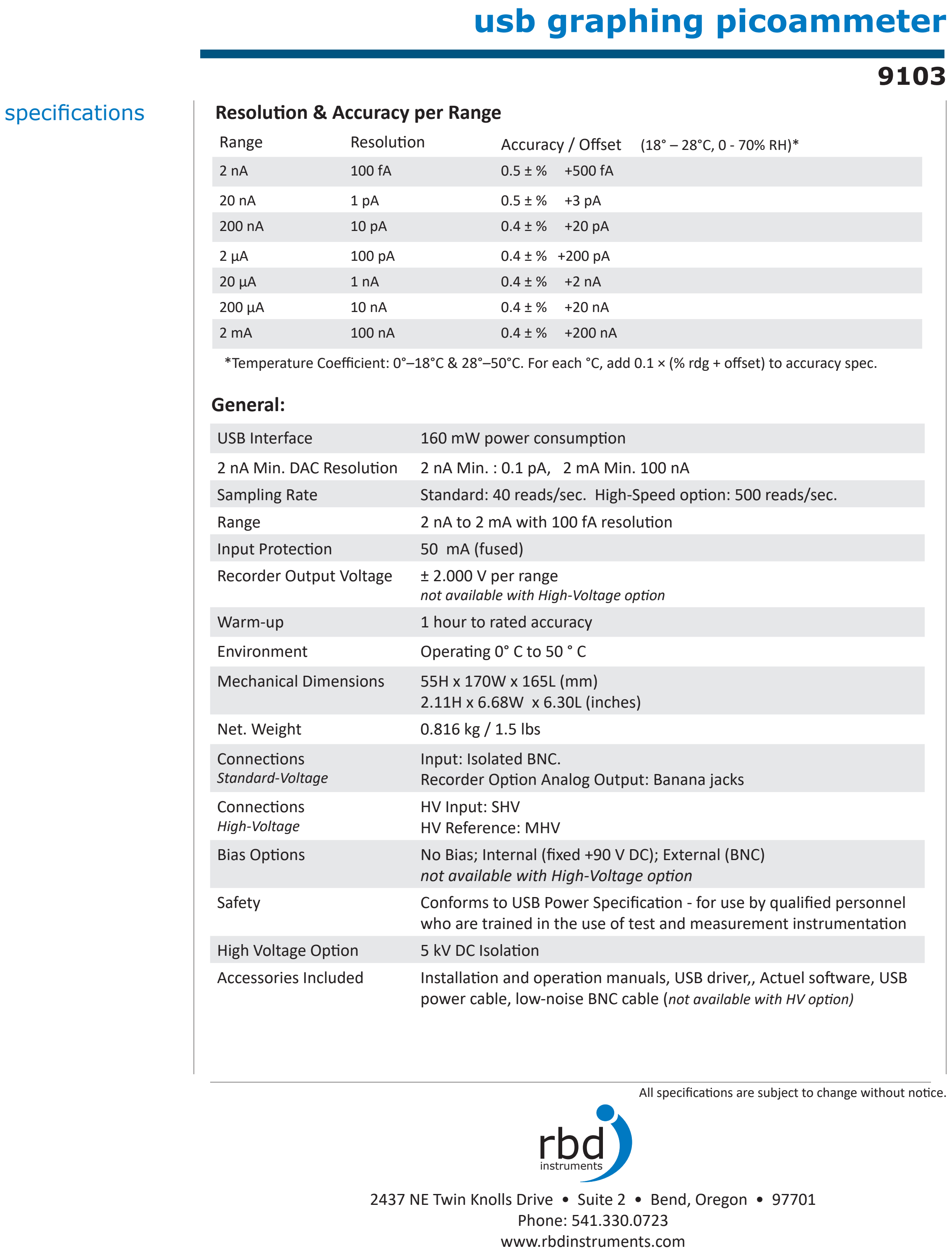

usb graphing picoammeter

9103

specifications

Resolution & Accuracy per Range

Range	Resolution	Accuracy / Offset	(18° – 28°C, 0 - 70% RH)*
2 nA	100 fA	0.5 ± %	+500 fA
20 nA	1 pA	0.5 ± %	+3 pA
200 nA	10 pA	0.4 ± %	+20 pA
2 µA	100 pA	0.4 ± %	+200 pA
20 µA	1 nA	0.4 ± %	+2 nA
200 µA	10 nA	0.4 ± %	+20 nA
2 mA	100 nA	0.4 ± %	+200 nA

*Temperature Coefficient: 0°–18°C & 28°–50°C. For each °C, add 0.1 × (% rdg + offset) to accuracy spec.

General:

USB Interface	160 mW power consumption
2 nA Min. DAC Resolution	2 nA Min. : 0.1 pA, 2 mA Min. 100 nA
Sampling Rate	Standard: 40 reads/sec. High-Speed option: 500 reads/sec.
Range	2 nA to 2 mA with 100 fA resolution
Input Protection	50 mA (fused)
Recorder Output Voltage	± 2.000 V per range *not available with High-Voltage option*
Warm-up	1 hour to rated accuracy
Environment	Operating 0° C to 50 ° C
Mechanical Dimensions	55H x 170W x 165L (mm) 2.11H x 6.68W x 6.30L (inches)
Net. Weight	0.816 kg / 1.5 lbs
Connections *Standard-Voltage*	Input: Isolated BNC. Recorder Option Analog Output: Banana jacks
Connections *High-Voltage*	HV Input: SHV HV Reference: MHV
Bias Options	No Bias; Internal (fixed +90 V DC); External (BNC) *not available with High-Voltage option*
Safety	Conforms to USB Power Specification - for use by qualified personnel who are trained in the use of test and measurement instrumentation
High Voltage Option	5 kV DC Isolation
Accessories Included	Installation and operation manuals, USB driver,, Actuel software, USB power cable, low-noise BNC cable (*not available with HV option)*

rbd
instruments

2437 NE Twin Knolls Drive • Suite 2 • Bend, Oregon • 97701
Phone: 541.330.0723
www.rbdinstruments.com

C.2. Keithley 6487

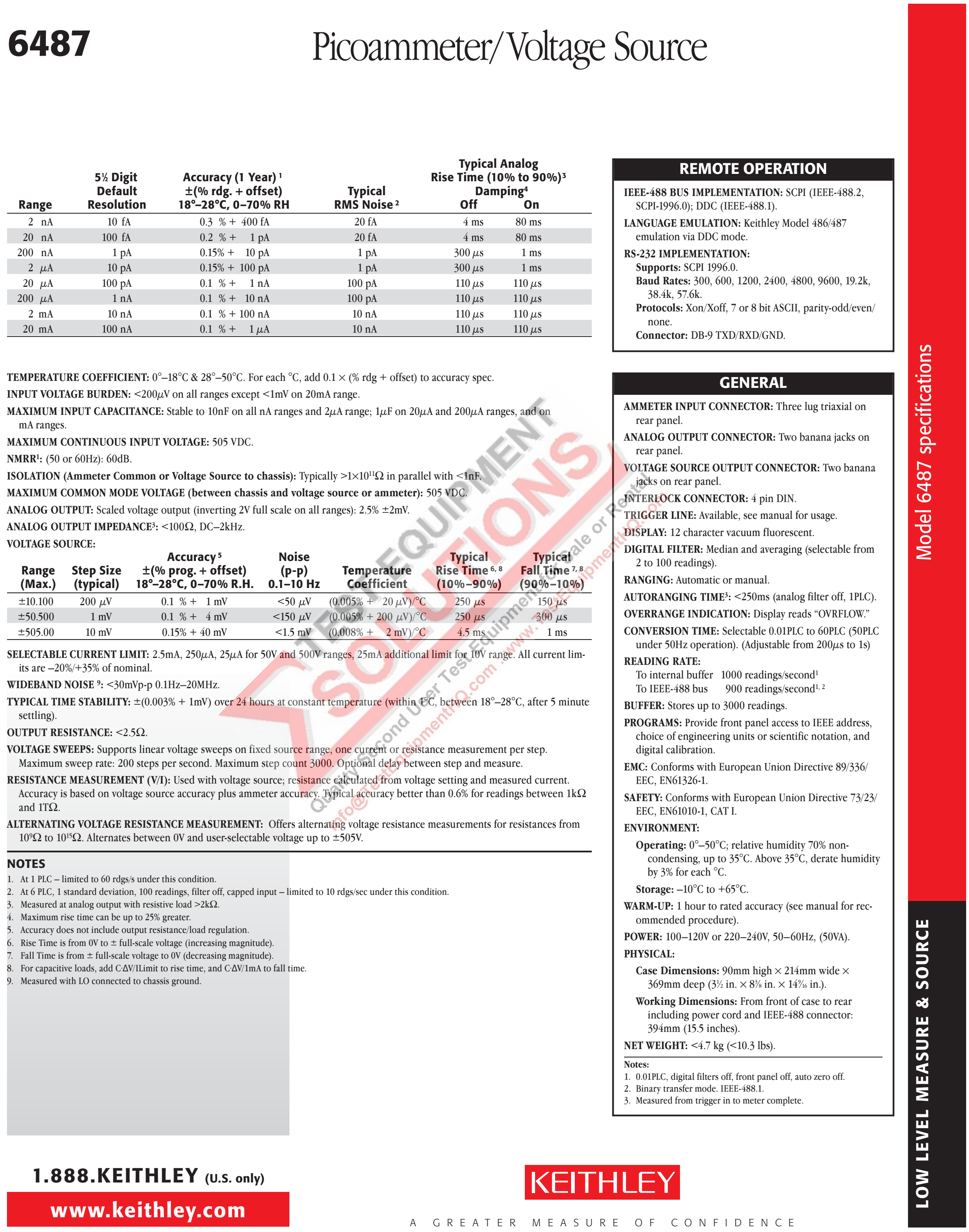

6487

Picoammeter/Voltage Source

Range	5½ Digit Default Resolution	Accuracy (1 Year) [1] ±(% rdg. + offset) 18°–28°C, 0–70% RH	Typical RMS Noise [2]	Typical Analog Rise Time (10% to 90%)[3] Damping[4] Off	On
2 nA	10 fA	0.3 % + 400 fA	20 fA	4 ms	80 ms
20 nA	100 fA	0.2 % + 1 pA	20 fA	4 ms	80 ms
200 nA	1 pA	0.15% + 10 pA	1 pA	300 µs	1 ms
2 µA	10 pA	0.15% + 100 pA	1 pA	300 µs	1 ms
20 µA	100 pA	0.1 % + 1 nA	100 pA	110 µs	110 µs
200 µA	1 nA	0.1 % + 10 nA	100 pA	110 µs	110 µs
2 mA	10 nA	0.1 % + 100 nA	10 nA	110 µs	110 µs
20 mA	100 nA	0.1 % + 1 µA	10 nA	110 µs	110 µs

TEMPERATURE COEFFICIENT: 0°–18°C & 28°–50°C. For each °C, add 0.1 × (% rdg + offset) to accuracy spec.

INPUT VOLTAGE BURDEN: <200µV on all ranges except <1mV on 20mA range.

MAXIMUM INPUT CAPACITANCE: Stable to 10nF on all nA ranges and 2µA range; 1µF on 20µA and 200µA ranges, and on mA ranges.

MAXIMUM CONTINUOUS INPUT VOLTAGE: 505 VDC.

NMRR[1]: (50 or 60Hz): 60dB.

ISOLATION (Ammeter Common or Voltage Source to chassis): Typically $>1\times10^{11}\Omega$ in parallel with <1nF.

MAXIMUM COMMON MODE VOLTAGE (between chassis and voltage source or ammeter): 505 VDC.

ANALOG OUTPUT: Scaled voltage output (inverting 2V full scale on all ranges): 2.5% ±2mV.

ANALOG OUTPUT IMPEDANCE[3]: <100Ω, DC–2kHz.

VOLTAGE SOURCE:

Range (Max.)	Step Size (typical)	Accuracy [5] ±(% prog. + offset) 18°–28°C, 0–70% R.H.	Noise (p-p) 0.1–10 Hz	Temperature Coefficient	Typical Rise Time [6, 8] (10%–90%)	Typical Fall Time [7, 8] (90%–10%)
±10.100	200 µV	0.1 % + 1 mV	<50 µV	(0.005% + 20 µV)/°C	250 µs	150 µs
±50.500	1 mV	0.1 % + 4 mV	<150 µV	(0.005% + 200 µV)/°C	250 µs	300 µs
±505.00	10 mV	0.15% + 40 mV	<1.5 mV	(0.008% + 2 mV)/°C	4.5 ms	1 ms

SELECTABLE CURRENT LIMIT: 2.5mA, 250µA, 25µA for 50V and 500V ranges, 25mA additional limit for 10V range. All current limits are –20%/+35% of nominal.

WIDEBAND NOISE [9]: <30mVp-p 0.1Hz–20MHz.

TYPICAL TIME STABILITY: ±(0.003% + 1mV) over 24 hours at constant temperature (within 1°C, between 18°–28°C, after 5 minute settling).

OUTPUT RESISTANCE: <2.5Ω.

VOLTAGE SWEEPS: Supports linear voltage sweeps on fixed source range, one current or resistance measurement per step. Maximum sweep rate: 200 steps per second. Maximum step count 3000. Optional delay between step and measure.

RESISTANCE MEASUREMENT (V/I): Used with voltage source; resistance calculated from voltage setting and measured current. Accuracy is based on voltage source accuracy plus ammeter accuracy. Typical accuracy better than 0.6% for readings between 1kΩ and 1TΩ.

ALTERNATING VOLTAGE RESISTANCE MEASUREMENT: Offers alternating voltage resistance measurements for resistances from $10^{9}\Omega$ to $10^{15}\Omega$. Alternates between 0V and user-selectable voltage up to ±505V.

NOTES

1. At 1 PLC – limited to 60 rdgs/s under this condition.
2. At 6 PLC, 1 standard deviation, 100 readings, filter off, capped input – limited to 10 rdgs/sec under this condition.
3. Measured at analog output with resistive load >2kΩ.
4. Maximum rise time can be up to 25% greater.
5. Accuracy does not include output resistance/load regulation.
6. Rise Time is from 0V to ± full-scale voltage (increasing magnitude).
7. Fall Time is from ± full-scale voltage to 0V (decreasing magnitude).
8. For capacitive loads, add C·ΔV/ILimit to rise time, and C·ΔV/1mA to fall time.
9. Measured with LO connected to chassis ground.

REMOTE OPERATION

IEEE-488 BUS IMPLEMENTATION: SCPI (IEEE-488.2, SCPI-1996.0); DDC (IEEE-488.1).

LANGUAGE EMULATION: Keithley Model 486/487 emulation via DDC mode.

RS-232 IMPLEMENTATION:
- **Supports:** SCPI 1996.0.
- **Baud Rates:** 300, 600, 1200, 2400, 4800, 9600, 19.2k, 38.4k, 57.6k.
- **Protocols:** Xon/Xoff, 7 or 8 bit ASCII, parity-odd/even/none.
- **Connector:** DB-9 TXD/RXD/GND.

GENERAL

AMMETER INPUT CONNECTOR: Three lug triaxial on rear panel.

ANALOG OUTPUT CONNECTOR: Two banana jacks on rear panel.

VOLTAGE SOURCE OUTPUT CONNECTOR: Two banana jacks on rear panel.

INTERLOCK CONNECTOR: 4 pin DIN.

TRIGGER LINE: Available, see manual for usage.

DISPLAY: 12 character vacuum fluorescent.

DIGITAL FILTER: Median and averaging (selectable from 2 to 100 readings).

RANGING: Automatic or manual.

AUTORANGING TIME[3]: <250ms (analog filter off, 1PLC).

OVERRANGE INDICATION: Display reads "OVRFLOW."

CONVERSION TIME: Selectable 0.01PLC to 60PLC (50PLC under 50Hz operation). (Adjustable from 200µs to 1s)

READING RATE:

To internal buffer	1000 readings/second[1]
To IEEE-488 bus	900 readings/second[1, 2]

BUFFER: Stores up to 3000 readings.

PROGRAMS: Provide front panel access to IEEE address, choice of engineering units or scientific notation, and digital calibration.

EMC: Conforms with European Union Directive 89/336/EEC, EN61326-1.

SAFETY: Conforms with European Union Directive 73/23/EEC, EN61010-1, CAT I.

ENVIRONMENT:
- **Operating:** 0°–50°C; relative humidity 70% non-condensing, up to 35°C. Above 35°C, derate humidity by 3% for each °C.
- **Storage:** –10°C to +65°C.

WARM-UP: 1 hour to rated accuracy (see manual for recommended procedure).

POWER: 100–120V or 220–240V, 50–60Hz, (50VA).

PHYSICAL:
- **Case Dimensions:** 90mm high × 214mm wide × 369mm deep (3½ in. × 8⅜ in. × 14⁹⁄₁₆ in.).
- **Working Dimensions:** From front of case to rear including power cord and IEEE-488 connector: 394mm (15.5 inches).

NET WEIGHT: <4.7 kg (<10.3 lbs).

Notes:
1. 0.01PLC, digital filters off, front panel off, auto zero off.
2. Binary transfer mode. IEEE-488.1.
3. Measured from trigger in to meter complete.

Model 6487 specifications

LOW LEVEL MEASURE & SOURCE

1.888.KEITHLEY (U.S. only)

www.keithley.com

KEITHLEY

A GREATER MEASURE OF CONFIDENCE

Bibliography

[Ady16] M. Ady. “Monte Carlo simulations of ultra high vacuum and synchrotron radiation for particle accelerators”. Presented 03 May 2016. PhD thesis. CERN, May 2016.

[Agh+20] N. Aghanim et al. “Planck 2018 results”. In: *Astronomy and Astrophysics* 641 (Sept. 2020), A6. ISSN: 1432-0746. DOI: `10.1051/0004-6361/201833910`.

[Ahm+02] Q. R. Ahmad et al. “Direct Evidence for Neutrino Flavor Transformation from Neutral-Current Interactions in the Sudbury Neutrino Observatory”. In: *Phys. Rev. Lett.* 89 (1 June 2002), p. 011301. DOI: `10.1103/PhysRevLett.89.011301`.

[AK+14] M. Ady, R. Kersevan, et al. “Introduction to the Latest Version of the Test-particle Monte Carlo Code Molflow+”. In: *Proc. of IPAC* (2014), p. 2348.

[Ake+19] M. Aker et al. “Improved Upper Limit on the Neutrino Mass from a Direct Kinematic Method by KATRIN”. In: *Phys. Rev. Lett.* 123 (22 Nov. 2019), p. 221802. DOI: `10.1103/PhysRevLett.123.221802`.

[Ake+21a] M. Aker et al. *First direct neutrino-mass measurement with sub-eV sensitivity.* 2021. arXiv: `2105.08533 [hep-ex]`.

[Ake+21b] M. Aker et al. *The Design, Construction, and Commissioning of the KATRIN Experiment.* 2021. arXiv: `2103.04755 [physics.ins-det]`.

[Akeep] M. Aker. “Tritium sources for neutrino experiments: Stability and interactions of tritium with key surfaces (Preliminary)”. PhD thesis. Karlsruher Institut für Technologie (KIT), in prep.

[AM+76] N. W. Ashcroft, N. D. Mermin, et al. *Solid state physics.* Vol. 2005. holt, rinehart and winston, new york London, 1976.

[Ams+15] J. F. Amsbaugh et al. “Focal-plane detector system for the KATRIN experiment”. In: *Nuclear Instruments and Methods in Physics Research Section A: Accelerators, Spectrometers, Detectors and Associated Equipment* 778 (2015), pp. 40–60. DOI: `10.1016/j.nima.2014.12.116`.

[Ams15] C. Amsler. *Nuclear and Particle Physics.* 2053-2563. IOP Publishing, 2015. ISBN: 978-0-7503-1140-3. DOI: `10.1088/978-0-7503-1140-3`.

[Are+16] M. Arenz et al. “Commissioning of the vacuum system of the KATRIN Main Spectrometer”. In: *Journal of Instrumentation* 11 (2016), P04011. DOI: `10.1088/1748-0221/11/04/P04011`. arXiv: `1603.01014 [physics.ins-det]`.

[Ase+11] V. N. Aseev et al. “Upper limit on the electron antineutrino mass from the Troitsk experiment”. In: *Physical Review D* 84 (11 2011), p. 112003. DOI: `10.1103/PhysRevD.84.112003`.

[Bab+12] M. Babutzka et al. “Monitoring of the operating parameters of the KATRIN Windowless Gaseous Tritium Source”. In: *New Journal of Physics* 14.10 (2012), p. 103046. DOI: `10.1088/1367-2630/14/10/103046`.

[Bab14] M. Babutzka. “Design and development for the Rearsection of the KATRIN experiment”. PhD thesis. Karlsruher Institut für Technologie (KIT), 2014. DOI: `10.5445/IR/1000045598`.

[Bah64] J. N. Bahcall. “Solar neutrinos. I: Theoretical”. In: *Phys. Rev. Lett.* 12 (1964), pp. 300–302. DOI: `10.1103/PhysRevLett.12.300`.

[Bit13] J. A. Bittencourt. *Fundamentals of plasma physics.* Springer Science & Business Media, 2013.

[Bla21] J. Blaschtschak. “Drifts of the plasma potential in the KATRIN tritium source and their impact on the neutrino mass measurements”. MA thesis. Karlsruher Institut für Technologie (KIT), Feb. 2021.

[Bloep] F. Block. “Magnetic Field Systematics and Statistical Data Analysis Tools for Neutrino Mass Analysis with KATRIN (Preliminary)”. PhD thesis. Karlsruher Institut für Technologie (KIT), in prep.

[Boy19] A. Boyle. “Understanding neutrino mass constraints from galaxy clustering and CMB lensing”. PhD thesis. Ludwig-Maximilians-Universität München, Sept. 2019.

[BP34] H. Bethe and R. Peierls. “The “Neutrino””. In: *Nature* 133.532 (1934). DOI: `10.1038/133532a0`.

[Cha14] J. Chadwick. “Intensitätsverteilung im magnetischen Spectrum der β-Strahlen von radium B + C”. In: *Verhandl. Dtsc. Phys. Ges.* 16 (1914), p. 383.

[Chi+10] S. Chilingaryan et al. “Advanced data extraction infrastructure: Web based system for management of time series data”. In: *Journal of Physics: Conference Series* 219.4 (2010), p. 042034. DOI: `10.1088/1742-6596/219/4/042034`.

[Col05] KATRIN Collaboration. *KATRIN design report 2004.* Tech. rep. 51.54.01; LK 01. Forschungszentrum, Karlsruhe, 2005. 245 pp. DOI: `10.5445/IR/270060419`.

[Cow+56] C. L. Cowan et al. “Detection of the Free Neutrino: a Confirmation”. In: *Science* 124.3212 (1956), pp. 103–104. ISSN: 0036-8075. DOI: `10.1126/science.124.3212.103`. eprint: `https://science.sciencemag.org/content/124/3212/103.full.pdf`.

[Dan+62] G. Danby et al. “Observation of High-Energy Neutrino Reactions and the Existence of Two Kinds of Neutrinos”. In: *Phys. Rev. Lett.* 9 (1 July 1962), pp. 36–44. DOI: `10.1103/PhysRevLett.9.36`.

[DAr74] R. J. D’Arcy. “Dielectric impurities and surface instability in Langmuir probe plasma measurements”. In: *Journal of Physics D: Applied Physics* 7.10 (July 1974), pp. 1391–1401. DOI: `10.1088/0022-3727/7/10/312`.

[Dav94] R. Davis. “A review of the homestake solar neutrino experiment”. In: *Progress in Particle and Nuclear Physics* 32 (1994), pp. 13–32. ISSN: 0146-6410. DOI: `10.1016/0146-6410(94)90004-3`.

[Din+05] A. Dinklage et al. *Plasma physics: confinement, transport and collective effects.* Vol. 670. Springer Science & Business Media, 2005.

[Ell19] E. Ellinger. “Development and Investigation of the Forward Beam Monitor for the KATRIN experiment”. PhD thesis. Bergische Universität Wuppertal, 2019. DOI: `10.25926/r160-7a40`.

[EM17] J. Engel and J. Menéndez. “Status and future of nuclear matrix elements for neutrinoless double-beta decay: a review”. In: *Reports on Progress in Physics* 80.4 (Mar. 2017), p. 046301. ISSN: 1361-6633. DOI: `10.1088/1361-6633/aa5bc5`.

[Erh+18] M. Erhard et al. “Technical design and commissioning of the KATRIN large-volume air coil system”. In: *Journal of Instrumentation* 13.02 (2018), P02003. DOI: `10.1088/1748-0221/13/02/P02003`.

[Est+20] I. Esteban et al. “The fate of hints: updated global analysis of three-flavor neutrino oscillations”. In: *Journal of High Energy Physics* 2020.9 (Sept. 2020). ISSN: 1029-8479. DOI: `10.1007/jhep09(2020)178`.

[FA03] D. C. Faircloth and N. L. Allen. “High resolution measurements of surface charge densities on insulator surfaces”. In: *IEEE Transactions on Dielectrics and Electrical Insulation* 10.2 (2003), pp. 285–290. DOI: `10.1109/TDEI.2003.1194112`.

[Fer34] E. Fermi. “Versuch einer Theorie der β-Strahlen.” In: *Zeitschrift für Physik* 88.3–4 (1934), pp. 161–177. DOI: `10.1007/BF01351864`.

[Frä+11] F. M. Fränkle et al. “Radon induced background processes in the KATRIN pre-spectrometer”. In: *Astroparticle Physics* 35.3 (2011), pp. 128–134. DOI: `10.1016/j.astropartphys.2011.06.009`.

[Fri+19] F. Friedel et al. “Time-dependent simulation of the flow reduction of D_2 and T_2 in the KATRIN experiment”. In: *Vacuum* 159 (2019), pp. 161–172. ISSN: 0042-207X. DOI: `10.1016/j.vacuum.2018.10.002`.

[Fri20] F. R. Friedel. “Ion and plasma systematics during the first KATRIN neutrino mass measurements”. 51.03.01; LK 01. PhD thesis. Karlsruher Institut für Technologie (KIT), 2020. 226 pp. DOI: `10.5445/IR/1000126837`.

[Fuk+98] Y. Fukuda et al. “Evidence for Oscillation of Atmospheric Neutrinos”. In: *Phys. Rev. Lett.* 81 (8 Aug. 1998), pp. 1562–1567. DOI: `10.1103/PhysRevLett.81.1562`.

[Gal12] P. Gallagher. *Introduction to Plasma Physics (PY5012) [online] [Accessed on: 20.06.2021]*. 2012. URL: `https://www.tcd.ie/Physics/people/Peter.Gallagher/lectures/PlasmaPhysics/Lecture1n2_basic_properties.pdf`.

[Gan+16] A. Gando et al. “Search for Majorana Neutrinos Near the Inverted Mass Hierarchy Region with KamLAND-Zen”. In: *Phys. Rev. Lett.* 117 (8 Aug. 2016), p. 082503. DOI: `10.1103/PhysRevLett.117.082503`.

[Gas+14] L. Gastaldo et al. “The Electron Capture 163 Ho Experiment ECHo”. In: *Journal of Low Temperature Physics* 176.5-6 (May 2014), pp. 876–884. ISSN: 1573-7357. DOI: `10.1007/s10909-014-1187-4`.

[Gia+21] A. Giachero et al. “Progress in the Development of TES Microcalorimeter Detectors Suitable for Neutrino Mass Measurement”. In: *IEEE Transactions on Applied Superconductivity* 31.5 (2021), pp. 1–5. DOI: `10.1109/TASC.2021.3051104`.

[Gro+20] Particle Data Group et al. “Review of Particle Physics”. In: *Progress of Theoretical and Experimental Physics* 2020.8 (Aug. 2020). 083C01. ISSN: 2050-3911. DOI: `10.1093/ptep/ptaa104`. eprint: `https://academic.oup.com/ptep/article-pdf/2020/8/083C01/34673722/ptaa104.pdf`.

[Hän06] D. Hänel. *Molekulare Gasdynamik: Einführung in die kinetische Theorie der Gase und Lattice-Boltzmann-Methoden.* Springer-Verlag, 2006.

[Har15] F. Harms. “Characterization and Minimization of Background Processes in the KATRIN Main Spectrometer”. PhD thesis. Karlsruher Institut für Technologie (KIT), 2015. DOI: `10.5445/IR/1000050027`.

[Jou18] K. Jousten. *Handbuch Vakuumtechnik.* Springer-Verlag, 2018.

[Kle+19] M. Kleesiek et al. “beta-Decay spectrum, response function and statistical model for neutrino mass measurements with the KATRIN experiment”. In: *The European Physical Journal C* 79.3 (Mar. 2019). ISSN: 1434-6052. DOI: `10.1140/epjc/s10052-019-6686-7`.

[Kle+ep] M. Klein et al. “Experimental investigation of the plasma in the KATRIN tritium source (Paper, preliminary title)”. In: (in prep.).

[Kle14] M. Kleesiek. “A Data-Analysis and Sensitivity-Optimization Framework for the KATRIN Experiment”. PhD thesis. Karlsruher Institut für Technologie (KIT), 2014. DOI: `10.5445/IR/1000043301`.

[Kle19] M. Klein. “Tritium ions in KATRIN: blocking, removal and detection”. 51.03.01; LK 01. PhD thesis. Karlsruher Institut für Technologie (KIT), 2019. 340 pp. DOI: `10.5445/IR/1000093526`.

[Knu67] M. Knudsen. *The cosine law in the kinetic theory of gases.* National Aeronautics and Space Administration, 1967.

[Kod+01] K. Kodama et al. “Observation of tau neutrino interactions”. In: *Physics Letters B* 504.3 (2001), pp. 218–224. ISSN: 0370-2693. DOI: `10.1016/S0370-2693(01)00307-0`.

[Kra+05] C. Kraus et al. “Final results from phase II of the Mainz neutrino mass search in tritium β decay”. In: *The European Physical Journal C* 40.4 (2005), pp. 447–468. DOI: `10.1140/epjc/s2005-02139-7`.

[Kuc+18] L. Kuckert et al. “Modelling of gas dynamical properties of the Katrin tritium source and implications for the neutrino mass measurement”. In: *Vacuum* 158 (2018), pp. 195–205. ISSN: 0042-207X. DOI: `10.1016/j.vacuum.2018.09.036`.

[Kuc16] L. Kuckert. “The Windowless Gaseous Tritium Source of the KATRIN Experiment – Characterisation of Gas Dynamical and Plasma Properties”. PhD thesis. Karlsruher Institut für Technologie (KIT), 2016. DOI: `10.5445/IR/1000065077`.

[LP14] J. Lesgourgues and S. Pastor. “Neutrino cosmology and Planck”. In: *New Journal of Physics* 16.6 (June 2014), p. 065002. ISSN: 1367-2630. DOI: `10.1088/1367-2630/16/6/065002`.

[LS85] V. Lobashev and P. Spivak. “A method for measuring the electron antineutrino rest mass”. In: *Nuclear Instruments and Methods in Physics Research Section A: Accelerators, Spectrometers, Detectors and Associated Equipment* 240.2 (1985), pp. 305–310. ISSN: 0168-9002. DOI: `10.1016/0168-9002(85)90640-0`.

[Lüt13] H. Lüth. *Surfaces and interfaces of solid materials.* Springer Science & Business Media, 2013.

[Mac21] M. B. Machatschek. “A Phenomenological Theory of KATRIN Source Potential Systematics and its Application in Krypton-83m Calibration Measurements”. 51.03.01; LK 01. PhD thesis. Karlsruher Institut für Technologie (KIT), 2021. 255 pp. DOI: `10.5445/IR/1000132391`.

[Mal07] O. B. Malyshev. “Characterisation of a turbo-molecular pumps by a minimum of parameters”. In: *Vacuum* 81.6 (2007). Proceedings of the European Vacuum Conference (EVC-9), pp. 752–758. ISSN: 0042-207X. DOI: `10.1016/j.vacuum.2005.11.055`.

[Mar+11] F. Marulli et al. “Effects of massive neutrinos on the large-scale structure of the Universe”. In: *Monthly Notices of the Royal Astronomical Society* 418.1 (Nov. 2011), pp. 346–356. ISSN: 0035-8711. DOI: `10.1111/j.1365-2966.2011.19488.x`. eprint: `https://academic.oup.com/mnras/article-pdf/418/1/346/2839351/mnras0418-0346.pdf`.

[Mar+21] A. C. Marsteller et al. “Neutral tritium gas reduction in the KATRIN differential pumping sections”. In: *Vacuum* 184 (2021), p. 109979. ISSN: 0042-207X. DOI: `10.1016/j.vacuum.2020.109979`.

[Mar20] A. C. Marsteller. “Characterization and Optimization of the KATRIN Tritium Source”. 51.03.01; LK 01. PhD thesis. Karlsruher Institut für Technologie (KIT), 2020. 182 pp. DOI: `10.5445/IR/1000127553`.

[MN98] M. Matsumoto and T. Nishimura. “Mersenne Twister: A 623-Dimensionally Equidistributed Uniform Pseudo-Random Number Generator”. In: *ACM Trans. Model. Comput. Simul.* 8.1 (Jan. 1998), pp. 3–30. ISSN: 1049-3301. DOI: `10.1145/272991.272995`.

[MNS62] Z. Maki, M. Nakagawa, and S. Sakata. “Remarks on the Unified Model of Elementary Particles”. In: *Progress of Theoretical Physics* 28.5 (Nov. 1962), pp. 870–880. ISSN: 0033-068X. DOI: `10.1143/PTP.28.870`. eprint: `https://academic.oup.com/ptp/article-pdf/28/5/870/5258750/28-5-870.pdf`.

[Obl20] N. S. Oblath. “Project 8: Measuring the tritium beta-decay spectrum using Cyclotron Radiation Emission Spectroscopy”. In: *J. Phys. Conf. Ser.* 1468.1 (2020). Ed. by Masayuki Nakahata, p. 012178. DOI: `10.1088/1742-6596/1468/1/012178`.

[Ost19] R. Ostertag. “Investigation of Plasma Effects in the KATRIN Source with 83mKr”. MA thesis. Karlsruhe Institute of Technology (KIT), June 2019.

[OW08] E. W. Otten and C. Weinheimer. “Neutrino mass limit from tritium β decay”. In: *Reports on Progress in Physics* 71.8 (July 2008), p. 086201. DOI: `10.1088/0034-4885/71/8/086201`.

[Pic+92] A. Picard et al. “A solenoid retarding spectrometer with high resolution and transmission for keV electrons”. In: *Nuclear Instruments and Methods in Physics Research Section B: Beam Interactions with Materials and Atoms* 63.3 (1992), pp. 345–358. ISSN: 0168-583X. DOI: `10.1016/0168-583X(92)95119-C`.

[PKW64] W. E. F. Pauli, R. Kronig, and V. F. Weisskopf. *Collected scientific papers.* Offener Brief an die Gruppe der Radioaktiven bei der Gauvereinstagung zu Tübingen (datiert 4. Dez. 1930). New York, NY: Interscience, 1964.

[Pon57] B. Pontecorvo. “Mesonium and anti-mesonium”. In: *Sov. Phys. JETP* 6 (1957), p. 429.

[PSB15] F. Priester, M. Sturm, and B. Bornschein. “Commissioning and detailed results of KATRIN inner loop tritium processing system at Tritium Laboratory Karlsruhe”. In: *Vacuum* 116 (2015), pp. 42–47. ISSN: 0042-207X. DOI: `10.1016/j.vacuum.2015.02.030`.

[Röl15] M. Röllig. “Tritium analytics by beta induced X-ray spectrometry”. PhD thesis. Karlsruher Institut für Technologie (KIT), 2015. DOI: `10.5445/IR/1000054050`.

[Röt19] C. Röttele. “Tritium suppression factor of the KATRIN transport section”. PhD thesis. Karlsruher Institut für Technologie (KIT), 2019. DOI: `10.5445/IR/1000096733`.

[Sch+06] S. Schael et al. "Precision electroweak measurements on the Z resonance". In: *Phys. Rept.* 427 (2006), pp. 257–454. DOI: `10.1016/j.physrep.2005.12.006`. arXiv: `hep-ex/0509008`.

[Sch21] L. Schimpf. "Characterisation of energy loss processes of 18.6 keV electrons inside the windowless tritium source of KATRIN". 51.03.01; LK 01. PhD thesis. Karlsruher Institut für Technologie (KIT), 2021. 232 pp. DOI: `10.5445/IR/1000131810`.

[Sei19] H. Seitz-Moskaliuk. "Characterisation of the KATRIN tritium source and evaluation of systematic effects". PhD thesis. Karlsruher Institut für Technologie (KIT), 2019. DOI: `10.5445/IR/1000090748`.

[Ste+13] N. Steinbrink et al. "Neutrino mass sensitivity by MAC-E-Filter based time-of-flight spectroscopy with the example of KATRIN". In: *New Journal of Physics* 15.11 (Nov. 2013), p. 113020. DOI: `10.1088/1367-2630/15/11/113020`.

[Str11] U. Stroth. *Plasmaphysik.* Springer, 2011.

[TS00] T. Tabata and T. Shirai. "Analytic Cross Sections For Collisions Of H+, H2+, H3+, H, H2, And H– With Hydrogen Molecules". In: *Atomic Data and Nuclear Data Tables* 76.1 (2000), pp. 1–25. ISSN: 0092-640X. DOI: `10.1006/adnd.2000.0835`.

[Val11] K. Valerius. "The wire electrode system for the KATRIN main spectrometer". In: *Progress in Particle and Nuclear Physics* 64.2 (2011). Neutrinos in Cosmology, in Astro, Particle and Nuclear Physics: International Workshop on Nuclear Physics, 31st course, pp. 291–293. DOI: `10.1016/j.ppnp.2009.12.032`.

[Zub12] K. Zuber. *Neutrino physics.* Taylor & Francis, 2012.